CHALMERS

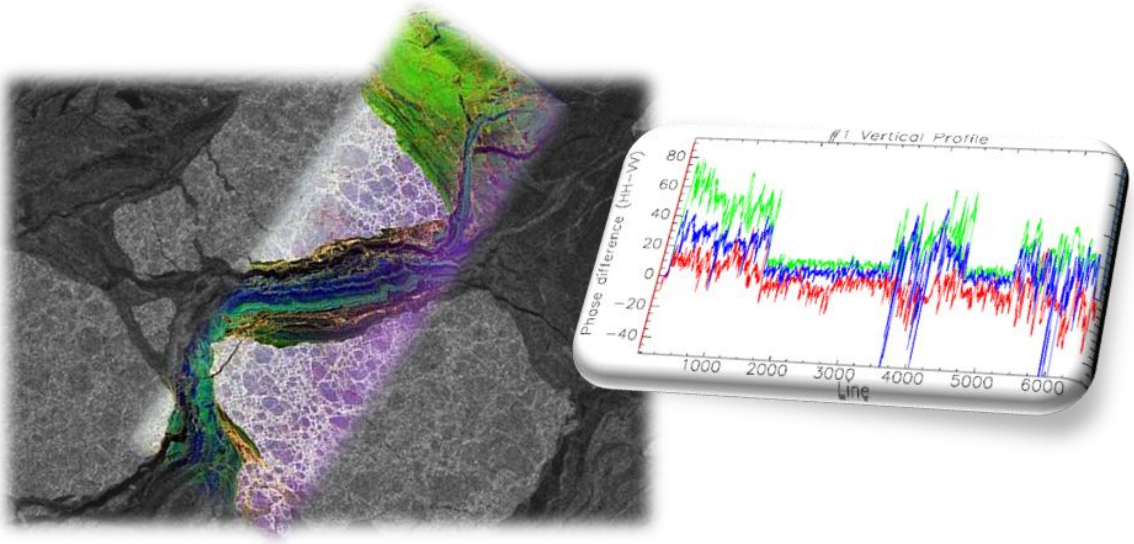

Analysis of Polarimetric Signatures of Arctic Lead Ice Using Data from AIRSAR and RADARSAT

Master of Science Thesis

DANIEL BÄCK

Department of Radio and Space Science
CHALMERS UNIVERSITY OF TECHNOLOGY
Göteborg, Sweden, 2008

Analysis of polarimetric signatures of Arctic lead ice using data from AIRSAR and RADARSAT
DANIEL BÄCK

© DANIEL BÄCK, 2008

Department of Radio and Space Science
Chalmers University of Technology
SE-412 96 Göteborg
Sweden
Telephone + 46 (0)31-772 1000

Cover:
A RADARSAT image and one of the AIRSAR scenes (6830) used in this project. The RADARSAT image has been acquired by CHH polarization and is coded gray whereas the AIRSAR images have been acquired in fully polarimetric mode (Red, green and blue colors corresponds to P-, L- and C-band total power, respectively)

Reproservice
Göteborg, Sweden 2008

Preface

This work has been done as a Master's thesis at the Department of Radio and Space Science at Chalmers University of Technology in Göteborg, Sweden. Most of the work including literature study, analysis of data and writing of the report was performed at NASA's Jet Propulsion Laboratory (JPL), California Institute of Technology in Pasadena, USA, and the visit lasted from February 16 to August 14 2007. My supervisor at JPL was Ben Holt from the Ocean-Atmosphere Interaction group in the Climate, Oceans and Solid Earth Science Section. Some final analysis of data and finishing of the report were conducted at Chalmers University of Technology during the fall 2007. My examiner at the Department of Radio and Space Science was Assistant Professor Leif Eriksson.

This report is divided into several major sections. First some background theory is presented such as for instance motivation of studying sea-ice and its impact on change of global warming as well as principles of radar remote sensing and a description of the two radar systems used in this project: AIRSAR and RADARSAT. The project will be defined and information about the AIRSAR and RADARSAT imagery will be described as well as the tools used throughout this project. A major part of this project was to analyze the calibration and quality of the data, so a particular section will discuss that. Then the process of identifying the different ice types and assigning them to different groups using the two radar systems will be explained. Two different sections are devoted to presentation of the polarimetric signatures and comparison with previous results. The last major chapter deals with classification and the search for different combinations of polarimetric parameters with optimum separation of the ice types. In the end all results will be discussed, conclusions will be drawn and advice for future work will be given.

There are a number of persons I would like to thank for all help throughout the project. Especially, I would like to thank my supervisor Ben Holt and the department of Ocean-Atmosphere Interaction at JPL for hosting and giving me the opportunity to do my Master's thesis there and also to experience a new country. Other persons that have helped me a lot with various questions at JPL are Bruce Chapman, Yunling Lou, Ron Kwok, Sassan Saatchi and Anita Lacroix. I appreciate the RADARSAT mosaic developed by Romain Husson. Also many thank to my examiner Leif Eriksson who first of all recommended me to contact Ben Holt, and also helped me out with many questions and practical issues. I would also like to thank Wolfgang Dierking and Martti Hallikainen for giving some valuable comments on my work.

This work was supported by the National Aeronautics and Space Administration through a contract with the Jet Propulsion Laboratory, California Institute of Technology.

Daniel Bäck
Chalmers University of Technology
October 2007

Abstract

In December 2004 the JPL airborne synthetic aperture radar (AIRSAR) flown on the NASA DC-8 acquired fully polarimetric data in the Beaufort Sea at C, L and P-band. This work presents the backscatter coefficients (σ_{HH}, σ_{VV}, σ_{HV}), copolarized ratios (σ_{HH}/σ_{VV}) and copolarized phase differences (ϕ_{HH-VV}) at the three frequencies from various sea ice types and in particular different young sea-ice types formed in recently frozen leads. Two weeks of RADARSAT imagery from the same region as the AIRSAR data was used in order to identify when and where leads were formed and the age of the newly formed ice contained within the leads. By using a known empirical relationship based on freezing degree days, the thickness of a sea-ice layer could be estimated from its age.

Several stages of new and young ice were identified and examined by using RADARSAT imagery to track back in time to find sea-ice openings: lead ice 1-2 days old, lead ice 2-3 days old, lead ice 9-14 days old, lead ice/first year ice older than 15 days and multi-year ice. Furthermore, narrow cracks with unique signatures, hypothesized to be a few hours old, found in several 1-2 days old leads have been included in the analysis. In addition to report the polarimetric signatures of these ice types, this study seeks to find which combination of polarimetric parameters that best differentiates the primary ice types as well as the stages of new and young ice within the leads.

Ice that is thought to be less than one day old has the lowest backscatter coefficients for C- and L-band. This ice type also has significantly larger copolar phases for C- band than the other ice types and is the only ice type that shows negative phase differences for L-band, in correspondence with previous reported results for very young ice. Furthermore, it has the lowest observed C-band copolar ratios. Ice 1-2 days old is characteristic for the large variability of the significantly negative P-band phases. Ice up to three days old has the lowest C-band copolar ratios. Using copolar ratios and phase to discriminate ice of age 9-14 days and older than 15 days was difficult, but L-band backscatter appears to give more contrast. The analysis of the phase information shows large variations between the thin ice types but it is hard to draw unambiguous conclusions. However, generally the phases for thin ice have much larger variability and typically have an offset relative to multi-year ice.

The best separations of thin ice are found by using C-band channels and for combinations with different polarizations. C-band crosspolarized backscatter coefficient combined with C-band copolarized ratio has been determined as giving the largest separation causing less misclassification, using a discriminant classifier. Ice less than one day and multi-year ice are the ice types that separate best from the other types while the other ice types more or less overlap for most combinations. Severe mixing between ice types occurs for combination of different L-band channels.

In future work the calibration quality of L- and P-band needs to be assessed. More time must be spent on trying to define different ice types and how to pick ice samples minimizing the effect of inhomogenities in the different polarimetric channels. Methods to determine normalized classification accuracies, independent of the number of samples of each class, must be considered.

Keywords: AIRSAR, RADARSAT, polarimetry, Arctic, Beaufort Sea, sea-ice, thin ice, young ice, lead ice, multi-year ice, sea ice thickness, polarimetric signatures, backscatter, co-polarized phase, classification

Table of Contents

Preface I
Abstract II
Table of Contents III
Acronyms and abbreviations V
1 Introduction 1
2 Background theory 2
2.1 Definition of sea-ice 2
2.2 Motivation of studying sea-ice 2
2.3 The formation and evolution of sea-ice 4
2.4 Radar and remote sensing 5
2.4.1 Terminology 5
2.4.2 Polarimetry 7
2.4.3 AIRSAR 9
2.4.4 RADARSAT 11
2.5 Scattering for of sea-ice 12
2.6 Thickness of sea ice 13
3 The project 14
3.1 Project description 14
3.2 Scene locations and image information 14
3.2.1 AIRSAR data 14
3.2.2 RADARSAT data 15
3.3 Environmental parameters 17
3.4 Tools used in the project 18
4 Calibration of AIRSAR scenes 20
4.1 Absolute and relative calibration 20
4.2 Phase calibration 22
4.3 Various artifacts of the data set 22
4.3.1 Artifact caused by hardware 22
4.3.2 Banding effect of the CVV channel 23
5 Identification of lead ice 24
5.1 How the RADARSAT imagery was used 24

5.2 Analysis of AIRSAR scenes 25
5.3 Summary of observations 30
5.4 Definition of ice types 31
6 Presentation of polarimetric signatures 32
7 Comparison with other studies 37
7.1 Multi-year ice 37
7.1.1 C-band 37
7.1.2 L-band 38
7.1.3 P-band 39
7.1.4 Phase 39
7.2 Thin ice / Lead ice 40
8 Classification 44
8.1 Combination of parameters 44
8.2 Implementation 46
8.3 Separation of different combinations 46
8.4 Previous results 49
8.5 Results of classification 50
9 Discussion and conclusions 53
10 Future work 55
11 References 57
Appendix A Ice terms ..... A
Appendix B AIRSAR Survey Image ..... B
Appendix C AIRSAR Scenes C
Appendix D RADARSAT image sequences ..... D
Appendix E Summary of polarimetric signatures ..... E
Appendix F Polarimetric signatures for all transects ..... F
Appendix G Combination of parameters over all incidence angels ..... G
Appendix H Combination of parameters in five different ranges of incidence angles ..... H
Appendix I Classification accuracies for different parameter combinations I

Acronyms and abbreviations

AIRSAR	Airborne Synthetic Aperture Radar
ASF	Alaska Satellite Facility
Co-pol	Co-polarized
Cross-pol	Cross-polarized
dB	Decibel
dBi	Decibel Isotropic
dBm	Power ratio in decibel
DC-8	Four-engined jet airliner
DOY	Day Of Year
EM	Electromagnetic
ENVI	Image processing and analysis software
ERS	European Remote Sensing Satellite
ESA	European Space Agency
FY	First Year
GHz	Gigahertz
GMT	Greenwich Meridian Time
HH	Horizontal transmit and horizontal receive polarizations
HV	Horizontal transmit and vertical receive polarizations
IABP/POLES	International Arctic Buoy Programme/Polar Exchange at the Sea Surface
IAOE'91	International Arctic Ocean Expedition 1991
Ice1	Ice type 1 (Lead ice: 1-2 days old or 8-13 cm thick)
Ice2	Ice type 2 (Lead ice: 9-14 days old or 25-36 cm thick)
Ice3	Ice type 3 (Thin first year ice: older than 15 days or thicker than 32 cm)
Ice4	Ice type 4 (Multi-year ice)
Ice5	Ice type 5 (Lead ice: 2-3 days old or 12-15 cm thick)
Ice6	Ice type 6 (Lead ice: Less than 1 day or less than 9 cm thick)
IDL	Interactive Data Language
IEEE	Institute of Electrical and Electronics Engineers, Inc
IPCC	Intergovernmental Panel on Climate Change
IR	Infrared
JERS	Japanese Earth Resources Satellite
JPL	Jet Propulsion Laboratory
MATLAB	Matrix Laboratory (numerical computing environment and programming language)
MHz	Megahertz
MY	Multi-year
NASA	National Aeronautics and Space Administration
Pi-SAR	Japanese airborne SAR system
POLCAL	JPL Polarimetric Calibration Tool
POLSAR	Polarimetric Synthetic Aperture Radar
POLSARPRO	Polarimetric Synthetic Aperture Radar Data Processing Tool
PRF	Pulse repetition frequency
RADAR	Radio Detection And Ranging
RADARSAT	Canadian earth observation satellite

RF	Radio Frequency
SAR	Synthetic Aperture Radar
SAT	Surface Air Temperature
SIR-C	Spaceborne Imaging Radar-C
SLAR	Side-Looking Airborne Radar
SLP	Sea Level Pressure
SPM	Small Perturbation Method
ThFY	Thin First Year
ThFYa-c	Thin First Year ice type a-c
THz	Terahertz
TOPSAR	Topographic Synthetic Aperture Radar
UTC	Coordinated Universal Time
VV	Vertical transmit and vertical receive polarizations
WMO	World Meteorological Organization

1 Introduction

The polar oceans are covered by an uneven sheet of sea-ice formed by the freezing of ocean surface water. The area of ocean covered by this ice varies strongly with the season. In the spring the coverage reaches its maximum where its presence impacts human activities. During minimum coverage, in late summer and early fall, the ice is confined to the most remote regions of the polar oceans. Remote sensing platforms such as airplanes and satellites are a natural tool for the environmental observations in the polar regions, where the spatial scales are vast, transportations is difficult and hazardous, operations are expensive, and the climate is hostile. Operating in the microwave spectrum overcome the limitations to weather and light levels (Carsey, et al., 1992).

Navigators, explorers, geographers, climatologists, and other researchers have long been interested in sea-ice. The interest in sea-ice properties and behavior derives from its roles in the climate system and in polar operations. The sea-ice cover interacts with the ocean and atmosphere. It forms a boundary between the relatively warm ocean water and the cold polar atmosphere, resulting in an effective insulation. The bright surface causes most of the solar radiation to be reflected back to the atmosphere, causing the polar regions to be relatively cool, whereas dark spots as open water and thin ice absorbs more solar energy. This is called the albedo effect. Thinning of sea-ice results in further absorption of solar energy and heat transfer to the atmosphere and effectively acts as positive feedback loop, rising the temperature further. The formation of sea ice crystals include the rejection of salt that eventually makes its way back to the surrounding ocean during grow or melt. Sea ice melt also includes adding fresh water back to the ocean. The exchange of salt and fresh water between sea-ice and ocean influences global ocean circulation. All these processes make the polar regions one of the most sensitive areas to climate changes on earth. Any change could have serious impacts for the animal life, for instance the polar ecosystems including polar bears. However, using the Arctic Ocean as a route for transportation would be relatively cheap and could be possible if further thinning of sea-ice continues.

This study will analyze sea-ice data from the Beaufort Sea off the coast of Alaska acquired in December 2004 by the NASA DC-8 equipped with a synthetic aperture radar (AIRSAR). The AIRSAR system operates at three different frequencies (C, L and P-band) in the microwave region and four polarizations (HH, VV, HV and VH) are available for each frequency. The number of data channels and the spatial resolution are much higher than for existing satellite systems. The purpose of this study is to find combinations of channels that have potential of discriminating different thin ice types with different thicknesses. Previous studies have not focused so much on thin ice or have found it hard to discriminate thin ice types, so the goal is to take the knowledge one step forward.

Satellite imagery is used to estimate the age of the sea-ice and the thickness is estimated from a relation based on freezing-degree days. The results are compared with other results from an earlier AIRSAR campaign in the Beaufort Sea in 1988 and a Space Shuttle SIR-C mission in 1994. The quality of the data is evaluated and attempts to find new results primarily for thin ice are performed.

2 Background theory

2.1 Definition of sea-ice

The World Meteorological Organization (WMO) uses the following definition of sea-ice:
"Sea-ice is any form of ice found at sea which has originated from the freezing of sea-water"
Sea ice is simply frozen ocean water. It forms, grows, and melts in the ocean. In contrast, icebergs, glaciers, ice sheets, and ice shelves all originate on land. Sea ice is present in both Arctic and Antarctica.

Sea-ice could be divided into different subgroups relating to their ages and thicknesses, according to Table 1. Refer to Appendix A for definitions of various ice terms.

Table 1: Definition of different sea ice types (Ulaby, et al., 1986).

Ice type	Subgroup	Thickness
New Ice	Frazil ice	≤ 5cm
	Grease ice	≤ 5cm
	Slush	≤ 5cm
	Shuga	≤ 5cm
Nilas	Dark nilas	≤ 5cm
	Light nilas	> 5 cm
	Ice rind	≤ 5 cm
Pancake ice		10-20 cm
Young ice	Gray ice	10-15 cm
	Gray-white ice	15-30 cm
First-year ice	Thin first year ice/white ice	30-70 cm
	Medium first-year ice	70-120 cm
	Thick first year ice	> 120 cm
Old ice	Residual first year ice	60-180 cm
	Second-year ice	< 3 m
	Multi-year ice	≥ 3 m

In this report the following definition will be used: thin ice (new ice – young ice), first year ice and multi-year ice (second-year ice – multi-year ice). First year ice and multi-year ice will sometimes be referred to as FY and MY ice, respectively.

2.2 Motivation of studying sea-ice

Properties of sea-ice including extent and thickness affect the global climate. One of the hottest topics these days is global warming and sea-ice is believed to be one of its major indicators. Sea-ice acts as an insulator between the warm sea water and the much colder atmosphere preventing heat to be exchanged. Brighter surfaces, that have high albedo, of sea-ice reflects most of the sunlight back into space help to keep the polar regions cold. Regions with low albedo such as cracks or openings in the ice, called leads, absorbs most of the solar radiation which leads to warming of the ocean and further melting of ice. Furthermore, thinning of sea-ice and openings significantly increases the heat flux from the ocean to the atmosphere; cracks and leads causes a tenfold increase. These effects are coupled together as a positive feedback loop amplifying the warming of the ocean and the atmosphere, and the

melting of sea-ice. Even a small increase in temperature can lead to greater warming over time, making the polar regions one of the most sensitive areas to climate change on Earth.

It has been reported in a recent study that from 1953-2006, Arctic sea ice extent at the end of the summer melt season in September has declined at a rate of -7.8% per decade. Over the period of modern satellite observations (1976-2006) the trend is even larger (-9.1% per decade) (Stroeve, et al., 2007). Figure 1 shows the dramatic trend. As can be observed, several models predict that the Arctic will be free of sea-ice by 2100. Another study reports that in September 2007 the sea-ice extent was so low that the "Northwest passage" was opened up for the first time since the satellite measurements began nearly 30 years ago (ESA, 2007).

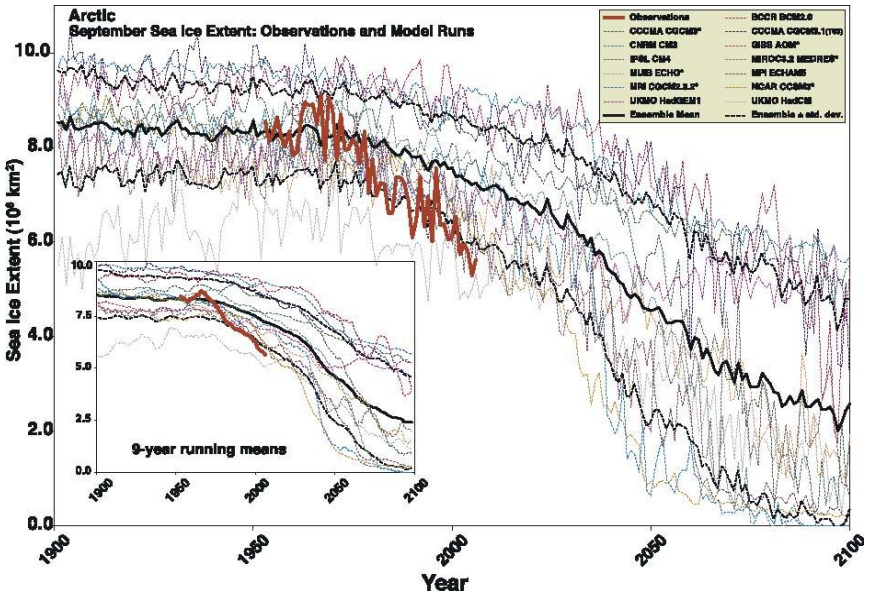

Figure 1: Arctic September sea ice extent (x 10^6 km^2) from observations (thick red line) and 13 IPCC AR4 climate models, together with the multi-model ensemble mean (solid black line) and standard deviation (dotted black line). Inset show 9-year running mean (Stroeve, et al., 2007).

Another thing worth mentioning is the significant shipping activities going on in the Arctic Sea despite its cold and harsh environment. Remote communities, facilities and oil drilling operations need resupply at regular intervals. This commonly involves ice breakers followed by freighters bringing supplies. Furthermore, scientific and military operations take place in the Arctic Sea utilizing for instance submarines for various missions. Contrary to the contribution to global warming, melting of sea-ice could lead to some positive effects. In the future the "Northwest passage" or Northeast passage could be used as a possible trading route since it would provide the shortest and fastest way between Europe and Asia. Even today the route is typically impassible because of sea-ice and is not used for commercial traffic. However, if the extent of sea-ice continues to decline, routes across the Arctic Ocean might be possible for parts of the year. To be able to use either the Northwest or Northeast Passages as a commercial ship route would be a lot faster and cheaper than going through Panama Canal or around all the continents. It is important to provide the ships with recent sea-ice charts with extent and thickness in order to navigate safely whether it is for resupply operations or commercial traffic.

2.3 The formation and evolution of sea-ice

When the surface is calm and cooling is rapid the ice forms in small crystals which join together to form a relatively uniform sheet of young ice. Ocean waves and currents could however result in an oily, opaque appearance, at which grease ice is said to exist. Upon further freezing, grease ice develops into nilas or ice rinds. Wind blowing on this surface causes pancake ice which looks like circular discs with raised edges. In due time, they merge to form continuous sheets. The thickness may exceed 10 cm in less than 48 hours. The colder the temperature is, the faster the growth rate. If the temperature is sufficiently cold and the wind is calm, ice particles form clusters on the surface that have high roughness, which is called frost flowers. New ice has high salinity or brine level but as the ice ages to first year ice the salinity is expelled into the sea-water. Remaining brine concentrates in tiny vertically oriented pockets within the ice. These are called brine pockets and act as dielectric discontinuities due to the high concentration of salinity compared to the surrounding. During the summer the heat of the sun moistens the snow near the surface, and melt pools begin to form. Old ice that has survived one summer typically is covered by refrozen melt pools has a very rough surface due to the impacts from the summer. Now the old ice has been drained so much so that the salinity near the surface is much lower than for the newer ice types and the brine pockets are replaced by air-filled voids. Wind, ocean currents, waves and pressure usually cause some deformation and drifting of the ice, resulting in blocks of ice piling up in ridges and hummocks. This process is called ridging. Ice floes could also be caused to diverge and form cracks or leads with open water. Figure 2 shows a schematic illustration of new ice, first-year ice, multi-year ice and summer ice. Figure 3 shows the evolutionary sequence for thin sea ice and how different ice conditions take place.

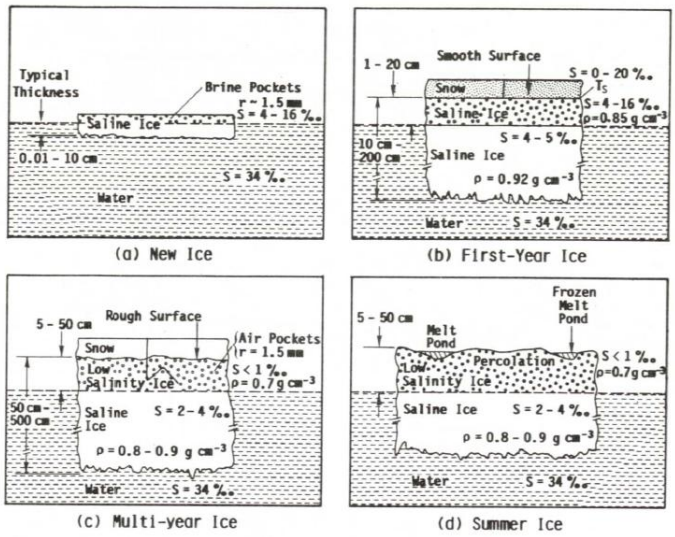

Figure 2: Schematic illustration of some principal ice types (Ulaby, et al., 1986)

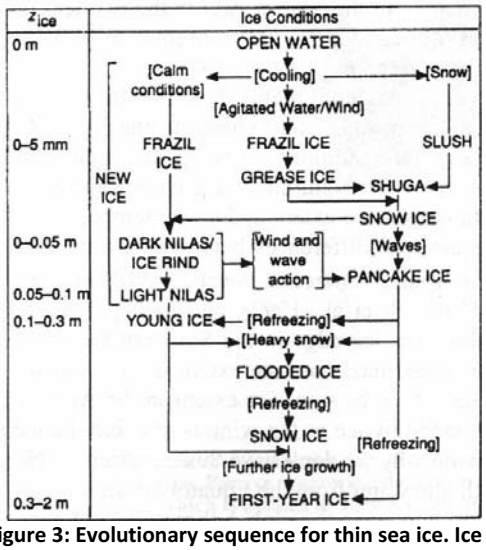

Figure 3: Evolutionary sequence for thin sea ice. Ice types are shown in capital letters and related environmental processes are enclosed in square brackets. (Grenfell, et al., 1992)

2.4 Radar and remote sensing

Jet Propulsion Laboratory (JPL) manages and operates a large suit of different radars used for remote sensing, both on earth and beyond in our solar system. AIRSAR is a NASA/JPL radar sensor with very high spatial resolution mounted on a DC-8 aircraft and is unique in providing useful data from several channels. Poseidon and Jason are two examples of altimeters that help us understand and foresee the effects of the changing oceans on our climate and on catastrophic climate events such as El Niño and La Niña. QuickSCAT is a scatterometer that can retrieve wind speed over the oceans by measuring radar reflection from the small capillary/gravity waves on the water surface and can therefore give a warning for potential hurricanes. Remote sensing is also used beyond our planet. Cassini-Huygens is a NASA/ESA collaboration that has given us amazing images of Saturn. In orbit around Saturn the satellite Cassini is also used to analyze its moons, for instance Titan that is interesting in particular since it is the only object other than Earth for which clear evidence of stable bodies of surface liquid has been found. It has found regions with low radar reflectivity, likely caused by liquid. Another hot topic is whether liquid water exists or has ever existed on Mars and therefore be able to support life. This is one of the main objectives to assess of several present remote sensing satellites, such as Mars Reconnaissance Orbiter, Mars Express and Mars Odyssey. The Mars Global Surveyor spacecraft has discovered gullies interpreted as startling evidence that liquid water flowed across the Martian surface in geologically recent times. Data from present and future remote sensing instruments will be the main aid in order to assist future human missions to Mars.

2.4.1 Terminology

When talking about remote sensing, passive and active sensors are usually mentioned. Passive sensors measure the natural emission that is emitted or reflected from the earth, e.g. the sunlight reflected from the ground, while an active sensor emits its own radiation and registers what is reflected back. By measuring the travel time of a signal it is possible to retrieve the distance to the target with an active sensor. This is the principle of radar (radio detection and ranging). Active remote sensing generally utilizes a part of the electromagnetic spectrum called microwaves which typically spans from 3 cm to 30 cm or frequencies ranging from 1 GHz to 10 GHz. A nomenclature has been designed when talking about radio and microwave signals. Frequency bands such as C, L and P-band which are common within remote sensing correspond 4-8 GHz, 1-2 GHz and 0.3-1 GHz, respectively (Woodhouse, 2006). These ranges are broad but for different applications the sensors usually use a narrower sub-band. This letter nomenclature was designed during the wartime and has no logic, the purpose was rather to confuse than to clarify. One benefit operating within any of these three bands instead of visual frequencies is that clouds are invisible. Higher frequencies easily get absorbed by for instance water vapor in the atmosphere. Utilization of microwave frequencies, unlike at visual frequencies, make it possible to operate both night and day, which is a major benefit when surveying polar regions where the sun is below the horizon for almost half of the year.

A radar is utilizing a transceiver which simplified consists of a transmitter and a receiver. The transmitter generates microwave signals typically by using electron tubes which use the motion of high speed electrons in specially designed structures to generate a variable electric/magnetic field which is then guided by waveguides to the antenna. One of the most important requirements for a radar system is

that the stream of generated pulses should be coherent, i.e. they should begin with the same phase (Woodhouse, 2006 p. 63). The same antenna is typically used for the receiver. Cross-talk is a measurement of the interference between the transmitted and the received signal, the lower value the better. The noise floor or sensitivity is a measurement of how small signals a receiver can detect before they drown in background noise. The received signal gets filtered away from noise and other distortions before it gets amplified and is then further processed with software to finally get a true image of the analyzed region.

Figure 4 shows the basic geometry and some of the notation for side looking airborne radar (SLAR). The airplane is flying in azimuth direction and radiates microwave signals in slant range direction. The direction for the airplane vertically down to the ground is called nadir. The difference between near-range and far-range is called range swath. Incidence angle is equivalent with look angle assuming a flat earth. The transmitted signal interacts with the surface and a part of it is reflected back to the receiver. During calm conditions a river acts as a smooth surface causing most of the signals to be reflected away from the radar, whereas upright stems in a forest and hills acts as strong double-bounce reflector causing much of the signals to be reflected back to the radar. It is expected to receive stronger signals in near-range than in far-range due to the difference in distance.

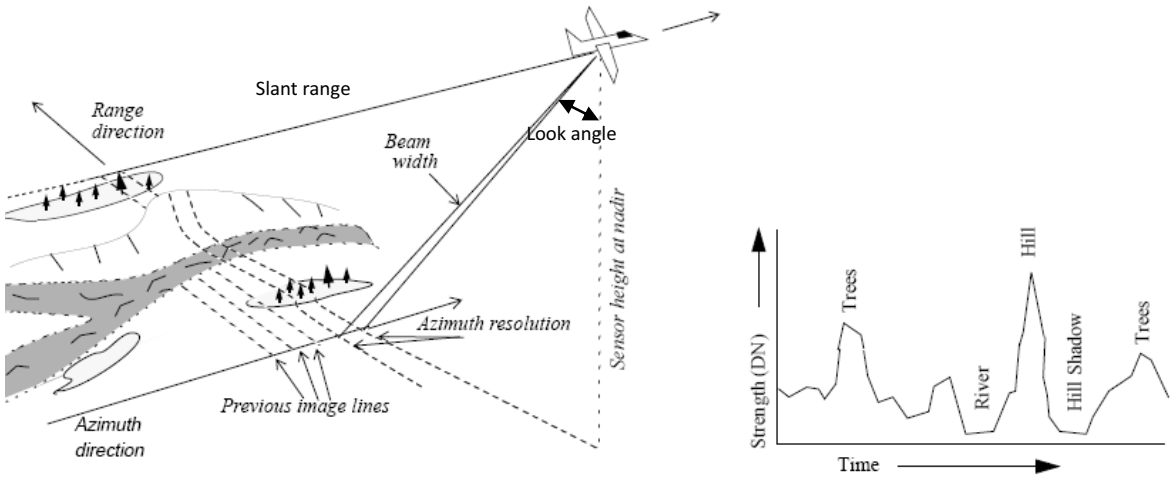

Figure 4: SLAR radar geometry and received radar signal (Smith, et al., 1997)

A synthetic aperture radar (SAR) is another type of SLAR which records the amplitude and phase of the returned signal as the radar moves forward. From these values it is possible to synthesize a much longer antenna than its physical one. The resolution of a radar system is an important parameter. It is defined as the maximum distance between two objects that can be distinguished as separate by the system.

The range resolution (cross-track) x_r of a SAR is:

$$x_r = \frac{c}{2B_r \sin\theta_i}$$

where *c* is the speed of light, B_r is the frequency bandwidth of the transmitted pulse and θ_i is the incidence angle (the angle between the radar beam and the normal to the earth's surface). Thus, it is important to have a large bandwidth if high resolution is required. Due to the geometry, resolution is better in far than near range.

The theoretical azimuth resolution (along-track) of a SAR is:

$$x_a = L_a/2$$

where L_a is the length of the antenna. This gives the impression that by reducing the length of the antenna the resolution would be increased. However, there is a limit how small the antenna could be:

$$W_a L_a > \frac{4V_s \lambda R \tan\theta_i}{c}$$

where W_a is the width of the antenna, V_s is the speed of the sensor platform (Curlander, et al., 1991). In fact the data in range and azimuth are coupled together in what is called an ambiguity relationship (McCandless, et al., 2004) so it is not an easy task to design a radar system that satisfies all requirements in a given specification.

The grainy "salt and pepper" appearance of a SAR image results from constructive and destructive interference of the coherent SAR pulse by different scatterers contained within a resolution cell. Despite its noisy appearance is not really noise in the classical sense but is referred to as speckle. However, it is often wanted to reduce it and one way is to average over N pixels in the spatial domain or equivalent divide the available bandwidth spectrum in N parts which are processed individually and then added together to form a SAR image. The result is an image less affected by speckle but to the price of lower resolution. The standard deviation of the speckle is reduced in proportion to the square root of the number of effective statistically independent looks. (McCandless, et al., 2004).

2.4.2 Polarimetry

A propagating electromagnetic (EM) wave (along the z-axis) can be represented as a superposition of two component waves that are orthogonal to each other: one horizontal (H) component having displacements only along the x-axis direction and one vertical (V) component only having displacements in y-direction, see Figure 5. They are said to have horizontal and vertical polarization, respectively. When an EM wave impinges an object it interacts with its molecules so that some part gets absorbed by the object, some part is transmitted through and the rest is reflected or scattered away. The relationship between incident and scattered wave fields is:

$$\begin{pmatrix} E_v^s \\ E_h^s \end{pmatrix} = \frac{e^{-ik_0 r}}{r} \begin{pmatrix} S_{VV} & S_{VH} \\ S_{HV} & S_{HH} \end{pmatrix} \begin{pmatrix} E_v^i \\ E_h^i \end{pmatrix}$$

where $E_{v/h}^{s/i}$ represent the scattered and incident wave fields (with amplitude and phase) with horizontal and vertical polarization. A radar system capable of measuring the amplitude and phase of all these four parameters is said to be fully polarimetric. The term $e^{-ik_0 r}/r$ takes into account the propagation effects, both phase and amplitude. k_0 is the propagation constant of the EM wave.

The scattering matrix ($S_{VV}, S_{VH}, S_{HV}, S_{HH}$) of an object is a complex quantity and depends on a large number of parameters such as wave frequency, wave polarization, surface geometrical structure and dielectric properties (Pottier, et al., 2006). It is often assumed that $S_{HV} \approx S_{VH}$ and therefore the average $(S_{VH} + S_{HV})/2$ is used for cross-pol.

Normalized radar cross section σ^0 of an object relates the scattered and incident wave field according to

$$\sigma^0 = \frac{4\pi R^2}{A_0}\left|\frac{E^s}{E^i}\right|^2 = 4\pi|S|^2$$

where *S* is the complex scattering amplitude of the object and A_0 is the area illuminated by the radar (Pottier, et al., 2006). Note that the radar cross section is a dimensionless unit measured in power. Often we are interested in the normalized radar cross section of a wave transmitted and received with particular polarizations. We are then using: σ^0_{HH}, σ^0_{HV}, σ^0_{VH} and σ^0_{VV} . In this report normalized radar cross section will simply be called backscatter or backscatter coefficients.

Another parameter often used is the copolarized ratio ($\sigma^0_{HH}/\sigma^0_{VV}$) which according to the small perturbation method (SPM) or the Bragg scattering theory only depends on the dielectric constant of the target and the incidence angle, and is independent of the surface roughness. This assumes that the surface conditions are in the validity regime of the SPM method. Flat (horizontal) surfaces tend to have σ^0_{VV}>σ^0_{HH} (Bragg scatter limit) but as the roughness increases the horizontal and vertical contributions become progressively similar. The ratios can therefore be an indicator of the type of surface cover.

The copolarized phase difference φ_{HH-VV} is an important parameter since it has physical meaning related to the number of interactions and different velocities in a medium for the different polarizations. The copolar phase difference near zero degrees is interpreted to mean single bounce scattering and a phase difference near 180 degrees is interpreted as double-bounce scattering, which refers to the interaction between two adjacent, but perpendicular, surfaces. The definition of copolar phase difference is (Woodhouse, 2006):

$$\tan\varphi_{HH-VV} = \frac{\mathrm{Im}(S_{HH}S^*_{VV})}{\mathrm{Re}(S_{HH}S^*_{VV})}$$

where S^*_{VV} denotes the complex conjugate of vertical polarized scattering coefficient.

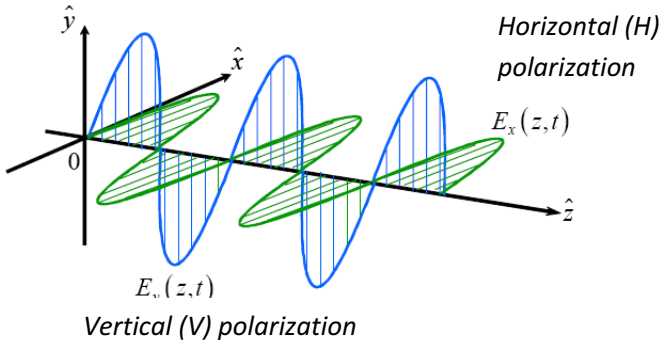

Figure 5: Spatial evolution of monochromatic plane wave components

2.4.3 AIRSAR

JPL/NASA manages and operates an airborne SAR (AIRSAR) mounted on a DC-8 (Figure 6) capable of acquiring three-frequency fully polarimetric data simultaneously. Thus, it is possible to get the radar backscatter for all possible combinations of horizontal and vertical transmit and receive polarizations (i.e. HH, HV, VH, and VV) and in addition the phase difference between copolarized polarizations (φ_{HH-VV}) for C-, L- and P-band. In 1988 AIRSAR was employed for missions in the Arctic Sea. This was the first time fully polarimetric sea-ice data were acquired and it is from this campaign much of the foundations of sea-ice signatures are based on today. Results obtained in this study will primarily be compared with the 1988 campaign, basically because they are based on the same system.

Figure 6: The JPL/NASA DC-8 (left) equipped with the AIRSAR sensor supported with phased array antennas (right).

In AIRSAR, polarimetry is implemented by alternately transmitting signals using horizontal or vertical polarization and measuring the received six channels of raw data simultaneously, both H and V polarizations at all three frequencies. The data is stored as a compressed Stokes matrix, achieving a total data volume reduction factor of about 50 (van Zyl, 1991). A decompression algorithm needs to be applied in order to extract or synthesize the polarimetric parameters. In order to compensate for various losses, perturbations and distortions, the extracted data need to be calibrated. Usually this is achieved by collecting data over targets with known backscatter coefficients. Rosamond calibration site, just north of JPL, is used for this purpose.

Table 2 summarizes some of the AIRSAR system characteristics. Theoretically, the noise level varies between -50 and -45 dB for P-band, -47 and -43 dB for L-band and -32 and -30 dB for C-band in the incidence angle range 28 to 55 degrees (see Figure 7). The VV channel appears slightly more sensitive than HH channel. The noise level decreases progressively in far range. The sensitivity characteristics could be derived from the antenna pattern.

Table 3 shows the calibrations goals for the AIRSAR system.

Table 2: Summary of AIRSAR system characteristics(van Zyl, 1991), (Lou, 2002).

Parameter	**C-band**	**L-band**	**P-band**
Chirp bandwidth	20 or 40 MHz	20 or 40 MHz	20 or 40 MHz
Chirp RF frequency	5308.75-5288.75 MHz (5307.50-5267.50 MHz)	1258.75-1238.75 MHz (1257.20-1217.50 MHz)	448.75-428.75 MHz (447.50-407.50 MHz)
Chirp duration	10 or 5 µs	10 or 5 µs	10 or 5 µs
Peak transmit power	59 dBm	67 dBm	62 dBm
Antenna polarization	H/V dual microstrip	H/V dual microstrip	H/V dual microstrip
Antenna gain	24 dBi	18 dBi	14 dBi
Azimuth beamwidth	2.5^o	8^o	19^o
Elevation beamwidth	50^o	44^o	38^o
Antenna dimensions	16.5 cm x 135.9 cm	45.7 cm x 161.3 cm	91.4 cm x 182.9 cm
Receiver gain	62 dB (63 dB)	50 dB (52 dB)	58 dB (59 dB)
Noise temperature	500-3000 K	500-3000 K	500-3000 K
Nominal altitude	8000 m		
Nominal velocity	450 knots		

Table 3: AIRSAR calibration goals (Freeman, et al., 1990)

Long and Short-Term Relative Calibration (Between passes and within an image frame)	±1 dB
Absolute Calibration (any channel)	±3 dB
Cross-frequency calibration	±1.5 dB
Polarization Amplitude Imbalance (between polarization channels	±0.4 dB (2-way)
Polarization Relative Phase Calibration (between polarization channels)	±10 deg (2-way)
Polarization Cross-Talk error (isolation)	-30 dB

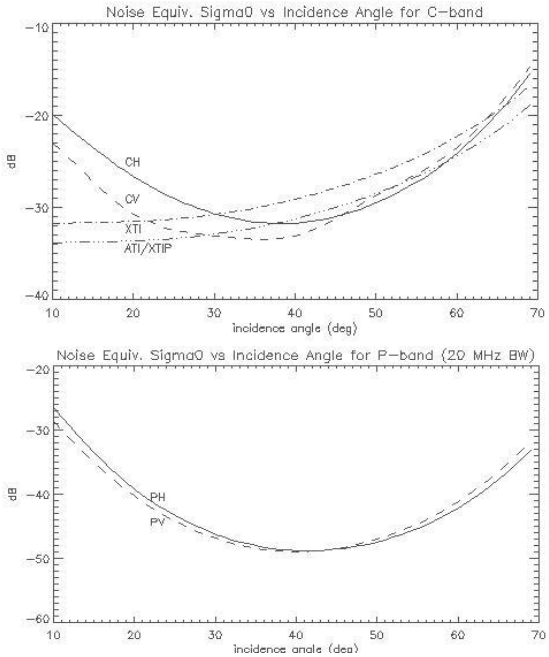

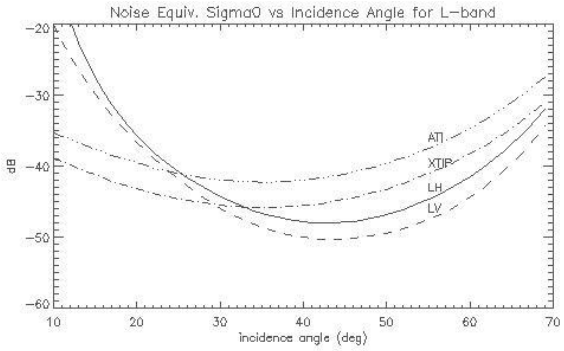

Figure 7: Theoretically evaluated noise floors for C, L and P-band for the AIRSAR system (Lou, 2002)

2.4.4 RADARSAT

RADARSAT (Figure 8) is a Canadian remote sensing satellite launched in 1995. It is using horizontal polarized (HH) C-band radiation and a variety of resolution, image swath width, and incidence angle combinations are available. See Table 4 and Table 5 for all system and orbit parameters. Is was developed for applications important to Canada, such as mapping of ice and northern regions; monitoring of agricultural, forestry, and geological resources; and maintaining a daily and all-weather capability for Arctic observations. Whereas it is known that a C-band SAR is not necessarily the optimum remote sensing instrument for all such applications, it can penetrate through cloud cover, haze, smoke, and thus allowing reliable observations in all seasons, and under poor optical conditions. Using the 500-km swath width, RADARSAT can provide daily imagery of the entire polar region above 79^0 north latitude (Raney, et al., 1991).

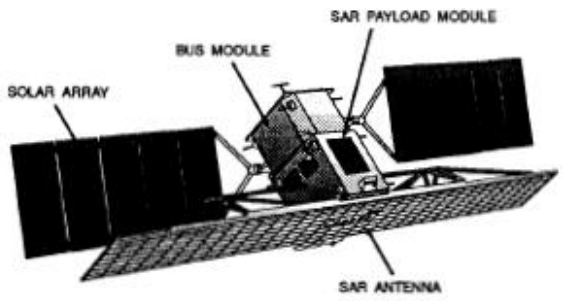

Figure 8: RADARSAT configuration, showing the antenna aligned with the solar panels, consistent with the dawn-dusk orbit (Raney, et al., 1991).

Table 5: Orbit parameters (Raney, et al., 1991).

Altitude (local)	793–821 km
Inclination	98.6°
Ascending node	1800 hours
Period	101 min
Repeat cycle	24 days
Subcycles	7 & 17 days
Reobservation	3+ days

Table 4: System parameters (Raney, et al., 1991).

Radar:	
Frequency	5.3 GHz
Wavelength	5.6 cm
Polarization	Horizontal
Pulse bandwidths	11.6, 17.3, or 30.0 MHz
Pulse length	42.0 μs
PRF	1270 – 1390 Hz (2 Hz steps)
Peak power	5 kW
Average power	300 W (nominal)
Input power needed	2500 W
Max. on time	28 min per orbit
Antenna size	15 m × 1.5 m
Pointing	≤ 0.2° (boresight)
(Elevation and azimuth)	
Preset Beams	20 (RAM)
Spacecraft:	
Spacecraft mass	2750 kg
Attitude control	~ 0.05°
Solar array	3.4 kW

2.5 Scattering for of sea-ice

A lot of effort has been put on trying to understand the complex processes behind the scattering of sea-ice, yet today this area is not fully understood. Sea-ice could be modeled as a three layer system where sea-ice is surrounded by air and sea-water. Usually also snow is added as another layer. The total backscatter is the contribution and interaction of surface scattering due to roughness of the different layers and diffuse volume scattering due to dielectric discontinuities within the layers, see Figure 9. The dielectric constant is a basic electric property of a material that affects the amounts that are reflected, absorbed and dissipated. The inverse of the dielectric constant is proportional to the penetration depth of the medium. For instance penetration of a radar wave into water that has high dielectric constant is negligible, causing most of the wave to be reflected. The dielectric constant is highly dependent on the salinity of the medium. Highly saline thin and first year ice therefore causes most of the incident radar energy to be reflected, i.e. surface scattering. In addition to the dielectric constant the roughness of the surface determines the amount of backscatter. A perfectly smooth surface reflects all the radar pulses away from the sensor except when the radar is directed at nadir. Figure 10 illustrates the evolution of microwave signatures for thin ice and first year ice. As can be noted the backscatter seem to vary pretty much (within 15 dB) as a result of ice aging, decrease of dielectric constant and thickness increase. Lowest backscatter is from new ice with smooth mirror-like surface, high dielectric with no absorption and no bubbles or void in the ice. During cold weather ice particles are clumped together (frost flowers) making the surface very rough and results in the highest backscatter values (Onstott, 1992).

Multiyear ice has lost much of is salinity through seasonal draining and thus is a low-loss medium providing longer penetration depths. There are a large number of dielectric discontinuities and dielectric scatterers such as brine inclusions and gas bubbles in multiyar ice. The large number of scatterers and their millimeter size contribute to large volume backscattering especially at C-band (Onstott, et al., 2004).

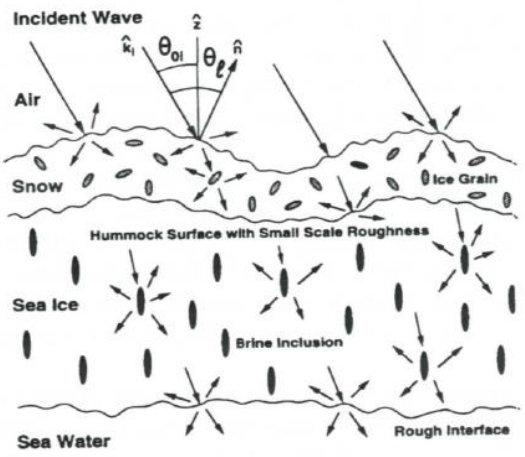

Figure 9: Scattering mechanisms in sea-ice (Nghiem, et al., 1995)

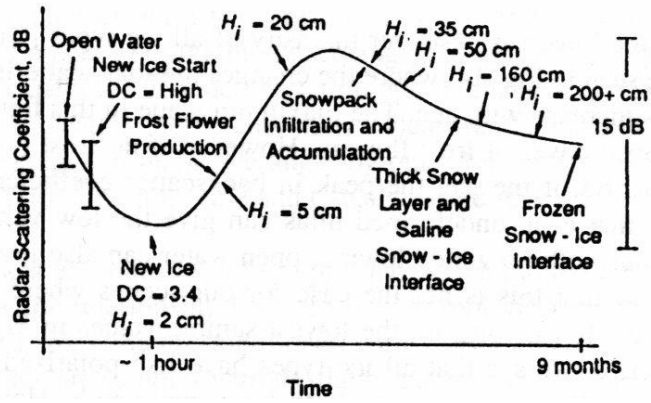

Figure 10: Radar-scattering evolution from thin sea ice to first year ice (Onstott, 1992)

2.6 Thickness of sea ice

Field studies have shown that the thickness (H) of young sea-ice is closely related to the cumulative number of freezing-degree days θ, where

$$\theta = \int_0^t (T_f - T_a)dt$$

T_f is the freezing point of the water (-1.8 degree Celsius at 35 ppt salinity) and T_a is the air temperature (usually at a height of 2 m). The thickness is then derived from the empirical relationship (Maykut, 1986)

$$H = 1.33\theta^{0.58}$$

For young ice grown during calm conditions without rafting processes, this relation should be a good estimate of the thickness (Wolfgang Dierking, personal communication).

Some work has been done using radar measurements to retrieve sea ice thickness using models, laboratory experiments and actual radar measurements. A neural network approach has been applied to estimate the ice thickness (Kwok, et al., 1995). C-band measurements based on thin ice grown in a laboratory have been performed (Kwok, et al., 1998). Data from the Sea of Okhotsk utilizing the Japanese L-band radar (Pi-SAR) show that backscattering ratios could estimate the sea-ice thickness which has been validated by ground-truth observations (Nakamura, et al., 2005). Another study modeling L-band scattering from the rough upper surface and including finite ice thickness showed that interference within the ice between downgoing waves and upgoing waves reflected from the sea ice/seawater transition layer leads to copolar phases and ratios in backscattering that oscillate, as function of ice thickness (Winebrenner, et al., 1995)

3 The project

3.1 Project description

This study will examine AIRSAR imagery acquired over the Beaufort Sea in 2004 and analyze different ice types and conditions. The AIRSAR system provides fully polarimetric data using C, L, and P-band imagery. The results will be compared to previous analysis using 1988 AIRSAR imagery of the Beaufort Sea and 1994 data from SIR-C undertaken initially by Leif Eriksson for his Masters work in 1997 at JPL. The new aspects of this analysis are the addition of the P-band polarimetric data. Particular emphasis will be placed on the detection of thin ice. This study will also assess the separation of different thin ice types using various two-parameter combinations of polarimetric channels. Two weeks of RADARSAT imagery over the same region as the AIRSAR scenes will be used in order to estimate the age of refrozen leads. A relation based on freezing-degree days will be used in order to estimate the thickness of the ice.

3.2 Scene locations and image information

3.2.1 AIRSAR data

Six scenes from the AIRSAR employment were chosen to be processed for further analysis: 6830, 6831, 6832, 6833, 6834 and 6837. See Appendix B for the AIRSAR survey image and the location of each scene. One of the scene (6837) was chosen not to be included in the study since it was hard to distinguish different ice types. This scene is located close to the coast of Alaska where there is extensive ice motion and impact from wind forcing in the seasonal ice zone, which extends to lead formation and closing and deformation, particularly in the early parts of winter (Ben Holt, personal communication). The scenes, their location and the time of acquirement at image centers are summarized in Table 6. A map of the data collection site is shown in a RADARSAT mosaic in Figure 11. All chosen scenes were acquired on December 2 2004 in POLSAR mode (polarimetric mode) and originate from datatake 218-1, except scene 6837 that originates from 218-2. The aircraft was flying in a direction of 218 degrees at an altitude of 7900 meters. In addition to the POLSAR datatake, TOPSAR data (interferometric mode) were acquired along the same general track as the POLSAR leg during the outbound transit, but this data will not be considered in this report. Two of the flight lines in Figure 11 were acquired in POLSAR mode and the other two in TOPSAR mode.

The slant range and azimuth pixel spacing are 6.66 and 9.26 m, respectively. The number of pixels in slant range direction is 2560 and is constant for all scenes, which means that each scene has a slant range swath width of 17.0 km. However, the number of lines in azimuth varies throughout the scenes and is summarized in Table 6. The incidence angle of the radar illumination on to the surface varies between 28 and 72 degrees. The bandwidth used was 20 MHz. The scenes have been processed with 18 looks in azimuth direction and the nominal resolution in slant range and azimuth is 11x21.6m. To keep the speckle to an acceptable level a further reduction was performed by applying a median filter with kernel size 11, thus an additional 121 looks were applied to the data resulting in a degradation of the resolution. However, due to the spatial correlation of neighboring pixels, the effective number of looks is not 121 x 18 but considerably less (Wolfgang Dierking, personal communication).

Table 6: Scene latitude, longitude and GMT are given for image centers

Scene	Latitude	Longitude	GMT	Lines in azimuth	Pixels in range
6830	75.10^o N	131.63^o W	2004/337:20:38:29	6611 (61.1 km)	2560 (17.0 km)
6831	74.70^o N	132.94^o W	2004/337:20:42:33	6626 (61.2 km)	2560 (17.0 km)
6832	74.37^o N	133.99^o W	2004/337:20:48:37	4466 (41.3 km)	2560 (17.0 km)
6833	74.14^o N	134.68^o W	2004/337:20:49:03	3321 (30.7 km)	2560 (17.0 km)
6834	72.82^o N	138.15^o W	2004/337:21:03:15	6520 (60.3 km)	2560 (17.0 km)
6837	71.16^o N	142.51^o W	2004/337:21:20:52	6564 (60.7 km)	2560 (17.0 km)

3.2.2 RADARSAT data

Over one hundred RADARSAT images/frames had been processed spanning a large part of the Beaufort Sea. The imagery ranges from November 17 to December 4 2004 and it is thus possible to track back about two weeks in time before and two days after the AIRSAR deployment. Each frame covers an area of about 512x460km, the nominal resolution in azimuth and range direction is 150m and the line and pixels spacing are both 100 m, according to the header files. Thus it is possible to analyze ice conditions at the AIRSAR scene locations, spanning several km in range and azimuth. There is a combination of frames with ascending and descending orbit.

The RADARSAT data were processed at the Alaska Satellite Facility (ASF). Each frame consists of one data and one leader file, and are identified by a 16 character long ID. For example:

R147095265PU008.D Data file
R147095265PU008.L Leader file

The first two characters (R1) corresponds to Radarsat-1, next five (47095) is the orbit number, next three (265) is the frame number and the last five characters is a processor version descriptor.

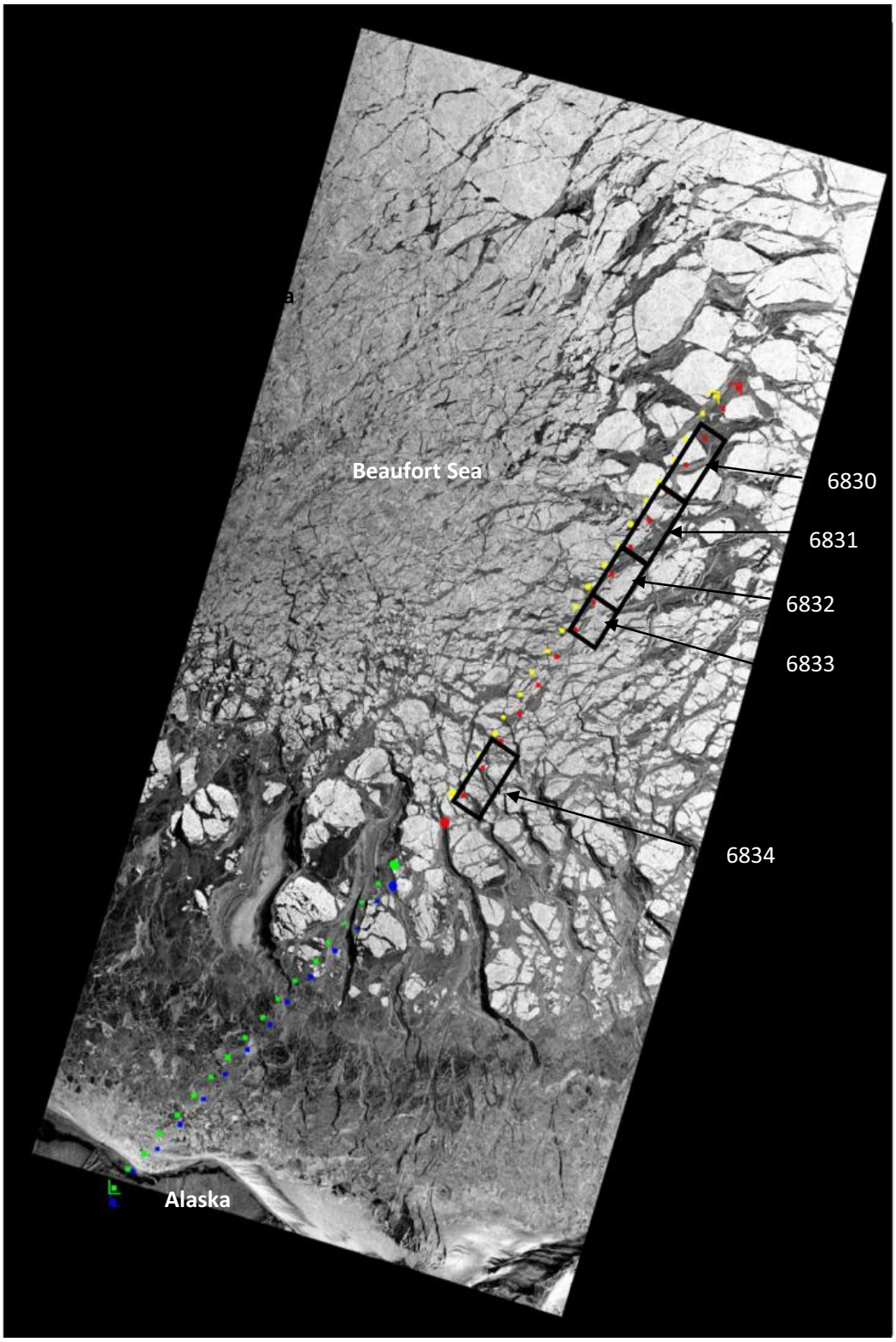

Figure 11: The approximate locations of the AIRSAR scenes are indicated in this RADARSAT mosaic. The blue and red sets of colored dots and the green and yellow ones correspond to the flight line when POLSAR and TOPSAR mode was used, respectively.

3.3 Environmental parameters

Crack openings and lead formations are an effect of various parameters, such as rapid temperature, pressure or wind changes or strong ocean currents. High wind speeds can start to drift ice and divergent ice motion can be responsible for new cracks and leads. The International Arctic Buoy Programme/Polar Exchange at the Sea Surface (IABP/POLAR) provides a dataset of surface air temperature (SAT) and sea level pressure (SLP) on a 100 km rectangular grid for all land and ocean areas of the Arctic region for the year 1979 to present. The data are available on a 12 hour and 24 hour interval for SAT and SLP, respectively. The data have derived from the combination and optimal interpolation of the following sources: 1) drifting buoys, obtained from IABP; 2) Russian North Pole drifting station; and 3) meteorological data, from more than 1600 land stations obtained from NCAR (dataset 464.0) (Rigor, et al., 2000). The spacing of buoys is rather coarse so some caution should be used when analyzing this data.

Figure 12 shows the surface air temperatures on Dec 2, 2004, just a couple of hours before the AIRSAR deployment. Furthermore, the location of the buoys and the AIRSAR scenes are highlighted. As can be seen the buoys are located quite far away from the AIRSAR scenes, which can introduce some uncertainties in the temperature estimates.

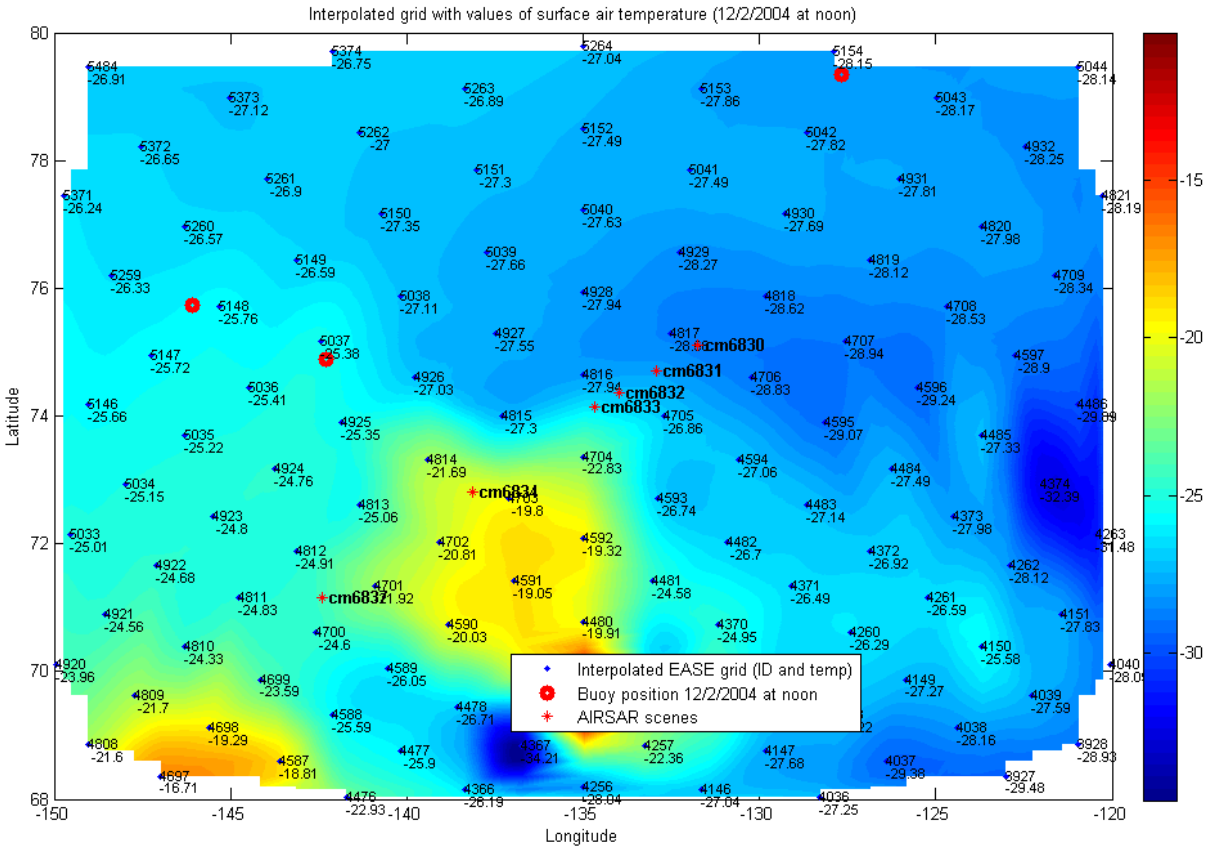

Figure 12: The IABP/POLES grid with surface air temperatures on Dec 2, 2004.

Figure 13 and Figure 14 show a time sequence from November 3 to December 3 2004 of the SAT and SLP, respectively, at the image centers of each AIRSAR scene. The temperatures and pressures have been calculated by interpolation of neighboring grid points in the IABP/POLES dataset. From the temperature records it is possible to estimate the thickness of the ice from the temperature, according to the relation described in 2.6.

Note that the temperatures are relatively low throughout the period, so the probability of any open water being present in the leads in any of the scenes should be rather low. The temperature variations in scenes 6830-6833 seem very similar which makes sense since they are located not very far from each other. Some trends could be observed, such as a slight decrease of temperature from November to December and colder further away off the coast of Alaska. There appears to be a large drop of temperature of about 10 degrees from Nov 24 to Nov 29. The pressure seems to fluctuate around some mean value but between some days it drops or increases considerably.

3.4 Tools used in the project

Two tools were evaluated for extraction of polarimetric parameters of the complex Stokes matrix: Polsarpro and ENVI. Polsarpro is a free software developed by ESA and ENVI is a commercial tool integrated with IDL and is used by many scientists and analysts around the world. Eventually, it was decided to use ENVI as a main tool for this project.

The different parameters extracted from ENVI were the backscatter coefficients HH, HV and VV, and copolarized phase differences φ_{HH-VV} for all three frequencies. Transects from different ice types were drawn using ENVI and all parameters were exported to Matlab for further analysis.

POLCAL is a calibration tool that has been developed at the Jet Propulsion Laboratory and has been used to evaluate the calibration of the data.

The tool “ASF Convert” was used to open the RADARSAT data files and save them to an appropriate picture format, e.g. jpeg. “ASF Convert” also has a metadata viewer which was used to look at the leader-files in order to find different parameters such as time of acquisition, resolution, swath width etc. Photoshop was used for most of the image editing such as image resizing, cropping, adding text to images, making the image sequences etc.

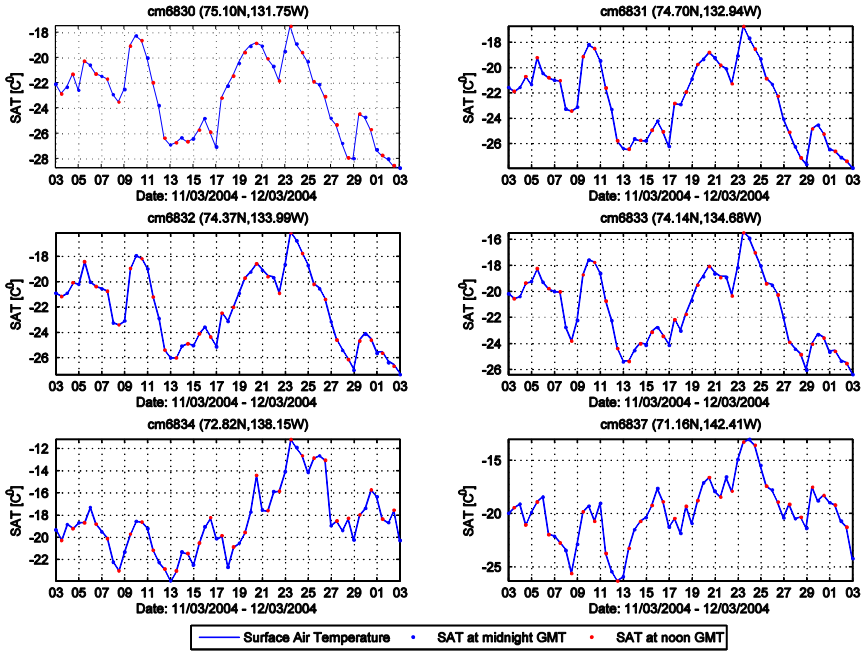

Figure 13: Surface air temperatures between Nov 3 and Dec 3 2004 derived from IABP/POLES data set.

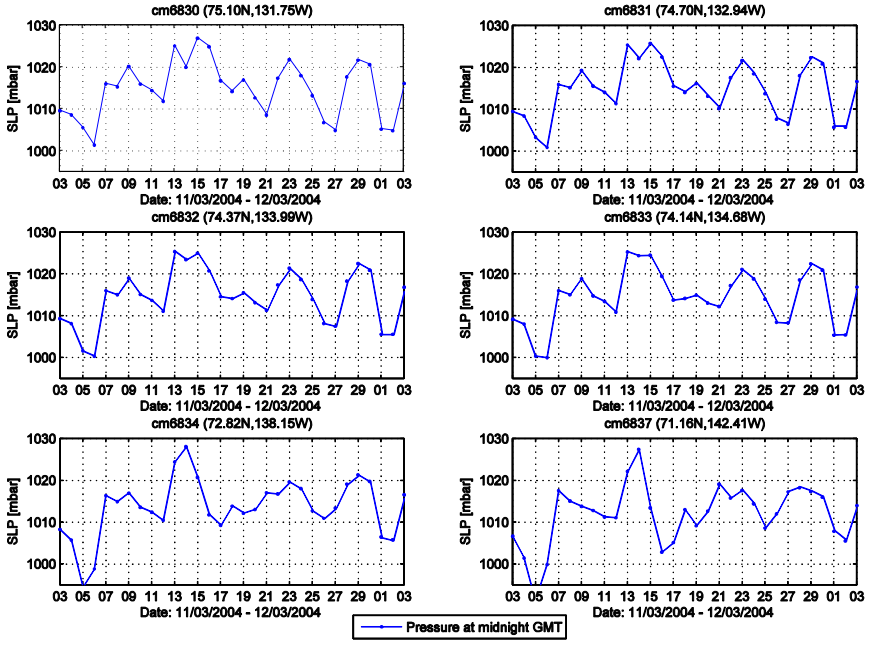

Figure 14: Surface level pressure between Nov 3 and Dec 3 2004 derived from IABP/POLES data set.

4 Calibration of AIRSAR scenes

4.1 Absolute and relative calibration

Four days after the sea-ice flights in the Beaufort Sea, the airplane flew over the Rosamond calibration site to acquire backscatter data over trihedrals, see Figure 15. The trihedrals have a known radar backscatter at C- and L-band which is utilized to correct for the amplitude offsets in the different polarization channels and the absolute gain of the radar system. The trihedrals are too small in order to accurately be used for P-band calibration. The corrections are needed to compensate for range propagation loss, antenna patterns, different receiver channel gains etc. By comparing the backscatter measurements with the theoretical values of the radar cross-section the absolute amplitude offset can be calculated. The channel imbalance is compensated for by analyzing the co-polarization ratio over the trihedrals that theoretically equals unity. The copolarized phase difference should theoretically be zero degrees.

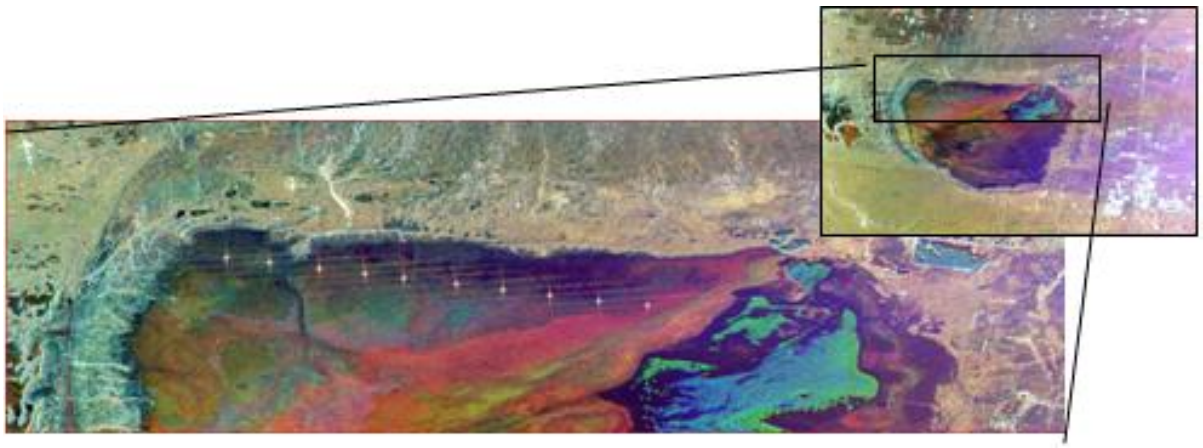

Figure 15: Radar image from Rosamond dry lake 12/6/2004 that has been used for calibration. Note the bright responses in the image that corresponds to the corner reflectors.

Figure 16 shows the observed response for each of the ten radar reflectors, which are aligned so that they have an incidence angle span of about 55 to 63 degrees relative to the radar sensor. POLCAL, a JPL calibration tool, has been used for the assessment. Note that L-band seems to be the frequency that is best calibrated; the co-polarized ratio is around unity, and the phase difference is quite good all over the range of incidence angles, and furthermore the measured and theoretical σ_{HH} data matches nicely. C-band data show that the phase calibration is acceptable. Also, it is observed that σ_{HH} should be suppressed with about 1-2 dB to compensate for the absolute calibration, which would also improve the gain balance. The trihedral corner reflectors are not optimized for lower frequencies as P-band. It is observed, however, that the results seem to be rather good, especially for lower incidence angles.

The cross-polarized channels have been calibrated (Bruce Chapman, personal communication).

Note that the radar reflectors are located within the incidence angle range 54-63 degrees and the range of incidence angles used in this project is 30-55 degrees. Previous measurements show that the copolar amplitude balance at C and L-band do not vary significantly between 27 and 55 degrees. The variations

at P-band are larger and this source of error is either due to the reflectors or the system (Freeman, et al., 1991).

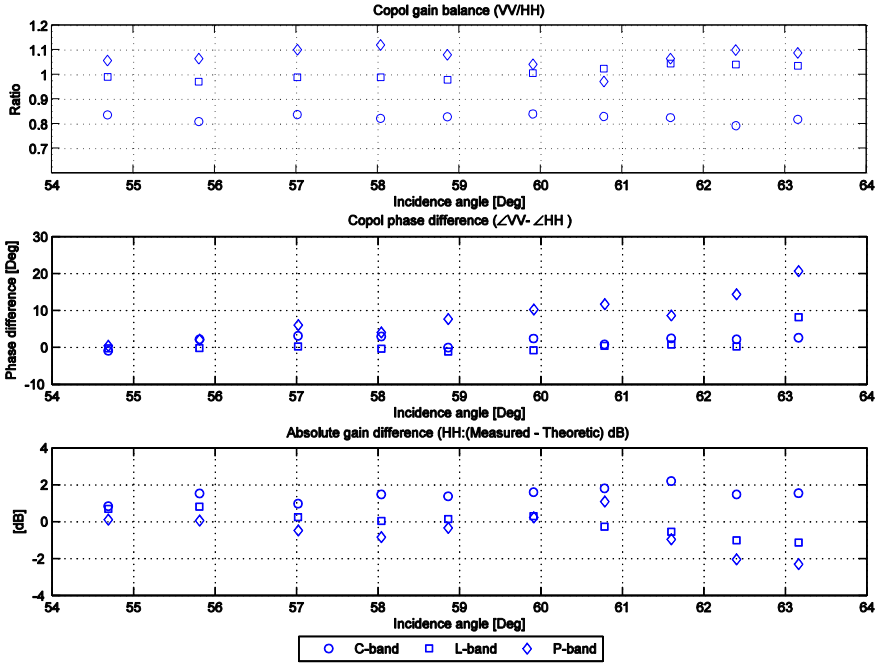

Figure 16: Signatures over trihedral calibration targets.

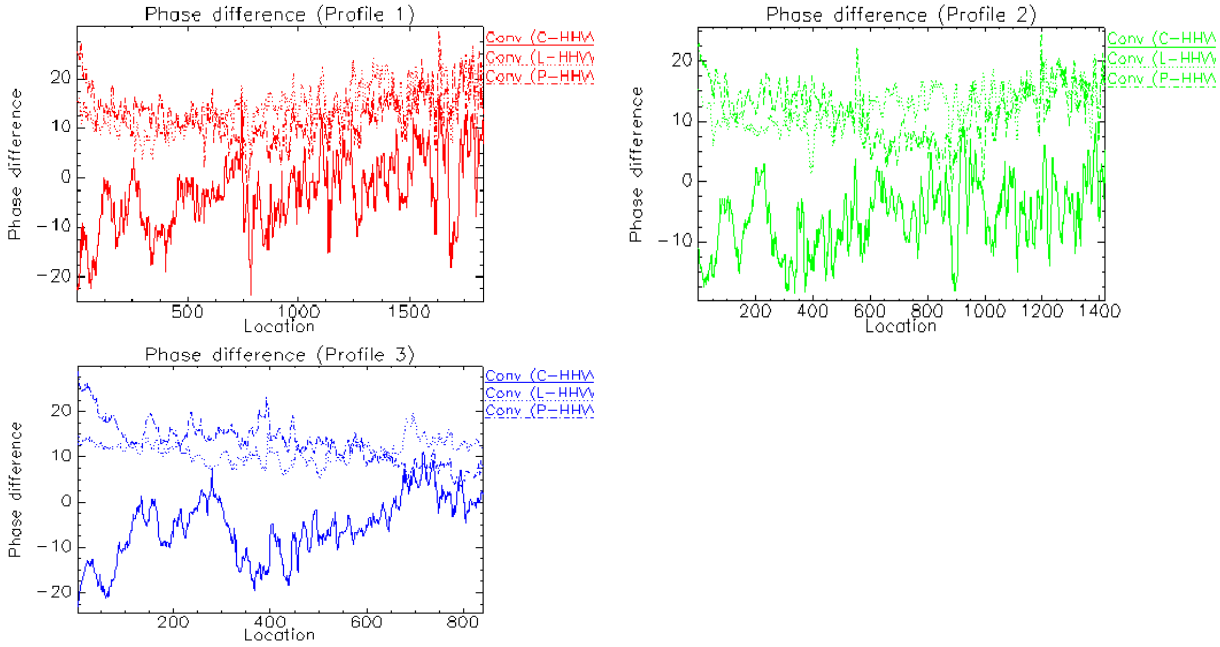

Figure 17: Phase differences for C, L and P-band along the three transects in Figure 18

4.2 Phase calibration

Multi-year ice has been used as a reference to calibrate the polarimetric phases, since theoretically the phase difference should be zero over multi-year ice (Winebrenner, et al., 1995). Both an offset and range dependence have been observed (Figure 17). In order to correct for the range dependence of the phase, three different profiles (see Figure 18) have been averaged together. The phase image has then been subtracted by this profile, in order to make the phase difference independent of range. The average offset corresponds to about -6.7 degrees for C-band, 11.1 degrees for L-band and 12.3 degrees for P-band.

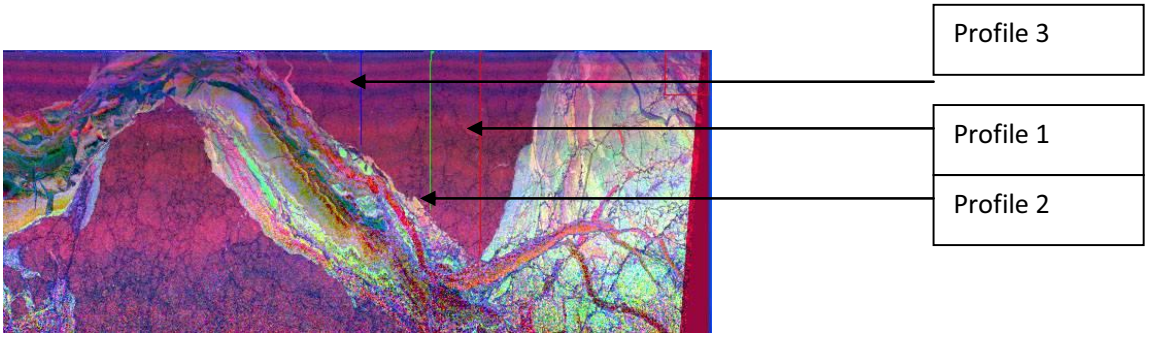

Figure 18: Three profiles/transects over a multi-year ice floe in scene 6830.

4.3 Various artifacts of the data set

4.3.1 Artifact caused by hardware

In was noted early in the project that the vertical polarization of L-band was about 14-15 dB larger than the horizontal polarization, see Figure 19. Similar results had not been found in the literature. A large amount of time was spent on figuring out what could be the reason for this. Eventually, it turned out that there must be a hardware error. The AIRSAR receiver actually consists of two receivers, one for horizontal and one for vertical polarization. As a part of processing, the co-polarized components get suppressed with a factor to the same level as the cross-polarized components, in order not to saturate the receivers. The operator of the AIRSAR equipped DC-8 usually commands the attenuation of the different channels during flight. Usually the HH and VV channels are suppressed 6 dB more than HV and VH, since this is typically the difference between the co-polarization and cross-polarization signals over land. Analyzing the calibration tone that was injected into the receiver it is possible to see what suppression that what used for different channels. It showed that the attenuator probably was stuck at 0 dB for both LHV and LVV channels. Thus, the LVV raw data were already 6 dB higher than the LHH raw data since the receiver gain for LVV did not get attenuated by 6 dB. Then in the processor another 6 dB was added to LVV data thinking that a 6 dB attenuation was used. That would explain why it is observed that LVV is 14-15 dB higher than LHH, 12 dB of which is attributable to calibration error (Yunling Lou, Personal Communication). The remaining 2-3 dB should correspond to the expected copolar ratio over multi-year ice. Compare with previously reported values around 4 dB over multi-year ice from an earlier sea-ice campaign in 1988 (Winebrenner, et al., 1995), (Drinkwater, et al., 1991).

The data were recalibrated by suppressing 12 dB to the VV channel and add a gain of 12 dB to the HV channel. This gave a satisfying copolar (HH/VV) ratio. However, at the end of the project (last week in Pasadena) it was noted that HH and VV appear to be about 6 dB too low when analyzing the backscatter of multi-year ice. Thus, the absolute backscatter values at L-band in this study must be used with some caution whereas the L-band copolar ratios are considered to be reliable.

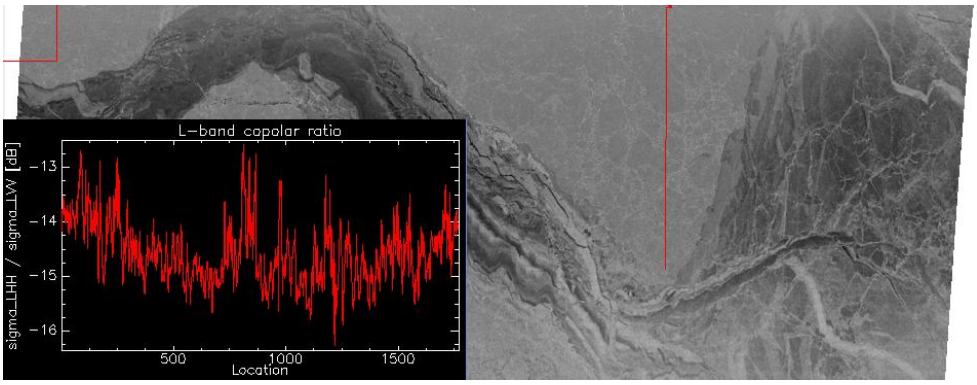

Figure 19: Plot of the L-band copolar ratio along a transect over multi-year ice in scene 6830.

4.3.2 Banding effect of the CVV channel

The effect appears only in the C-band and in the VV channel. It becomes obvious when analyzing the copolar plot of C-band (HH/VV) in logarithmic scale, see Figure 20. A similar problem has occurred before and it was referred to as CV Antenna Pattern Calibration Error (Lou, 2001), (Imel, 2002).

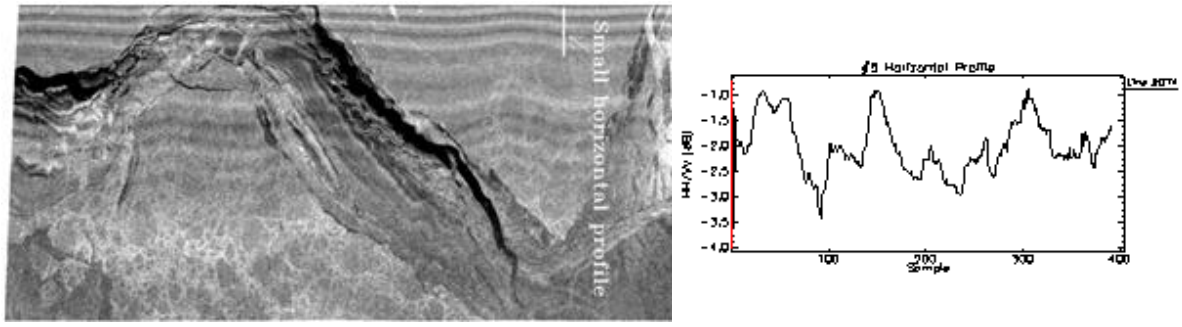

Figure 20: Example of banding effect observed in scene 6830 (HH/VV plotted for C-band and in dB-scale)

Notice the large periodic variations can be as high as 2.5 dB, see Figure 20. The banding effect seems to be around 1 dB. This could not only be due to strong reflections but obviously due to the banding effect in the CVV image. The effect is also apparent for the C-band phase difference, variations of about 20 degrees are observed in near range.

Conclusion: This is a hardware artifact only for CVV and C-band copolarized phase difference channels. Data of ice should be avoided to be picked in near range where the effect is most serious.

5 Identification of lead ice

A combination of AIRSAR and RADARSAT imagery was analyzed in order to identify different ice types. The RADARSAT imagery was used to track the ice motion and determine the age of the ice types.

5.1 How the RADARSAT imagery was used

The first task was to go through all RADARSAT images and identify each AIRSAR scene, and then resize the image so they covered about the same region. By looking in the header file in each RADARSAT image it was possible to determine when it was acquired. The notation of the time is: DDD:HH:MM:SS.MSEC, where DDD, HH, MM, SS, MSEC corresponds to day of the year (in 2004), hour of the day, minute, second and millisecond at the image center (UTC time), respectively. Only the day and hour were used to determine the time of datatake. Figure 21(a) shows an example of a RADARSAT image that has been resized so it should cover about the same region as scene 6830 in Figure 21(b). Note that the solid box approximately corresponds to scene 6830. The RADARSAT image was acquired 337:01, i.e. 1 am Dec 2 2004 which is about 20 hours before the AIRSAR scene 6830 was acquired.

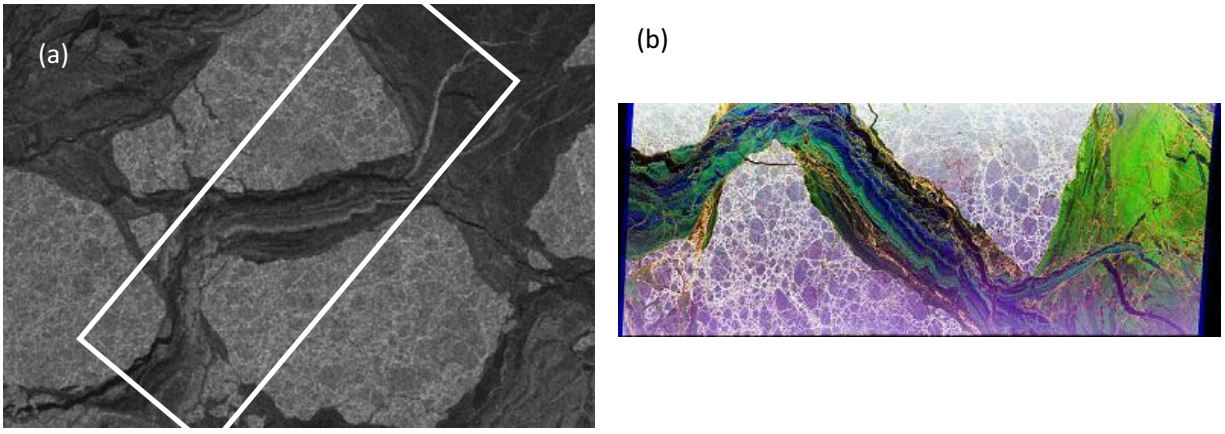

Figure 21: Radarsat image (a) covering roughly the same region as AIRSAR scene 6830 (b). The solid box indicates the AIRSAR frame location.

When all images covering each AIRSAR scene had been collected, the next task was to go through the image sequence and identify ice openings. It was observed that the ice moves relatively much in a couple of days. Figure 22 shows some examples of openings observed using the RADARSAT imagery covering AIRSAR scene 6830. In (d) two large leads have formed which are not observed in (c). The openings in (d) should have occurred sometime between 336:01 and 337:01, and the ice in scene 6830 (which was imaged 337:21) should thus be about 1-2 days old. Likewise the openings and the chunk break-off observed in (b) and not in (a) should correspond to ice of age 12-14 days old in scene 6830.

Appendix D contains all RADARSAT image sequences overpassing the AIRSAR scenes.

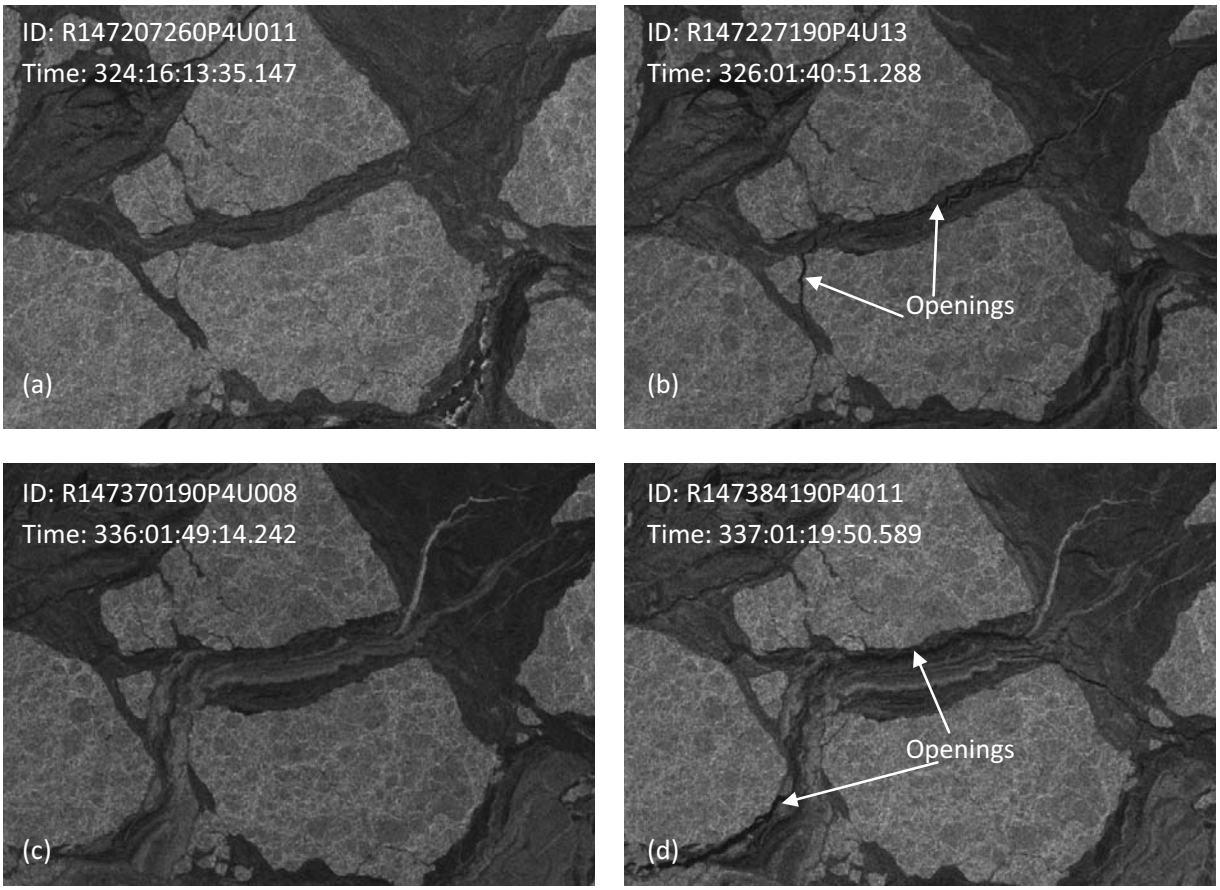

Figure 22: Two examples of openings in the ice observed using RADARSAT imagery. The regions overlap AIRSAR scene 6830 in Figure 21 (b).

5.2 Analysis of AIRSAR scenes

Figure 23 to Figure 27 show the identified ice types in the different AIRSAR scenes and the different transects indicate which samples that have been included for each ice type. Polarimetric signatures have been extracted from each transect. Note the dark, low-reflecting features in many of the scenes. This is probably young refrozen leads, about 1-3 days old. Since scene 6830-6833 are located next to each other, most of the leads in this scene probably opened at the same time. This is probably due to rapid movement of ice floes, which could be caused by changes of ocean currents or pressure. Analyzing the pressure records shows a large drop between November 30 and December 1. Maybe this could have caused strong winds to open up the ice.

Scene 6830 was the first one to be acquired during the Arctic campaign and it is located most far away off the coast of Alaska. An interesting refrozen lead containing a variety of different ice types is located between three multi-year ice floes. Probably these floes once were connected. What makes this scene interesting in particular is that probably most of the stages of the evolution from new ice to thin ice to first year ice are found in the refrozen lead. It means that darker parts probably are new ice and regions giving stronger reflections within the lead could be young ice that has developed frost flowers. Also some ice is identified as older than 15 days.

Two cracks in the refrozen lead are found and they probably consist of very young ice. Due to the low temperature the presence of open water is highly unlikely, see Figure 13. Young ice formed in calm and cold leads have a very smooth surface and acts like a mirror for the radar, thus its low backscatter. Analyzing the Radarsat images from the same region as scene 6830 gives a hint that the dark cracks were created sometime between 336:01 and 337:01, Figure 22 (a) and (b). The AIRSAR scene was imaged 337:21 and thus the ice in the crack would be 20-43 hours or about 1-2 days old.

In the middle of the refrozen lead is a complex region with bands giving different backscatter. An analysis of the Radarsat images shows that there was a crack opening sometime between 324:16 and 326:01, see Figure 22 (c) and (d), thus the youngest ice in this region should be about 12-14 days in the AIRSAR scene. The image sequence shows the evolution of the lead ice. After a couple of days (day 330) a very bright band appears in the middle of the lead. This could be the response of fully developed frost flowers which typically occurs when the lead ice is about 20-25 cm thick, which typically corresponds to an age of five days, see Figure 10 (Onstott, 1992 p. 91). Another hypothesis is that it may be brash ice due to convergent motion of ice floes. Another reason for the complex appearance might be that the thermodynamic growth is disturbed by rafting processes due to the ice motion (Wolfgang Dierking, Personal communication). The Radarsat images further hints that the ice closest to the newly opened lead is darker and might thus be younger. The movement of the ice causes the sheets to shear and this could open up some ice, which might be the reason why some dark regions are found.

A number of interesting leads have not been included in the analysis since they are located at an incidence angle larger than 55 degrees, for example the leads in the middle of scene 6831. It has been noted that background noise starts to contribute significantly at large incidence angles, especially the copolar phases at C-band. Not many studies have looked at data from so large incidence angles.

Shear zones with ice sheets moving with different speed have been identified in scene 6831 and 6833. From the RADARSAT imagery it has been noted that ice constantly breaks off and refreezes here, thus making it hard to determine the age of the young ice in these regions.

Some dark, low backscattering, narrow cracks have been observed in many of the 1-2 day old leads. These cracks probably consist of very young ice, less than one day or only a couple of hours old. However, this is a hypothesis since this has not been verified by the coarser RADARSAT imagery. Figure 28 shows an example of cracks in scene 6833. Furthermore, ice of age 2-3 days types have been indicated in this figure. It has been observed from the RADARSAT data that this ice was formed about one day prior to the ice in the 1-2 day old lead. Ice 2-3 days old has only been identified in scene 6833.

Several newly opened and refrozen leads could be found in scene 6834. However, it turns out that it is tricky to determine exactly the age of most of the leads because of lack of satellite coverage for many of the days. For instance the large lead to the left in the scene appears to be very young and probably is 1-2 days old but there is no coverage over this region for days 336 or 337 so the age could not be verified. One transect has been drawn over multi-year ice. It appears as the ice has a lot of deformation and ridges so this could affect that the backscatter could be somewhat higher than the other multi-year ice samples in scene 6830 and 6831.

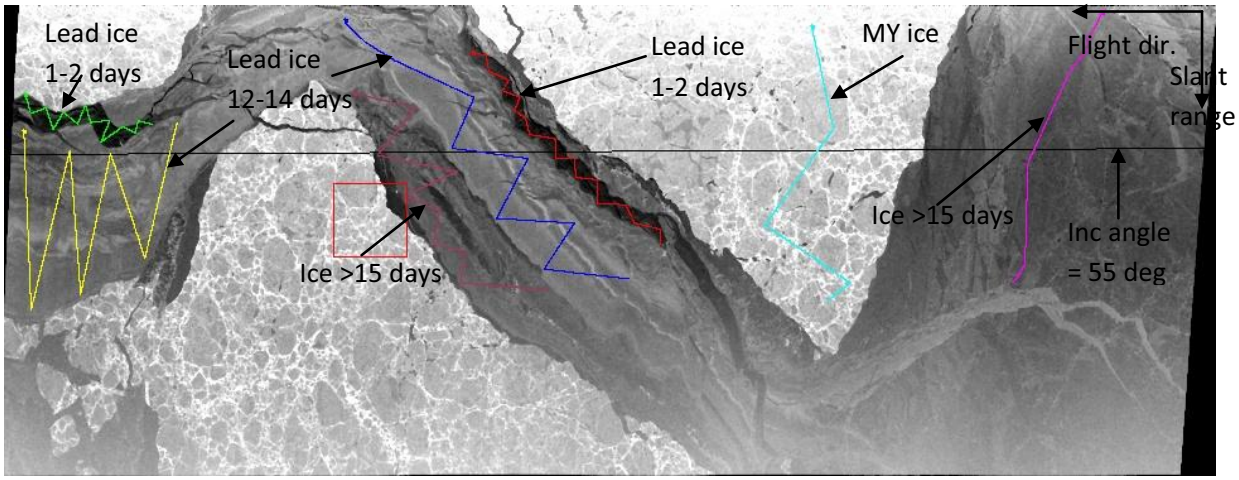

Figure 23: Scene 6830 (C-HH) and the picked transects. No data is included for incidence angles larger than 55 degrees.

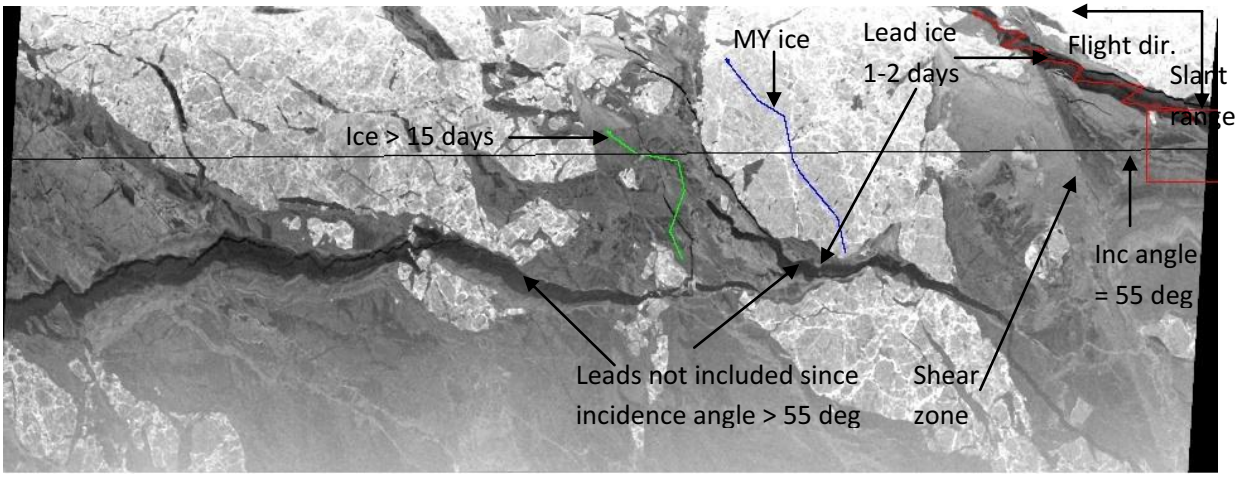

Figure 24: Scene 6831 (C-HH) and the picked transects. No data is included for incidence angles larger than 55 degrees.

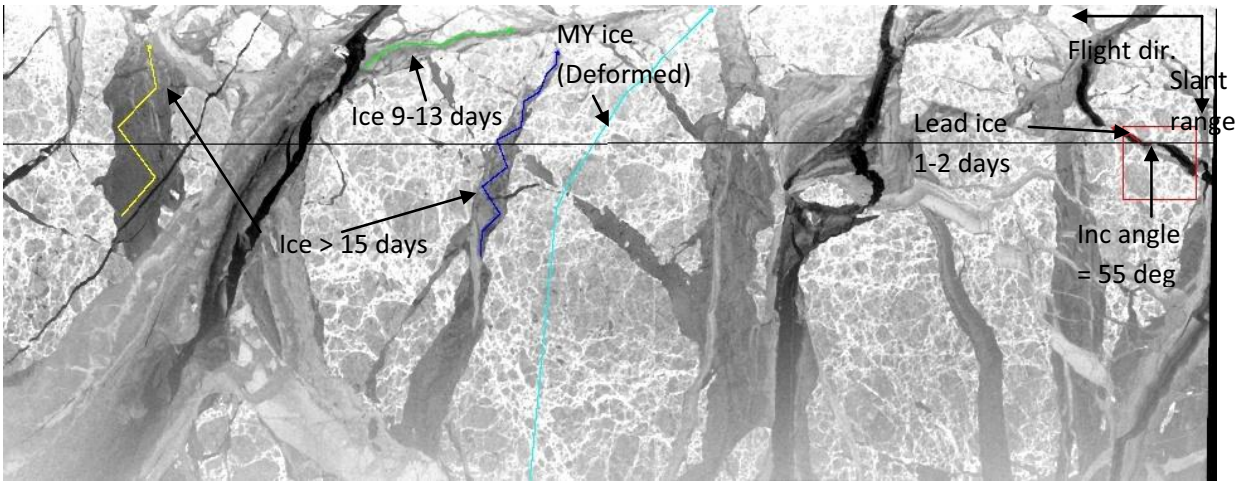

Figure 25: Scene 6834 (C-HH) and the picked transects. No data is included for incidence angles larger than 55 degrees.

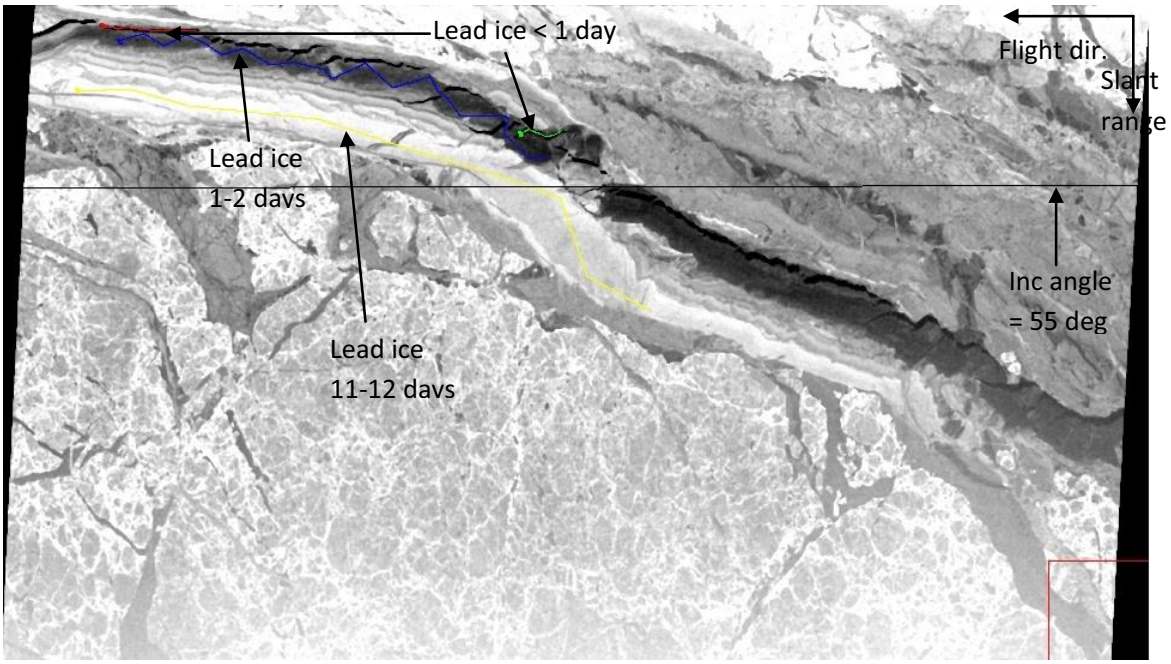

Figure 26: Scene 6832 (C-HH) and the picked transects. No data is included for incidence angles larger than 55 degrees.

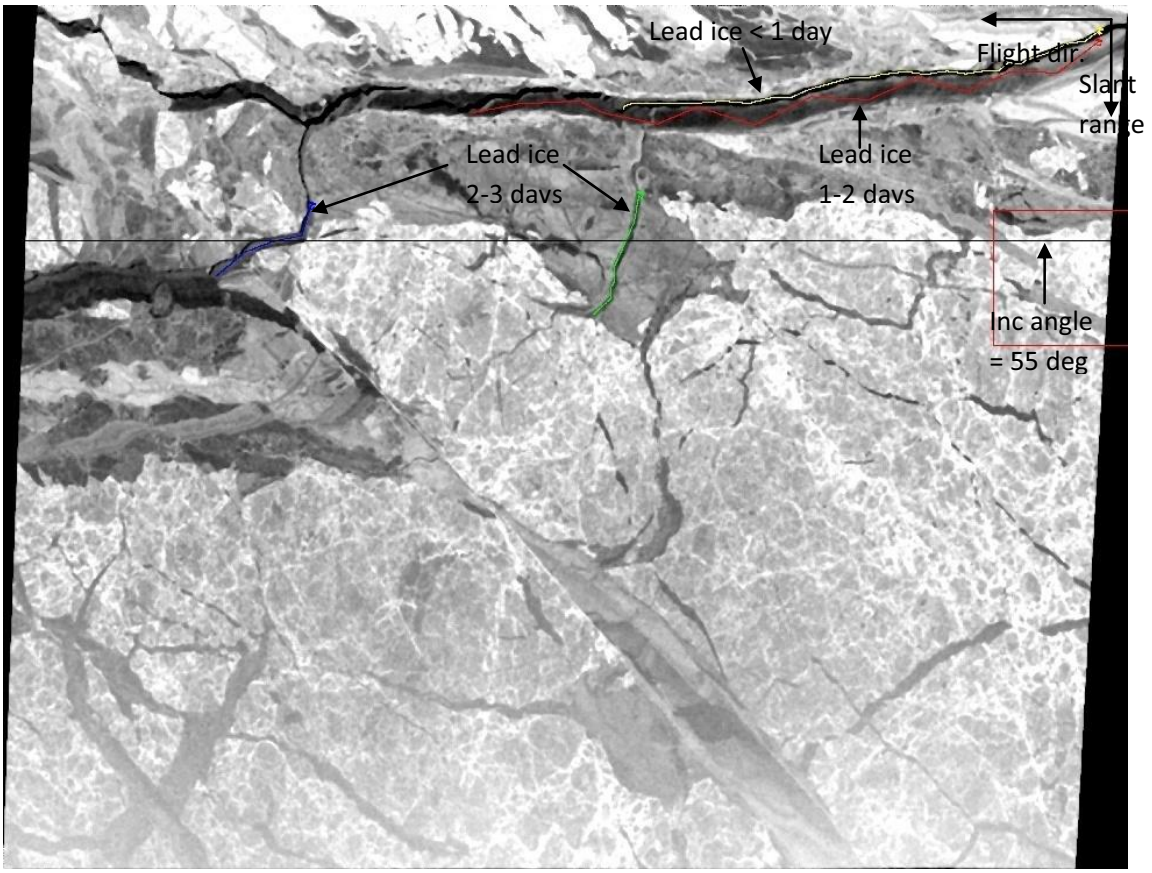

Figure 27: Scene 6833 (C-HH) and the picked transects. No data is included for incidence angles larger than 55 degrees.

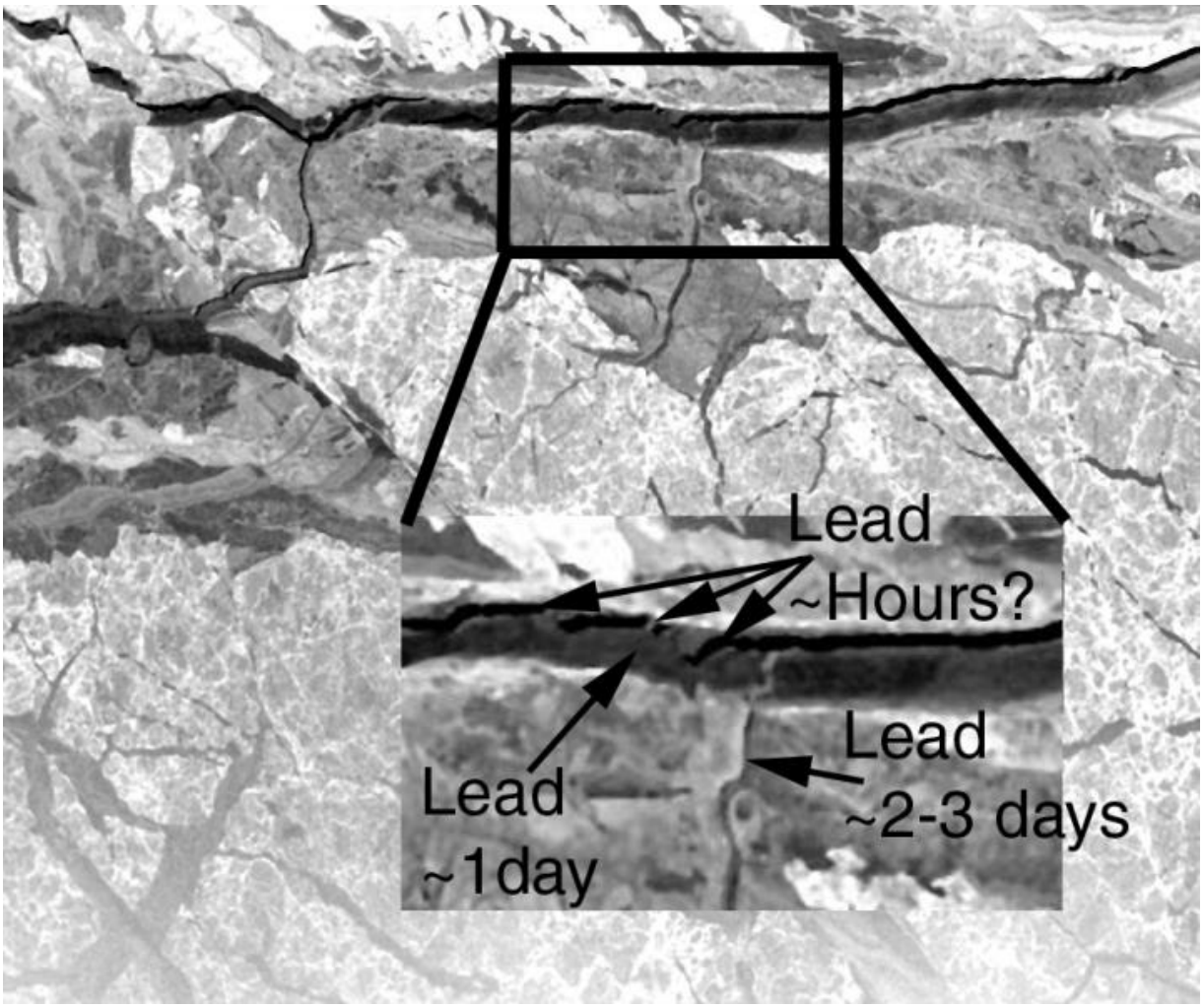

Figure 28: Zoom-in of scene 6833 reveals some dark cracks, hypothesized to be less than one day old.

5.3 Summary of observations

Table 7 to Table 11 summarize the identified ice types in the different scenes. The polarimetric signatures of these ice types will be analyzed further on. The day the ice was created as well as the age of the ice have been estimated from the RADARSAT imagery. The thickness has been estimated from the relation based on freezing-degree days using the temperature records provided from IABP/POLES data set. In the tables below, n/a stands for not applicable.

Table 7: Scene 6830

Ice type	Transects picked	Ice formed (DDD:HH)	Age (days)	Thickness (cm)	Incidence angle	Comments
Lead ice	2	336:01 - 337:01	1-2	9-13	42-55 deg 50-55 deg	
Lead ice	2	324:16 - 326:01	12-14	34-36	35-55 deg 53-55 deg	Might contain younger ice. Large dynamic range (Ice could vary from Young ice to Frost Flowers)
Thin ice/ FY ice	2	n/a	>15	>37	49-55 deg 31-55 deg	
MY ice	1	n/a	n/a	n/a	35-55 deg	

Table 8: Scene 6831

Ice type	Transects picked	Ice formed (DDD:HH)	Age (days)	Thickness (cm)	Incidence angle	Comments
Lead ice	1	336:01 - 337:01	1-2	9-13	32-52 deg	
Thin ice/ FY ice	1	n/a	> 15	>37	54-55 deg	
MY ice	1	n/a	n/a	n/a	44-55 deg	

Table 9: Scene 6832

Ice type	Transects picked	Ice formed (DDD:HH)	Age (days)	Thickness (cm)	Incidence angle	Comments
Lead ice	2	n/a	< 1	< 9	49-50 deg 34-35 deg	Age has not been verified by RADARSAT imagery.
Lead ice	1	336:01 - 337:01	1-2	9-13	35-52 deg	The age is probably the same as the lead to the left in scene 6831. The first opening is observed 332. Thus, some ice in the lead could be ~6 days.
Lead ice	1	326:01 – 327:16	11-12	32-34	45-55 deg	Could be covered with frost flowers due to its bright appearance in CHH.

Table 10: Scene 6833

Ice type	Transects picked	Ice formed (DDD:HH)	Age (days)	Thickness (cm)	Incidence angle	Comments
Lead ice	1	n/a	< 1	< 9	34-44 deg	Age has not been verified by RADARSAT imagery.
Lead ice	1	336:01 – 337:01	1-2	9-13	36-45 deg	Some regions to the right seem to be created one day earlier, thus might contain little older ice.
Lead ice	2	335:15 – 336:01	2-3	12-15	52-55 deg 52-55 deg	Might have a large dynamic range due to development of frost flowers

Table 11: Scene 6834

Ice type	Transects picked	Ice formed (DDD:HH)	Age (days)	Thickness (cm)	Incidence angle	Comments
Lead ice	1	336:01 – 337:01	1-2		54-55 deg	
Lead ice	1		9-13	25-30	37-44 deg	No RADARSAT coverage for some days.
Thin ice/ FY ice	2	n/a	> 15	>32	43-55 deg 42-55 deg	
MY ice	1	n/a	n/a	n/a	31-55 deg	

5.4 Definition of ice types

Table 12 defines the different ice types in terms of their estimated age and thickness. Also listed is the number of picked samples, or equivalently pixels, for each ice type. All ice types between 9 and 14 days have been grouped together as one ice type. No ice type of age 3 to 9 days old has been found. Note that ice type 1 (1-2 days) has most of the samples since this type was easiest to identify throughout the scenes. The thinnest ice samples of type 3 should be at least larger than 32 cm, according the freezing-degree relation in 2.6. Only 400 samples in the incidence angle range 52-55 degrees have been picked of ice type 5, since it was only found in one of the scenes (6833).

Table 12: Definition of ice types

Notation	Ice type	Age (days)	Thickness (cm)	Inc angle	Total samples
Ice1	Lead ice	1-2	8-13	32-55 deg	7758
Ice2	Lead ice	9-14	25-36	35-55 deg	3392
Ice3	Thin FY ice	> 15	>32	31-55 deg	2109
Ice4	MY ice	Year	?	31-55 deg	1812
Ice5	Lead ice	2-3	12-15	52-55 deg	407
Ice6	Lead ice	< 1	0-9	34-44 and 49-50 deg	1778

6 Presentation of polarimetric signatures

The different ice types have been picked using ENVI mainly by looking at the CHH and CVV images. The ice data (HH, VV, HV and the copolar phase differences and their incidence angle for all three frequencies) were exported to Matlab for further analysis. The copolar ratio (HH/VV) was calculated using Matlab rather than creating new images in ENVI. Appendix F summarizes the polarimetric signatures for all ice types and transects, and an example of the signatures for a particular lead ice profile 1-2 days old is shown in Figure 29. Small-scale variations are observed as well as large peaks especially for the L- and P-band backscatter coefficients, which likely is due to some deformation or variations in the ice comparable to the wavelength of L- and P-band.

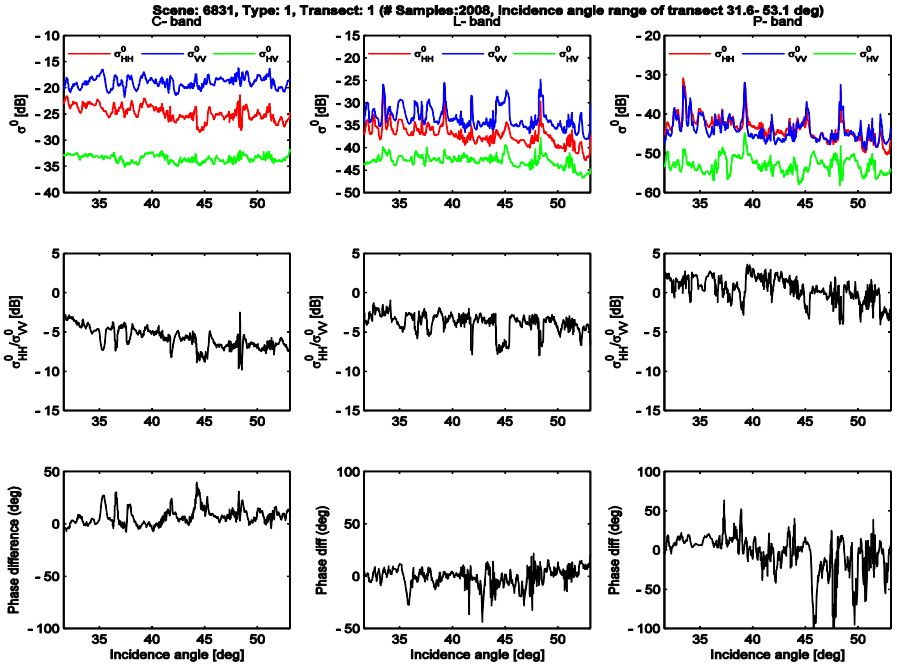

Figure 29: Polarimetric signatures of lead ice 1-2 days old. The data are from one transect in scene 6831.

All ice types were divided in groups of different incidence angle ranges: $30^o<\theta<35^o$, $35^o<\theta<40^o$, $40^o<\theta<45^o$, $45^o<\theta<50^o$ and $50^o<\theta<55^o$. It was decided not to include incidence angles larger than 55 degrees since these angles not have been included in most of the previous sea-ice radar acquisitions. Therefore it is easier to make a one-to-one comparison of the polarimetric signatures. Furthermore, the noise level starts to increase in far range so the risk is increased that the actual signatures of very young ice are hidden in the background noise. The mean value and standard deviation were calculated for all samples of each ice type within each incidence angle range. Lead ice 1-2 days (ice1) old has most of the samples and covers all the incidence angle ranges, whereas lead ice 2-3 days (ice5) has fewest samples and has only been found for incidence angles between 50^o and 55^o.

A summary of the averaged polarimetric signatures for all six ice types is presented in Figure 30. Three different parameters are plotted: normalized backscatter for C- and L-band occupies the first six bins, copolar ratio for C- and L-band the next two bins and finally the last three bins are occupied by the

copolar phase for all three bands. Figure 31 presents the standard deviations of the polarimetric parameters within each incidence angle range for each ice type. Variations increase for ice types with more samples. Appendix E summarizes the numerical values of the signatures (mean values and standard deviations) divided into the five different ranges of incidence angles

The reason why P-band backscatter is not included is due to the observation that the horizontal polarization was larger than the vertical one (HH>VV), including for multi-year ice. This behavior is not expected from theory and has not been found in the literature. It has been assumed that this is due to unbalanced channels, e.g. no calibration applied for this band. It has been reported that the P-band copolarized amplitude balance varies significantly across the swath, which either is caused by the reflectors or the AIRSAR system (Freeman, et al., 1991). Therefore, P-band is harder to calibrate. Thus, neither the backscatter coefficients nor the copolar ratio for P-bands have been included in the analysis further on. However, P-band phase difference has been included, since it has manually been adjusted to zero degree over multi-year ice which is what is expected from theory (Winebrenner, et al., 1995).

A number of expected things are observed:

- All thin ice types give low backscatter compared to multi-year ice. Multi-year ice has much lower dielectric constant and salinity compared to thin ice (Figure 2) and thus a larger portion of the radar wave penetrates into the ice which gives more volume scattering back to the radar. Furthermore, the surface is rougher so a larger amount of diffuse surface scattering is reflected back to the radar sensor compared to mostly specular scattering reflected away from the radar sensor of thin ice. The combination of rougher surface and lower dielectric constant should give multi-year ice the highest overall backscatter, which also is observed in the plots.
- Backscatter decreases with decreasing frequency. The surface becomes relatively smoother as the frequency decreases, thus the diffuse backscatter is decreased and specular reflection increase as the radar signal scatters away from the sensor. On the other hand, there is increased penetration depth with decreasing frequency. However, the air bubble dimensions are only comparable to C-band wave length and furthermore they are only concentrated to the upper layer of the sea-ice configuration. There is increased detection of deformed ice and ridges with decreasing frequency, with scattering arising from random orientation of deformed blocks and larger air voids within ridges, which become detectable with increased penetration.
- The backscatter for most ice types decreases with increasing incident angle (note only one point available for ice5) for all polarizations. MY ice shows this strongest, especially for L-band. For ice2 this trend is not as obvious. This decrease is expected due to increased specular scattering and reduced energy scattering back to the antenna.
- For many of the thin ice types the backscatter from vertical polarization is much larger than at horizontal polarization. This could be explained by assuming a combination of smooth surface and ellipsoidal brine inclusions aligned vertically in the sea-ice structure. This combination could explain the large difference between HH and VV.

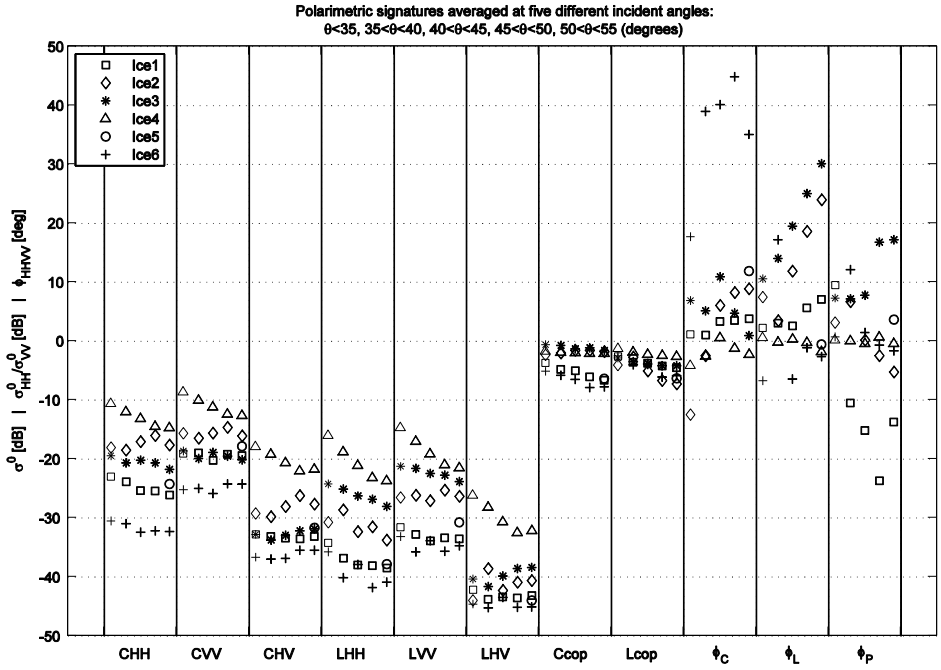

Figure 30: Summary of polarimetric signatures for all six ice types (Ice1: Lead ice 1-2 days old, Ice2: Lead ice 9-14 days old, Ice3: Lead/FY ice >15 days, Ice4: Multi-year ice, Ice5: Lead ice 2-3 days old, Ice6: Lead ice <1day old). The first six bins represents the backscatter of C- and L-band (HH, VV and HV pol), next two bins (Ccop and Lcop) are copolarized ratio (HH/VV) for C- and L-band. The last three bins correspond to the copolarized phase difference (ϕ_{HH-VV}) for C-, L- and P-band. Within each bin is the mean value of five different ranges of incidence angles calculated (see title text).

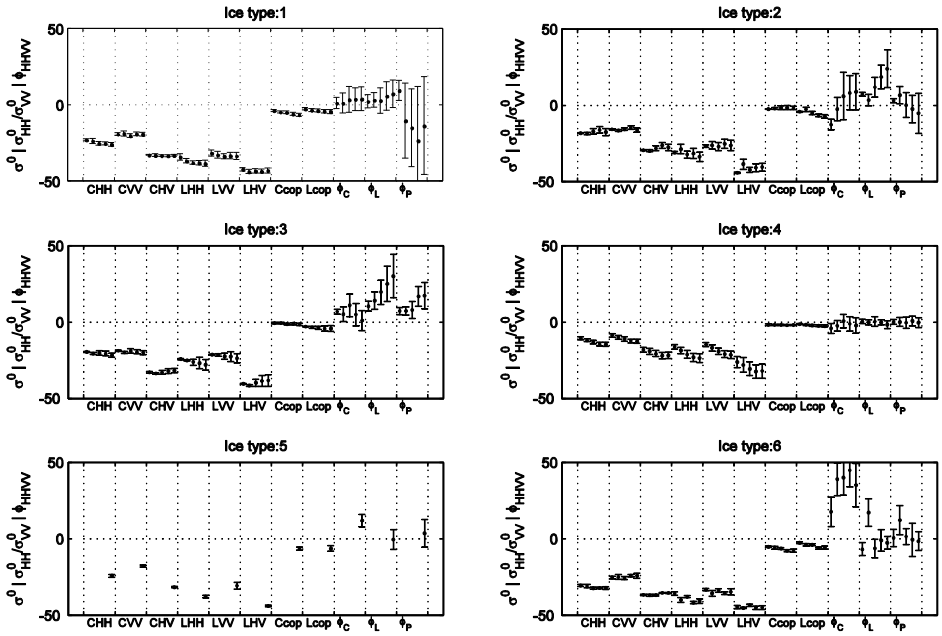

Figure 31: Standard deviations included, otherwise the same definitions as the figure above.

Regarding the thin ice types the following things are observed:

- A very interesting observation is that the backscatter for L-band tends to increase with the age and thickness of ice. This behavior is not observed for C-band; younger ice is observed to give higher backscatter than older thin ice, which is likely due to the development of frost flowers. C-band wavelength has a size comparable to the frozen ice clusters (Wolfgang Dierking, personal communication).
- The younger ice types (0-3 days) has a significantly higher copolar coefficient (VV>HH) for C-band, especially for larger incidence angles. The thin ice types have higher copolar coefficients than multi-year ice for L-band. However, the contrast is not as large as for C-band.
- In general most of the ice samples have phase differences within 0 and 10 degrees. 10 degrees is also the calibration uncertainty (Table 3). Multi-year ice has the lowest phase variability.
- Ice 1-2 days old has a very large variability and significant negative phase differences for the P-band.
- Ice that is hypothesized to be less than one day old (Ice6) has significant large C-band phases. Furthermore, it is the only ice type that has negative L-band phase differences. Note the relatively large variability.
- The L-band phases increase strongly with increasing incidence angle for ice 9-14 days and ice older than 15 days (ice3).
- Ice type 6 (youngest lead ice) has backscatter very close to the sensitivity of AIRSAR at C-band. Thus, it could be noise we are observing.

Figure 32 shows the relatively large C-band phase differences and the low backscatter for very young ice (Ice6). Also note the low L-band phases for many of the ice samples, which mainly has been observed for this ice type (see Figure 30).

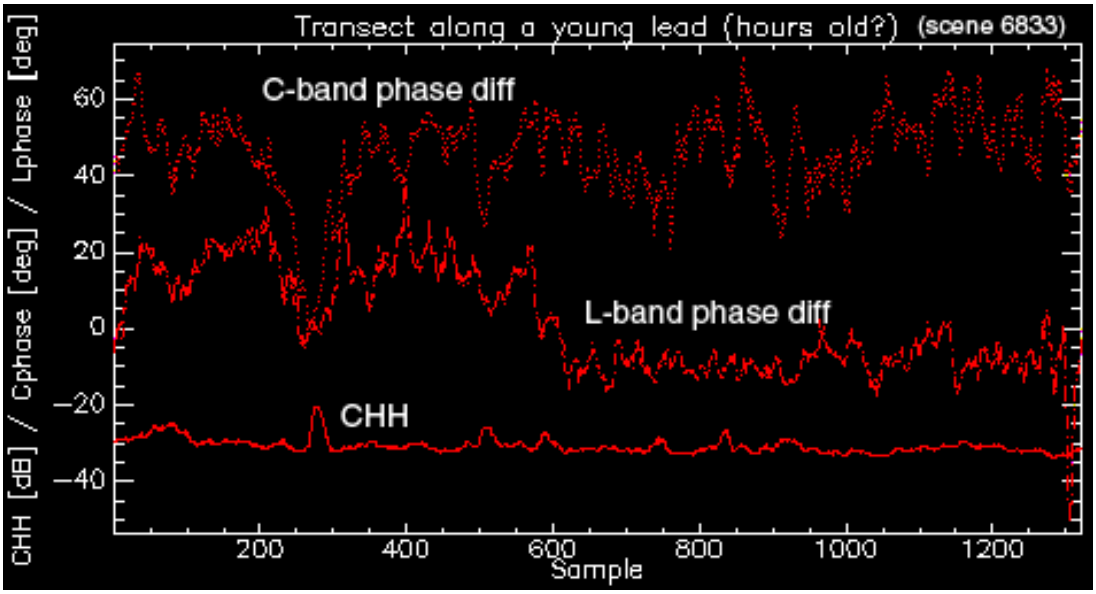

Figure 32: Signatures of a dark crack in a 1-2 day old lead in scene 6833.

It has been noted that the multi-year ice backscatter signatures in scene 6834 have high variability, see Figure 33. This has not been observed for the multi-year ice samples in the other two scenes. Apparently, the ice is deformed and many ridges have been included, causing much variation especially for L and P-band. However, note that the variations almost cancel in the copolarized ratio. The reason why the L-band backscatter for multi-year ice drops off so much in Figure 30 is that many of the samples in near range have been picked from scene 6834 where the ice is ridged.

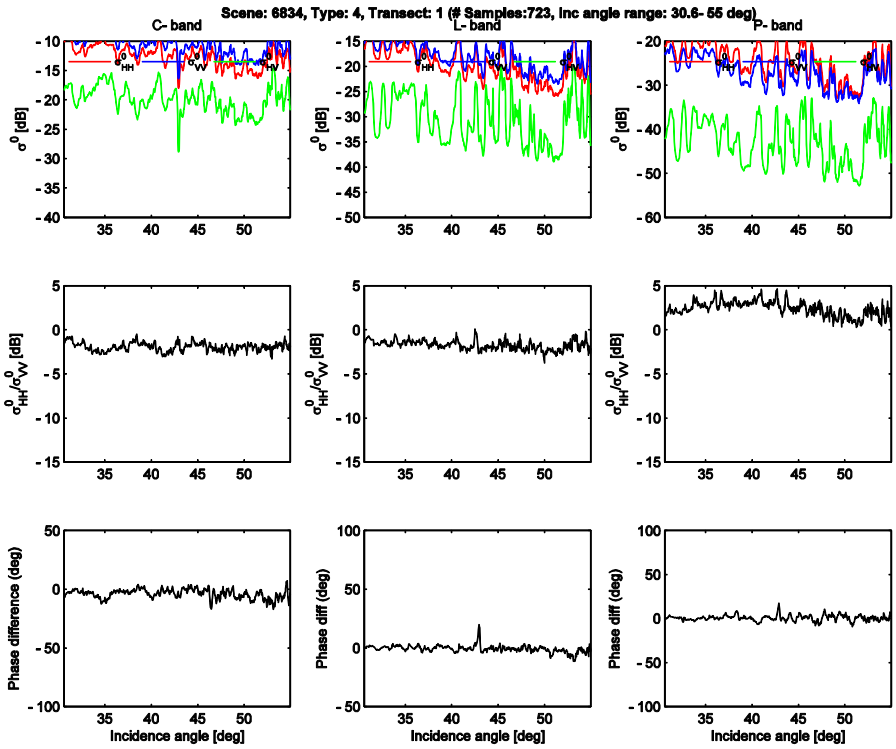

Figure 33: (Deformed) multi-year ice from scene 6834

7 Comparison with other studies

A lot of effort has been put on comparing the results of multi-year ice with previous results since it has well-known scattering characteristics and could thus be used as a reference to evaluate the quality of the data set in this study.

7.1 Multi-year ice

Most of the reported observations are from the Arctic AIRSAR campaign March 1988, but there also exist several reports based on for instance ERS (CVV-channel) and JERS (LHH-channel) all of which the observations in this study will be compared with. Since the data in this campaign were acquired in December and the previous campaign 1988 in March, it is interesting to know what differences to expect during this period of time. The spatial and temporal variability in the Arctic region was reported in a study using ERS data (Kwok, et al., 1994). Since ERS is a single-frequency, single-polarization system with low incidence angle range (19-26 degrees), a one-to-one comparison has not been possible; especially since no samples of this low incidence angle range has been picked in this analysis. However, the difference of the signatures acquired by ERS day of year (DOY) 315-365 (December included) and DOY 45-90 (March included) appears to be minimal; CVV appears to have the same mean value of -10 dB, but a slightly larger variation could be noted for December. It is expected that the differences of old ice signatures between different campaigns should not be big (Ben Holt, personal communication).

7.1.1 C-band

The backscatter of multi-year ice with various surface conditions (deformed and undeformed) are clustered between -14 dB and -8 dB over the range of incidence angle of ERS (19-26 deg), RADARSAT-1 (20-49 deg) and ENVISAT (14-45 deg) (Nghiem, et al., 2001). From some analyses (Nghiem, et al., 1995; Rignot, et al., 1994) of the polarimetric signatures of the very first AIRSAR campaign in the Beaufort Sea 1988 it is observed that the backscatter coefficients of C-band and the ones observed in this study agree pretty well, both in terms of absolute values and in the decreasing trend, see Figure 34. The reason for the relatively strong reflection (-8.7 dB) for CVV in this study at incidence angle around 30 degrees might be that samples in this range have been picked from scene 6834 which might have a lot of ridge-like features in near-range, so this response probably reflects the signatures of deformed multi-year ice. Due to the volume scattering and the relatively rough surface of multi-year ice, the backscatter should decrease slowly as the incidence angle increases (Nghiem, et al., 1995).

Our measured copolar ratios values fluctuate around -2.5 dB between 35 and 55 degree incidence angle and observations from 1988 data show copolar ratios between -1.0 dB and -2.4 dB (Drinkwater, et al., 1991).. Theoretically, the measured copolar ratio is a combination of surface and volume scattering contributions. According to Bragg scattering theory the contribution of surface scattering is predicted to be -3.5 dB to -4.4 dB in the incidence angle range 44-51 degrees but is shifted towards 0 dB if the volume scattering contribution due to the air bubbles in the upper layer of old ice (Drinkwater, et al., 1991).

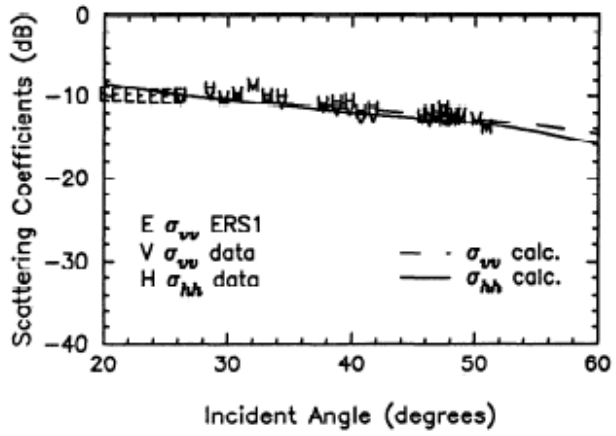

Figure 34: Scattering behavior at C-band based on models and actual observation from 1988 in the Arctic Sea (Nghiem, et al., 1995).

7.1.2 L-band

Moving over to L-band shows that our observations appear a bit lower than reported in other studies. The mean values of backscatter decreases from -16 dB to -24 dB and from -15 dB to -22 dB for LHH and LVV, respectively, within the incidence angle range 30-55 degrees, see Figure 30. Compare to reported range -14 dB to –18 dB for LHH (Rignot, et al., 1994) and about -12 dB to about -18 dB for LHH an LVV (Nghiem, et al., 1995). In the last reference the author also derives a theoretical scattering curve that show that LHH and LVV decreases from about -13 to -18 dB within 30-55 degrees incident angle range, see Figure 35. It appears as the backscatter is significantly smaller for two of the scenes: 6830 and 6831; about -20 to -25 dB between 35 and 55 degrees. The multi-year ice in scene 6834 shows larger values in accordance with other reported results, but on the other hand this region seems to be affected by a large amount of ridge-like features that could raise the mean backscatter level of especially L-band and P-band. The reason why the calculated mean values of LHH and LVV drops about 10 dB in a range of 25 degrees is because the samples of lowest incident angles are averaged from scene 6834 which probably is affected by ridges in near range. In for instance scene 6830 it is observed that LHH and LVV drop about 5 dB between 30 and 55 degrees, which is in accordance with for instance (Rignot, et al., 1994). In a recent study (Dierking, et al., 2006) it has also been reported values of LHH between -12 dB and -16 dB within the incident angle range 36 to 41 degrees, which is at least 3 dB larger than observed in our data. A difference of about 6 dB between data in this analysis and observations from previous mentioned reference could be found at an incident angle of 40 degrees. It is likely to assume that the AIRSAR L-band data have not been absolutely calibrated.

A look at copolar ratio for L-band shows that it varies between -1.4 dB and -2.6 dB between 30 and 55 degree incident angle. It has been reported from the Arctic campaign 1988 (Drinkwater, et al., 1991) copolar ratios of -3.9 dB to -4.2 dB within the incident angle range 43-51 degrees, which is significantly larger than our observed values. The author further shows that this is according to the Bragg scattering prediction that the air bubbles in old ice are too small to scatter efficiently at L-band and that most backscattering is due mostly to small-scale roughness. This is in accordance with a study on the response of L-band to sea-ice (Winebrenner, et al., 1995) that shows that copolar ratios align nicely around -4.0

dB. However, it has been found in another report (Nghiem, et al., 1995 p. 685), analyzing sea ice measurements from 1988, that the vertical and horizontal polarizations do not have this large difference in amplitudes; both the observations and the theoretical modeling show this, see Figure 35.

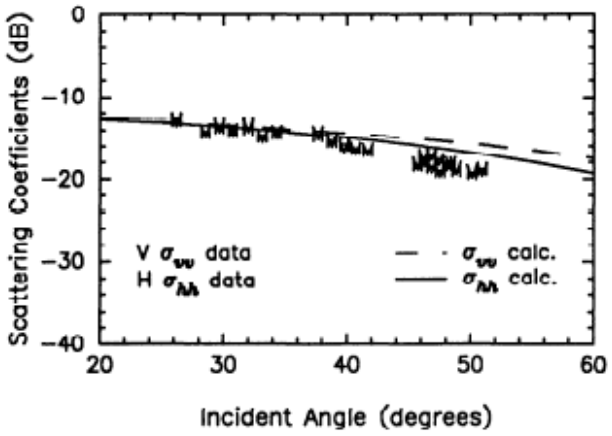

Figure 35: Scattering behavior at L-band based on models and actual observation from 1988 in the Arctic Sea (Nghiem, et al., 1995).

7.1.3 P-band

Reports on the scattering from P-band are pretty scarce in the literature. However, during the 1988 AIRSAR campaign data from the P-band were actually collected and reported (Drinkwater, et al., 1991). Nevertheless, the author points out that there exists some uncertainty due to the unknown HH-VV channel offset. The reported values of multi-year ice vary around -3.3 dB, which is some dB larger than what is expected from Bragg scattering theory. Our observations show large positive copolar ratios (HH>VV) which has not been encountered in the literature, thus, it has been assumed that this band not is calibrated. Furthermore, not much effect has been put on trying to calibrate this channel since it is known that there will be some uncertainty due to the significant variability of the copolarized amplitude balance from corner reflectors at the calibration site in the Rosamond dry lake (Freeman, et al., 1991).

The P-band phase information has been included even though the backscatter and copolar coefficients have been disregarded. It is assumed that P-band phase band is calibrated if it approaches zero degrees over multi year ice.

7.1.4 Phase

Theoretically, neither volume scattering from air bubbles (with no preferred direction in their structure) nor rough surface scattering from infinitely thick dielectrics produces copolar phases significantly different from zero (Winebrenner, et al., 1995). This is why the observed mean copolar phase over multi-year ice has been defined to zero degrees. Indeed the nice alignment along zero degree for multi-year ice is observed, especially for L- and P-band. The standard deviations for C-band are less than 5 degrees and slightly lower. This is within the range of ±6 degrees that both Bragg scattering and models for volume scattering from spherical air bubbles predict (Drinkwater, et al., 1991).

7.2 Thin ice / Lead ice

The thin ice polarimetric signatures have been compared with other studies in the Beaufort Sea 1988 in the Arctic and in the Weddell Sea 1994 in the Antarctica. The data from the 1988 campaign were acquired with the AIRSAR sensor and most of the studies use different notations of thin ice types. One of the studies found it useful to divide thin ice into two subgroups; ThFYa and ThFYb. ThFYa is young ice giving little backscatter, probably covered by Ice1, Ice2, Ice5 and Ice6 from this study, and ThFYb is more reflective ice, probably covered by frost flowers and should be compared with Ice2 in this study (Drinkwater, et al., 1991). Some lead ice data, notated Lead_1 and Lead_2, has been included from a study focusing on lead ice signatures at L-band (Winebrenner, et al., 1995). The Antarctica data were acquired with the SIR-C sensor mounted on the space shuttle. The ice types were subdivided into a number of groups but they have been grouped together here into a single one, ThFY, which covers young ice up to gray-while ice, e.g. a thickness range of 0 to 30 cm (Eriksson, 1998). ThFY could be compared with all thin ice groups in this study.

Differences in ice definition, incidence angle, system noise, weather and ice conditions make it difficult to compare the ice signatures from the different acquisitions. Ice that is thought to have developed some frost flowers (Ice2) has a copolar ratio of between -2.4 and -1.5 dB at C-band and should be compared with -0.4-0 dB for ThFYb. Apparently they do not really agree. Some ice types (ice6, ice1, ice5 and ice2 0-14 days) have high C-band copolar ratios that have not been reported in the Beaufort 1988 and Weddell Sea studies. The highest copolar value for the Weddell Sea data and Beaufort 1988 at C-band is -4.7 dB and -5.4, respectively, whereas -7.7 dB for the youngest ice in Beaufort 2004. It is difficult to compare the phases, but it appears as if they cluster around the same values. The exception is ice6 at C-band that gives a significant high phase difference, which not has been observed in the other studies. Note that the standard deviation of the phases from the Beaufort 1988 campaign is much higher than in the other studies.

Reports on P-band backscatter are pretty scarce. However, Ice type 1 in our study has some very low P-band phases which have not been found from the 1988 data.

Moving over to L-band also shows large variability among the classes. For instance the two leads from 1988 have some very high copolar ratios and low negative phases whereas thin sea-ice in the Antarctica has some very low copolar ratios (HH/VV =-0.3 dB). The large difference might be explained by a theory based on interference within the ice between downgoing and upgoing waves reflected from the sea-ice/seawater transition layer. This causes the copolar phases and ratios to oscillate as a function of ice thickness. The model shows that observations of positive copolar phases in thin ice would be roughly as probable as those of negative phases (Winebrenner, et al., 1995), see Figure 36. Very young ice, just a couple of hours old or a couple of cm thick (3-4 cm), is expected to have negative copolar phase, which also the young lead ice types in Beaufort 1988 shows. Also ice type 6 in this study that is hypothesized to be less than one day old is the only ice type that has negative phases. According to the model ice 1-2 days old, predicted to have a thickness of 8-13 cm, would have any phase between -40^{o} to 40^{o} and any copolar ratio between -12 and 0 dB. Large variability is also expected for the older thin ice types. However, for sea-ice with a broad distribution of thicknesses the model predicts an oscillatory behavior

up to a mean thickness of about 40 cm corresponding to ice older than 15 days (Figure 37). A very broad distribution would damp the oscillatory behavior very fast. It is hard to estimate the thickness distribution when lacking in-situ observations. However, the models show that we should expect large uncertainty in the determination of ice thickness if the age of the ice is not accurately known.

Table 13: Polarimetric signatures of thin ice from the AIRSAR campaigns in the Beaufort Sea in 1988 and 2004 and the SIR-C data take in the Weddell Sea 1994.

Frequency	Area	Type	Inc angle	HH/VV (dB)	ϕ_{HHVV} (mean)	ϕ_{HHVV} (std)
C	Beaufort 1988	ThFYa	45-48	-5.4 – -4.4	7 – 8	63–70
		ThFYb	41-44	-0.4 – 0	-4 – -2	23–27
	Beaufort 2004	Ice6	30-55	-7.7 – -5.2	18 – 35	10–14
		Ice1	30-55	-6.6 – -3.8	1 – 4	4– 9
		Ice5	50-55	-6.4	12	4
		Ice2	30-55	-2.4 – -1.5	-13 – 9	1–13
		Ice3	30-55	-1.6 – -0.7	1 – 11	2 –8
	Weddell 1994	ThFY	30-33	-4.7 – -1.5	-3 – 12	6–31
L	Beaufort 1988	ThFYa	45-48	-5.7 – -4.9	3 – 6	46–67
		ThFYb	41-44	-5.7 – -5.2	17 – 20	26–39
		Lead_1	37-45	-9.4 – -4.0	-10 – -50	-
		Lead_2	46-49	-7.4 – -4.0	-10 – -35	-
	Beaufort 2004	Ice6	30-55	-6.1 – -2.6	-7 - 17	4–9
		Ice1	30-55	-4.5 – -2.7	2 – 7	4–9
		Ice5	50-55	-6.3	0	6
		Ice2	30-55	-7.2 – -2.7	7 – 24	1–12
		Ice3	30-55	-4.2 – -3.0	11 – 30	3–14
	Weddell 1994	ThFY	30-33	-4.0 – -0.3	-8 – 18	9–38
P	Beaufort 1998	ThFYa	45-48	-5.4 – -3.9	4 – 13	41 – 52
		ThFYb	41-44	-4.6 – -3.9	-4 – 4	42
	Beaufort 2004	Ice6	30-55	-	-2 – 12	5 – 11
		Ice1	30-55	-	-24 – 9	7 – 35
		Ice5	50-55	-	4	9
		Ice2	30-55	-	-5 – 7	1 – 13
		Ice3	30-55	-	7 – 17	2 – 9

From a study using fully polarimetric data from the Okhotsk Sea it is proposed that both L-band backscatter and copolar ratio could be an estimator of the thickness of sea-ice (Nakamura, et al., 2005), see Figure 38 and Figure 39. Ice thicker than 15 cm has been included. Our thin ice types estimated to be 15 – 40 cm thick all have higher copolar ratios than the one reported in the Okhotsk study, so it appears as if there are significant differences in the physical properties of the sea-ice. According to models, a change in air bubble radius with 1 mm could increase the backscatter with about 10 dB (Winebrenner, et al., 1989 pp. 155-157). However, it is not clear if this is the explanation of the behavior of thin ice.

From the literature it appears as if the C-band backscatter can span over a very wide range, from -35 dB for very smooth and thin ice grown in a laboratory (Figure 40) to -5 dB for thin ice with frost flowers (Dierking, et al., 2006 p. 964). In this study the range spans from -32 to -15 dB for C-band (HH and VV).

During the International Arctic Ocean Expedition in 1991 (IAOE'91) in-situ radar measurements were performed on different thin ice types (dark and light nilas and pancake ice), see Figure 41 (Beaven, 1995). From these observations it appears as ice6 (< 1 day old) corresponds rather well to the measurements on dark nilas (<5 cm), ice1 and ice5 (1-3 days) corresponds to light nilas (>5 cm) and ice2 (9-14 days) and ice3 (>15) corresponds to pancake ice (10 – 20 cm). However, it is unclear whether ice older 15 days still has pancake features on the ice.

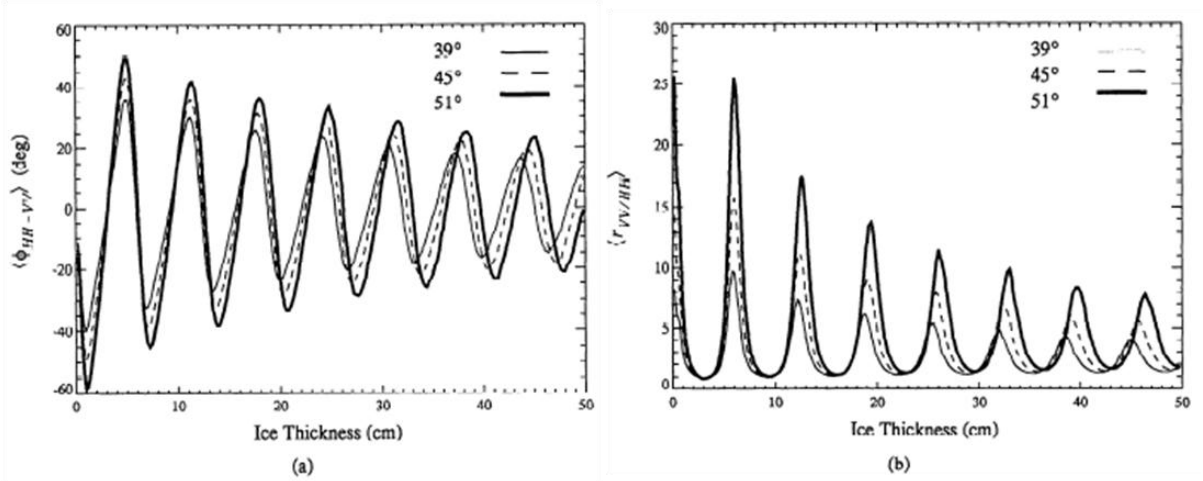

Figure 36: Plots of (a) theoretical copolar phase and (b) ratio versus ice thickness at three incidence angles with data typical of AIRSAR and Arctic sea ice. A single sea-ice thickness is assumed (Winebrenner, et al., 1995).

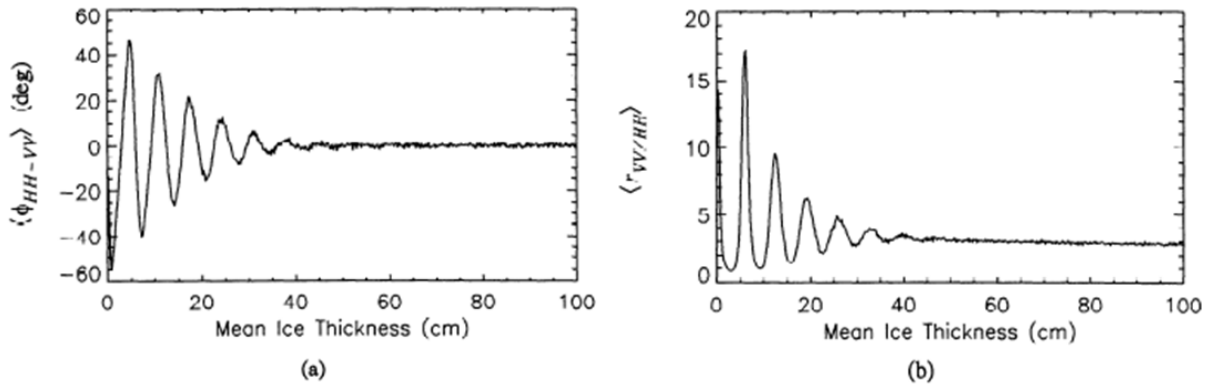

Figure 37: Plots of (a) copular phase and (b) ratio, versus mean ice thickness, at L-band of the JPL AIRSAR and 45^{o} incidence angle. The distribution of sea-ice thicknesses is broad (Winebrenner, et al., 1995).

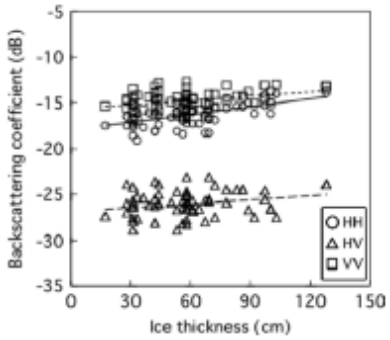

Figure 38: Relationship between ice thickness and the backscattering coefficients (L-band) from a study in the Okhotsky Sea (Nakamura, et al., 2005).

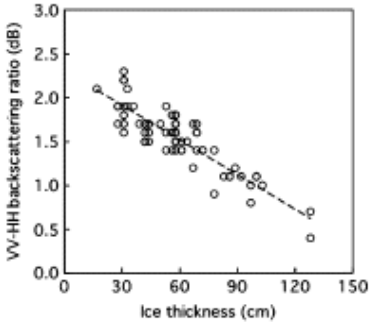

Figure 39: Relationship between ice thickness and the VV-HH backscattering (L-band) from a study in the Okhotsky Sea (Nakamura, et al., 2005).

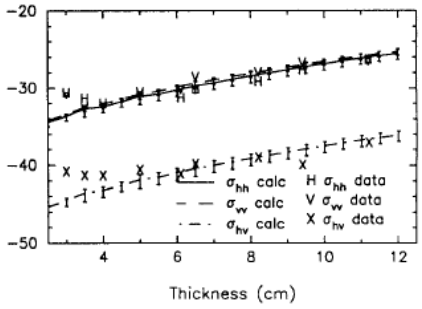

Figure 40: C-band backscatter at 35^{o} incidence angle of thin ice grown under laboratory conditions. Capital letters represent measured data, and curves are model calculations with a Gaussian thickness distribution with mean thickness from 2.5 to 12 cm. The vertical axel shows the backscatter (dB) (Kwok, et al., 1998).

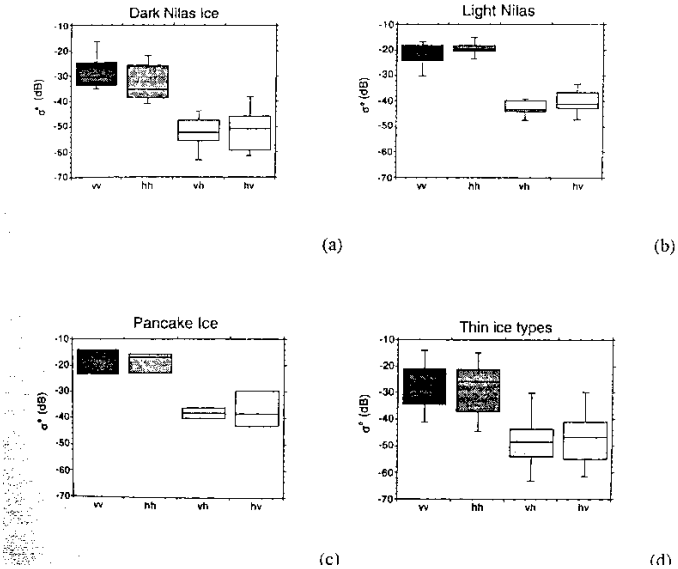

Figure 41: IAOE'91 seasurements of C-band backscatter versus polarization from young first-year ice type: a) dark nilas, b) light nilas, c) pancake ice, and d) all young first-year ice types combined. The center line is the median value measured. The top and bottom lines of each of the shadow boxes mark the ±25% points in the distribution and the extended lines (when shown) mark the ±45% points in the distribution (Beaven, 1995).

8 Classification

8.1 Combination of parameters

All possible combinations of the different parameters have been plotted in order to find some combinations that might be useful for classification (See Appendix G). Figure 42 shows an example of how the samples are spread out in the CHH and CVV plane. Note that all samples over all incidence angles have been included, even those that might be affected by for instance ridges. Multi-year ice gives the highest backscatter and the youngest ice (ice6) has the lowest measured values. This is typically observed for most backscatter combinations. In-between the oldest and youngest ice, the other ice types form clusters that have some overlap. It is observed that ice 1-2 days old (Ice1) and 2-3 (Ice5) are difficult to separate since they overlap almost entirely for all combinations. However, the variability of ice5 seems to be considerably lower than of ice1 but this could be explained by the fact that only about 400 samples have been used for ice5 compared to 7800 samples for ice1. A simple classifier that tries to find decision boundaries in a plane would have difficulties classifying these two classes, so the best result might be if these two classes are combined into a single one. Two-parameter combinations using C-band channels generally show higher backscatter for 9-14 days old ice than ice older than 15 days. However, this is thought to be due to the evolution of frost flowers which causes samples to partly overlap multi-year ice. It appears hard to implement a classifier based on two-parameter combinations, trying to discriminate ice of age 1-2 days, 2-3 days, 9-14 days and ice older than 15 days without too much misclassification error.

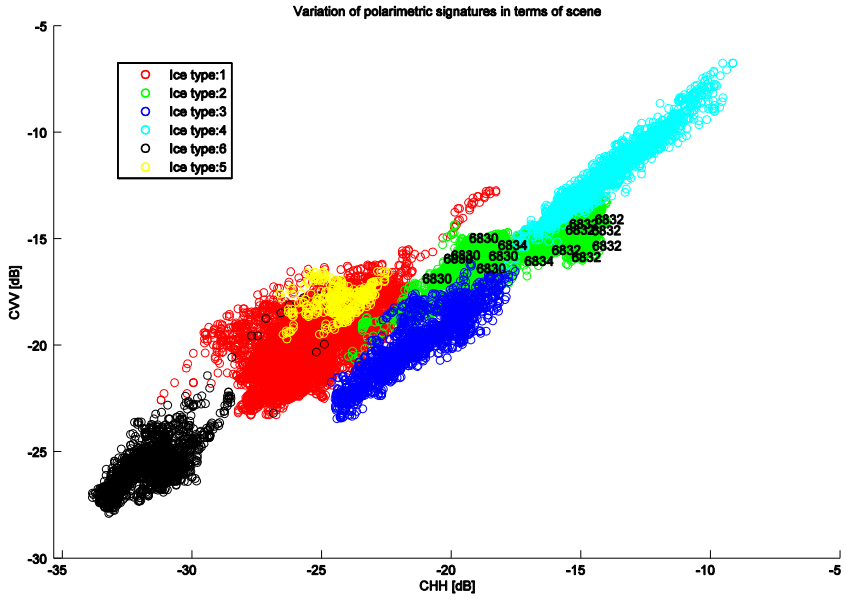

Figure 42: Distribution of samples in the CHH-CVV plane. Some samples of ice type 2 have large backscatter; they have been picked from scene 6832.

One way to improve a classifier is to understand what causes the spread of the samples. Figure 43 plots the incidence angle dependence of the samples. It is expected to see higher backscatter in near range than in far range. Appendix H divides all two-parameter combinations in ranges of 5^o: 30^o to 35^o, 35^o to 40^o, 40^o to 45^o, 45^o to 50^o and 50^o to 55^o. It is observed that the clusters are more well-defined, especially for the incidence angles less than 35^o, where we have fewer samples.

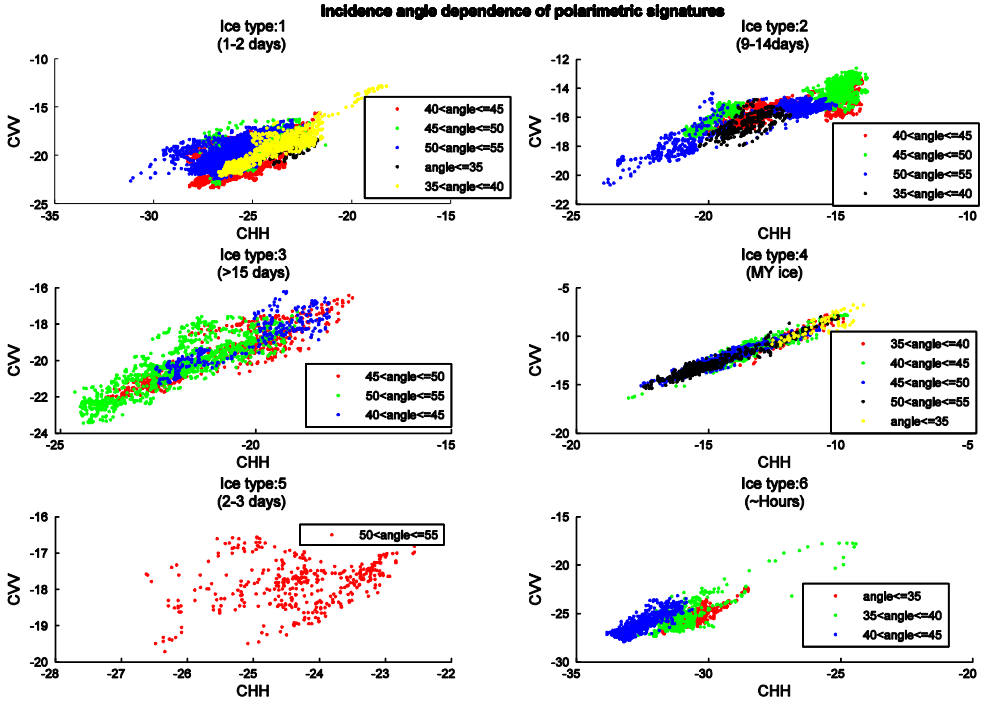

Figure 43: Incidence angle dependence of the different ice types using the combination CHH and CVV.

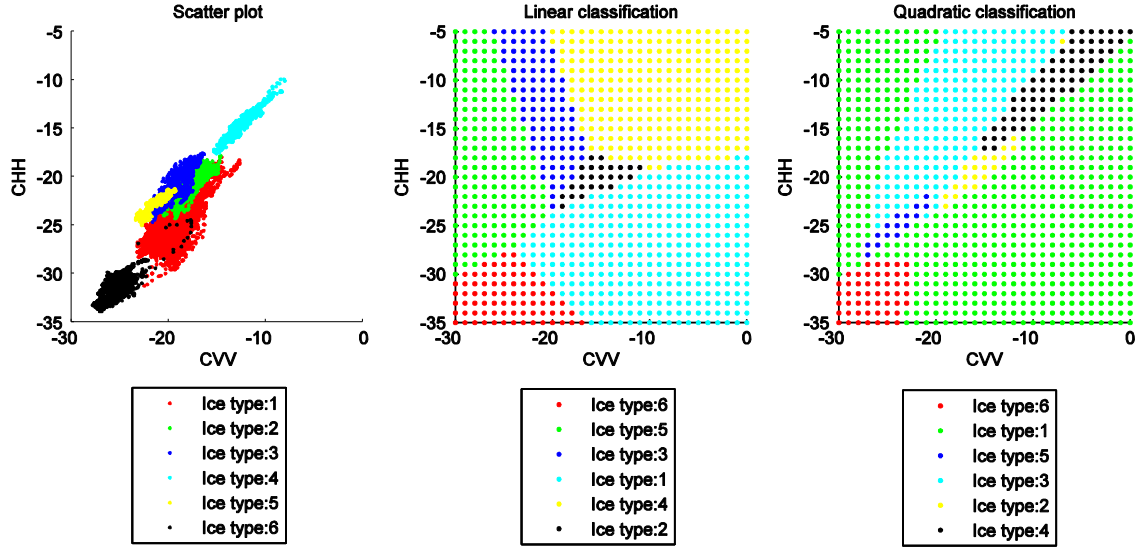

Figure 44: Result of classifying in CHH and CVV plane using linear and quadratic methods.

8.2 Implementation

Matlab has a built-in function, classify, that has been used as a classifier in this project. Two different discriminant methods have been used and compared: linear and quadratic. The linear function divides the plane in straight lines whereas the quadratic function divides the plane with parabolic curves. Both methods use likelihood ratios to assign observations to groups. Figure 44 shows an example where the different ice types in the CHH-CVV plane have been classified, using linear and quadratic discriminant methods. The total misclassification error has been calculated by comparing the classified classes and the actual ones and dividing the number of misclassified pixels by the number of pixels for all classes. It was found that the quadratic classifier generally performs better and thus it has been used.

8.3 Separation of different combinations

The performance of all possible combinations (over all incidence angles) has been summarized in Appendix I. Table 14 shows some of the best and worst combinations, where the best ones are CHV combined with CHH/CVV and CHV combined with LHH which just results in 7.7% and 8.6% misclassified pixels, respectively. Note that using only C-band data or combining particular C- and L-band channels give about the same accuracy. Using the C-band crosspolarized channel together with another channel appears to give good separation of the ice types, since the five most accurate combinations include the CHV channel. Using single-polarization classification usually performs worse than using two-parameter combinations. For instance classification based on only L-band such as LHH, LVV or LHV results in 61%, 69% and 70% misclassified pixels, respectively. Single polarization C-band achieves better, in particular the crosspolarized channel CHV performs best by misclassifying 22% of all pixels. All two-parameter combinations based on single frequency L-band misclassify more than 50% of the pixels. Multi-year ice and the youngest ice type (ice6) are typically easiest to classify, since they have very high and low backscatter, respectively. The other ice types partly overlap each other for most combinations. The best combination (CHV and CHH/CVV) misclassifies 1-2 days, 2-3 days, 9-14 days and ice older than 15 days with about 8%, 5%, 11% and 11%, respectively. Classification based on the C- or P-band phase information does not appear very good due to the large phase variations and overlap between the different classes. However, combining L-band phase and CHV results in about 12% overall misclassified pixels.

It must be pointed out that the cross-polarized backscatter for thin ice is very low, in the extreme case around -37 dB at C-band. If CHV not would be considered as reliable, CHH combined with LHH/LVV, CVV or CHH/CVV provides the best classification accuracies of about 86%. CHH combined with LHH/LVV misclassifies ice older than 15 days rather much whereas CHH combined with CVV provides worse accuracy of classifying ice that is 1-2 days old.

Figure 45 shows the separation of the different ice types using two combinations of parameters that give the highest accuracy, one combination using CHH and LHH/LVV and also one of the combinations with worst performance (LHH and LVV). The lines in the plots indicate the standard deviation of the polarimetric parameters for each ice types. Note the good class separation for three of the combinations compared to combining LHH and LVV. It has been reported that if one of the copolar channels of a certain frequency is chosen, it is not gained much by also using one of the other (Eriksson, 1998 p. 39).

Table 15 shows the confusion matrix and the producer's and user's accuracies for CHV combined with CHH/CVV, which has been determined as the best combination, misclassifying least pixels. The confusion matrix tells how many pixels of a certain ice type that is accurately classified or misclassified. Rows and columns list the actual and classified ice types, respectively. The main diagonal of the matrix lists the correctly classified ice types. The producer's accuracy is the probability of a reference pixel being correctly classified and the user's accuracy indicates the probability that a pixel classified on the map actually represents that category on the ground (Congalton, 1991). Note that a producer of a classification map can claim that an area that was ice type 5 was identified as such for 95% of the pixels, but a user of this map will find that only 41% of the pixels of an area that the map says are ice type 5 actually is ice type 5. Many of the pixels of ice type 1 are misclassified as ice type 5 which leads to low user's accuracy for this group. This is expected for classes with relatively few pixels. Even though the overall accuracy (total number of accurately classified pixels divided by total number of pixels) is as good as 92% some consideration must be used. Since ice type 1 has most of the pixels, the accuracy of classifying this ice type will greatly affect the overall accuracy for all pixels. There are methods to determine a normalized accuracy, regardless of the number of pixels for each class (Congalton, 1991), but this is left for future work and improvements.

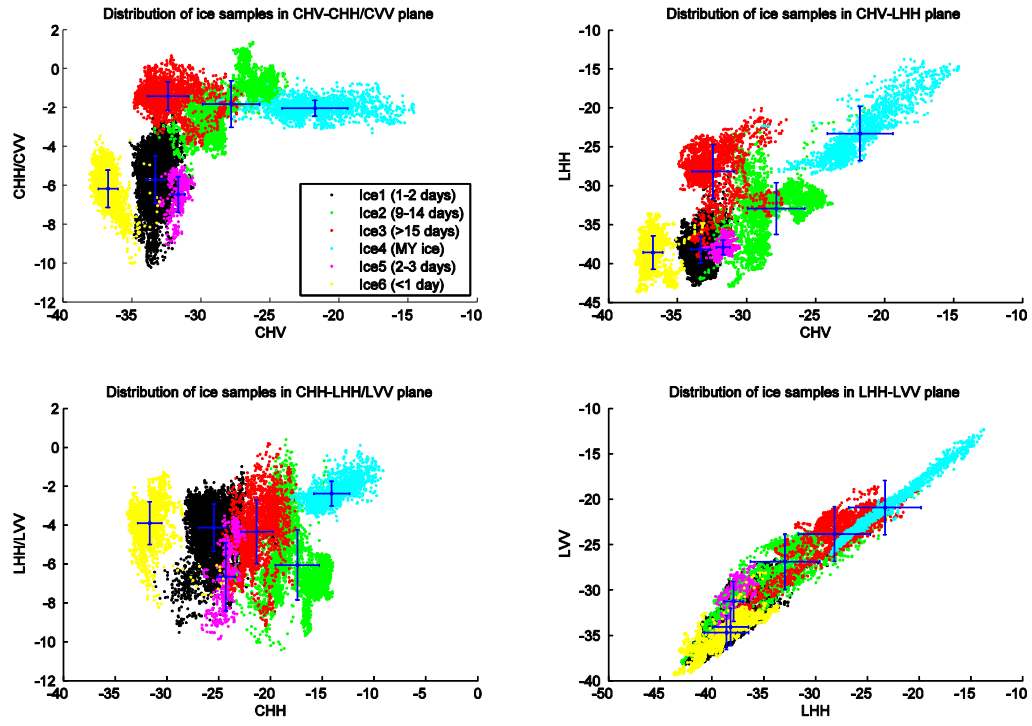

Figure 45: Separation of ice types using different combinations of parameters. The lines centered over each cluster denote standard deviation.

Table 14: Percentage of misclassified pixels for various combinations of parameters

Combination		Misclassification							Comment
		Ice1 1-2 days	Ice2 9-14	Ice3 >15 days	Ice4 MY ice	Ice5 2-3 days	Ice6 <1 day	All pixels	
CHV	CHH/CVV	8.3%	10.8%	10.5%	2.6%	5.2%	1.3%	7.7%	Best comb.
CHV	LHH	9.3%	11.8%	12.4%	2.3%	4.9%	1.7%	8.6%	
CHH	CHV	11.9%	13.6%	18.5%	2.8%	5.9%	1.0%	10.9%	
CHV	ϕLHHVV	13.4%	10.3%	24.9%	0.3%	7.9%	1.7%	11.5%	Utilizing phase
...					...				...
CHH	LHH/LVV	15.5%	18.4%	22.2%	0.3%	12.0%	1.7%	13.8%	
CHH	CVV	24.5%	10.9%	6.4%	3.9%	7.1%	1.6%	14.4%	
CHH	CHH/CVV	24.5%	10.9%	6.4%	3.9%	7.1%	1.6%	14.4%	
...					...				Only one parameter
CHV	CHV	11.5%	17.9%	93.8%	4.3%	8.8%	2.5%	21.6%	
...					...				...
LHH	LHH	84.3%	36.1%	43.7%	34.4%	21.6%	67.6%	60.9%	
LVV	LVV	85.5%	73.9%	58.4%	41.7%	54.5%	37.8%	69.3%	Worst combinations
LHH/LVV	LHH/LVV	85.7%	83.2%	99.3%	7.9%	39.8%	47.9%	73.9%	
ϕCHHVV	ϕCHHVV	100%	87.1%	83.3%	18.4%	15.7%	19.7%	76.3%	

Table 15: Confusion matrix for CHV combined with CHH/CVV. The values denote the number of pixels.

		Classified ice types						Total	Producer's Accuracy
		Ice1 1-2 day	Ice2 9-14 days	Ice3 >15 days	Ice4 MY ice	Ice5 2-3 days	Ice6 <1 days		
Actual ice types	Ice1 1-2 day	7114	79	48	0	516	1	7758	92%
	Ice2 9-14 days	23	3264	225	111	35	0	3658	89%
	Ice3 >15 days	10	230	2052	0	0	0	2292	90%
	Ice4 MY ice	0	47	0	1765	0	0	1812	97%
	Ice5 2-3 days	21	0	0	0	386	0	407	95%
	Ice6 <1 days	26	0	0	0	0	1915	1941	99%
	Total	7194	3620	2325	1846	937	1916		
	User's Accuracy	99%	90%	88%	96%	41%	100%		

8.4 Previous results

In a study of sea-ice from the Arctic campaign in March 1988 it was analyzed which classifier that best separates the ice types thin ice, first-year ice, multi-year ice, first-year rubble and ridges and compressed first year ice. The results showed that using a fully polarimetric C-band classifier the overall classification had an accuracy of 80%, which is only 2% better than a classifier operating on CHH and CVV data only. At L-band, the fully polarimetric classifier gives a classification accuracy of 83% and is 1% worse than a classifier working on LHH and LVV only. The best performance was provided by a two channel, two frequency classifier using LHH and CVV or LHV and CHH with classification accuracies of 89%. It was also shown that the addition of P-band data degrades classifier performance, probably because the return from thinner/smoother ice is close to the noise floor (Henderson, 1998), (Rignot, et al., 1994). No further discrimination of thin ice was done, thus a direct comparison with the results in this study could not be done.

Radar backscatter measurements of thin ice in the Arctic Sea were performed as part of the International Arctic Ocean Expedition in 1991 (IAOE'91). It was reported that copolarized and crosspolarized C-band channels could be related to ice types with different thickness (see Figure 46 and for definitions Table 1). Using two channels instead of one improves the separation of some of the grease/frazil and dark nilas categories and light nilas. Although there is some mixing between classes, the use of dual-channel backscatter at C-band may be useful for classification and determination of thin ice thickness. Figure 47 shows the separation of thin ice using HH and VV-polarized C-band backscatter. Very thin ice such as grease/frazil ice separates well from the other thicker thin ice types, which also has been observed in this study. However, there are much mixing between the other ice types and it does not appear that thin ice thickness can be obtained from these channels (Beaven, 1995).

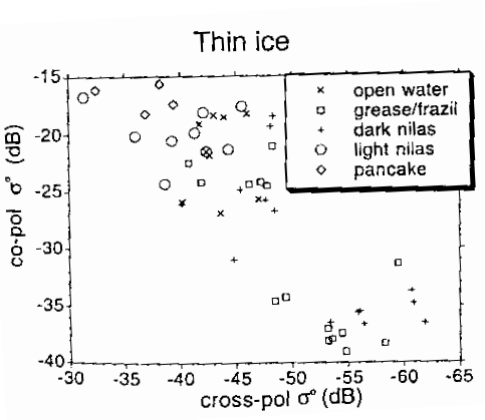

Figure 46: Copolarized and cross-polarized backscatter for thin ice categories (From IAOE'91). (Beaven, 1995)

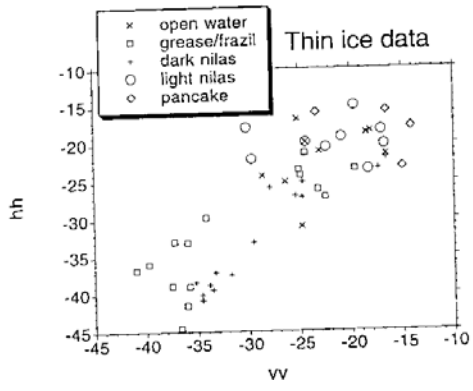

Figure 47: Backscatter from HH polarization versus VV polarization for thin ice categories. (Beaven, 1995)

In a study focusing on signatures of thin ice types in the Weddell Sea in Antarctica it was proposed that the most favorable two-parameter combination for a classifier appears to be either the correlation between the L-band HH and VV-polarized channels (ρ_{hhvv}) and LVV or CHH/CVV and LVV (Eriksson, 1998). Since the correlation between different polarizations has not been considered in this report, the first combination that the author mentions has not been evaluated for our data. Figure 48 and Figure 49

show the separations of the thin ice types. Three groups of thin ice types have been identified (type a, b and c) and they appear dark in both C-band L-band images. It was reported that the signatures differs somewhat between the signatures from the Arctic AIRSAR campaign in 1988. This has also been verified in a previous chapter as well as differences to the signatures observed in this study. The author points out that the differences could be due to the fact that on average the Antarctic ice is more saline and less deformed than the Arctic counterpart, but may also depend on differences in incidence angle, system noise, wind, weather, ice conditions and how the different ice types are defined (Eriksson, 1998).

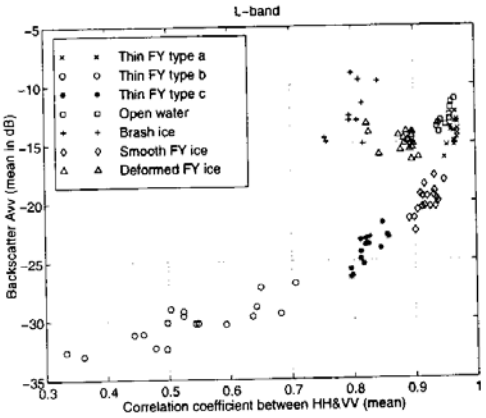

Figure 48: L-band VV backscatter versus ρ_{hhvv}. Data from Weddell Sea 1994 (SIR-C mission). (Eriksson, 1998)

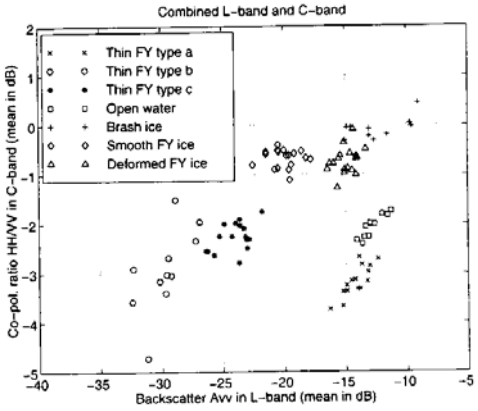

Figure 49: LHH versus CHH/CVV. Data from Weddell Sea 1994 (SIR-C mission). (Eriksson, 1998)

8.5 Results of classification

Figure 50 shows some result of classification using some two-parameter combinations for one region in scene 6830. The two best combinations CHV and CHH/CVV as well as CHV and LHH are included. In addition two combinations not including the cross-polarized channel are analyzed: CHH and LHH/LVV as well as CHH and CVV. Furthermore, LVV and CHH/CVV which was determined as giving good thin ice separation of Weddell sea-ice and CHH and LHH which were evaluated as good separators of principal ice types in the Beaufort Sea 1988. Also the best combination including phase data have been included.

Most of the combinations appear to give pretty good results when comparing with the actual SAR image. Obviously it is impossible to determine which combination that is most accurate since we do not know exactly for all pixels what the ice type should be, due to lack of in-situ observations. Classification of multi-year ice seems to give good results in most cases. The exception is LVV combined with CHH/CVV where bands of ice older than 15 days appear at regions that should be multi-year ice. This artifact may be due to effect described in section 4.3.2. In future work when this banding effect has been resolved the result should look better. However, note that some parts in the middle of the lead have been misclassified as young ice of 1-2 days old. From the CHH channel this does not seem to be the case. In addition some regions in the lead that should be older than 15 days are misclassified as 9-14 days. The dark lead in the CHH channel determined to be about 1-2 days old appears to be best represented using the combinations CHH and LHH/LVV as well as CHH and CVV. CHV and CHH/CVV appears to classify a slightly larger lead than what could be observed from the CHH channel. LVV and CHH/CVV or CHH and

LHH misclassifies a large part of the lead as ice younger than one day or ice between 2-3 days old, respectively. CHV and CHH/CVV as well as CHH and CVV appear to give good visual results.

The proportion of each classified ice type for each combination is shown in Table 16. The coverage of multi-year ice is about 30% and there is not much variation among the combinations. However, the variations are larger for the other ice types and it is tricky to tell which one should be most accurate. CHV combined with $\phi_{CHH-CVV}$ has the highest proportion of ice1 classified pixels, which probably is too high since some regions observed as older than 15 days is misclassified as 1-2 days. Combining LVV and CHH/CVV appears to classify a too large portion as ice 9-14 days old. It is also the combination that finds some percentage of young ice (<1 day) in the dark lead, but probably this is a misclassification since the age has been verified by Radarsat imagery to be 1-2 days old.

Table 17 shows the signatures averaged over all incidence angles of each derived ice type. The mean value and standard deviations have been calculated from the ensemble of pixels of each classified ice type for each combination of parameters.

Note that no binning of incidence angles of different ranges has been performed; the result of the classification is an attempt to separate all ice types using samples over all incidence angles. Of course this smears out the signatures and causes significant overlap. An improvement would be to divide the polarimetric signatures in a certain number of regions where it is observed that the signatures do not vary significantly (see for instance the work by (Rignot, et al., 1994)).

Table 16: Percentage of pixels covered by each ice type for each combination

Combination	Ice type 1 (1-2 days)	Ice type 2 (9-14 days)	Ice type 3 (> 15 days)	Ice type 4 (MY ice)	Ice type 5 (2-3 days)	Ice type 6 (< 1 day)
CHV and CHH/CVV	9%	41%	19%	28%	3%	0%
CHV and LHH	10%	38%	16%	28%	9%	~0%
CHH and LHH/LVV	7%	31%	28%	29%	5%	0%
CHH and CVV	8%	44%	19%	27%	3%	0%
LVV and CHH/CVV	9%	46%	8%	32%	1%	4%
CHH and CVV	6%	40%	21%	28%	6%	~0%
CHV and $\phi_{CHH-CVV}$	13%	37%	16%	27%	6%	~0%

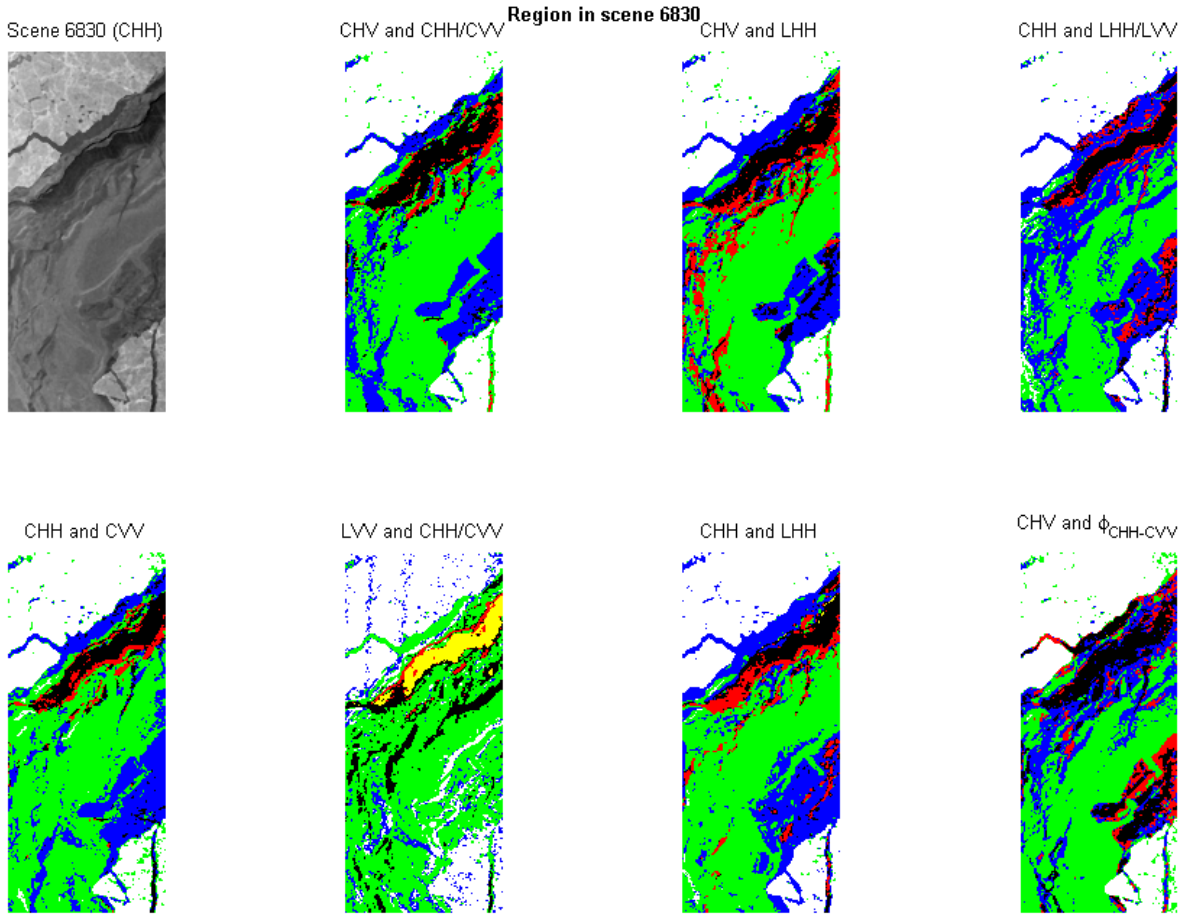

Figure 50: Results of quadratic classification using combination of various parameters. Legend: White – MY ice, Black – 1-2 days old lead, Red – 2-3 days old lead, Green – 9-14 days old lead, Blue – >15 days old lead, Yellow – <1 day old lead

Table 17: Signatures (mean value and standard deviations) derived from the classified ice types

Combination	Ice type 1 (1-2 days)	Ice type 2 (9-14 days)	Ice type 3 (> 15 days)	Ice type 4 (MY ice)	Ice type 5 (2-3 days)	Ice type 6 (< 1 day)
CHV and CHH/CVV	-33.0±0.6 dB -5.0±1.4 dB	-29.3±1.1 dB -2.8±0.8 dB	-31.7±1.2 dB -1.9±0.6 dB	-20.1±2.4 dB -2.0±0.5 dB	-31.4±0.6 dB -5.2±1.0 dB	Not classified
CHV and LHH	-33.0±0.5 dB -37.5±2.1 dB	-29.2±1.0 dB -32.5±3.5 dB	-31.5±1.3 dB -28.2±3.3 dB	-20.1±2.4 dB -20.5±3.4 dB	-31.5±0.6 dB -37.3±1.3 dB	-35.0±0.1 dB -36.3±0.6 dB
CHH and LHH/LVV	-25.1±1.3 dB -3.8±1.1 dB	-19.1±1.1 dB -6.1±1.5 dB	-20.8±1.3 dB -4.0±1.7 dB	-13.2±1.9 dB -2.3±0.5 dB	-23.6±1.0 dB -4.9±1.4 dB	Not classified
CHH and CVV	-24.8±1.7 dB -19.7±1.0 dB	-19.3±1.3 dB -16.5±1.0 dB	-21.3±1.6 dB -19.4±1.4 dB	-13.0±1.8 dB -11.0±1.7 dB	-23.1±0.6 dB -17.9±1.3 dB	Not classified
LVV and CHH/CVV	-33.2±2.3 dB -3.6±1.0 dB	-28.2±2.3 dB -2.6±0.9 dB	-22.9±2.5 dB -1.6±0.6 dB	-18.9±3.2 dB -2.1±0.4 dB	-29.0±2.2 dB -6.6±1.3 dB	-35.4±1.1 dB -6.2±0.5 dB
CHH and CVV	-24.9±1.7 dB -19.7±1.3 dB	-19.3±1.2 dB -16.6±1.0 dB	-20.9±1.7 dB -18.4±1.7 dB	-13.1±1.8 dB -11.1±1.8 dB	-23.3±1.0 dB -19.2±1.3 dB	-29.1±0.4 dB -19.9±0.8 dB
CHV and $\phi_{CHH-CVV}$	-33.1±0.5 dB 4.1±9.6 ^{o}	-29.0+1.1 dB -4.8±16.1 ^{o}	-31.2±0.8 dB -1.9±5.9 ^{o}	-20.1±2.3 dB -1.2±5.9 ^{o}	-31.6±0.6 dB 10.9±4.2 ^{o}	-34.5±0.2 dB 29.8±2.8 ^{o}

9 Discussion and conclusions

Much work has been carried out trying to evaluate the quality of the data of the 2004 campaign. The signatures of multi-year ice have been compared to the 1988 campaign and with theoretical predictions. Multi-year ice has well-known signatures and they should not change significantly throughout the winter period. It was found that the C-band data are well calibrated; absolute backscatter data correspond to what has previously been reported and the calculated relative backscatter coefficients (HH/VV) are between values observed in the 1988 campaign. P-band data show HH larger than VV backscatter coefficients which neither is expected from theory nor observed from the very few observations in 1988. It was decided to exclude P-band backscattering observations in this study, due to the scarce information available about the scattering behavior and the fact that it is hard to calibrate. Initially in the project we encountered problem with the L-band data. It was observed that vertical polarization was about 15 dB larger than horizontal polarization. It was concluded that 12 dB of the VV channel was attributable to a hardware artifact. Correcting for this error showed copolar ratios (HH/VV) around -3 dB for multi-year ice for samples in scene 6830 and 6831, within 1 dB of what has been reported from the 1988 campaign and what is expected from theory. However, we still note that the absolute backscatter coefficients are significantly lower (about 6 dB) than what has previously been reported. One speculation is that rather than lower VV with 12 dB, VV needs to be suppressed by 6 dB and HH increased by 6 dB. This would still give the same copolar ratio. More work is needed in order to understand and resolve this issue. For instance one could have a look at the range spectra. The phases for all three frequencies should be considered as calibrated since they have been adjusted to zero degrees over multi-year ice.

In addition to multi-year ice, we have identified and examined several stages of new and young ice in the AIRSAR scenes and RADARSAT imagery has been used to track back in time to find sea-ice openings. The thickness of a sea-ice layer could be estimated from its age by a known empirical relationship based on freezing degree days with temperature records from the IABP/POLES data set. Lead ice less than one day old should have a thickness between 0 and 8 cm. Lead ice 1-2 days and 2-3 days should have a thickness of 8-13 cm and 12-15 cm, respectively. Ice 9-14 days old have a thickness between 25 and 36 cm but the class may in fact have a large distribution of different thicknesses due to rafting processes piling up ice floes on each other. The large variability of older thin ice such as the ice type 9-14 days old motivates the division of this class into subclasses in future work. Several bands of different C-band backscatter have been identified as well as characteristic regions with low C-band copolar phases. The bright bands observed in scene 6830 may not be frost flowers but could be bands of brash ice formed by the observed ice sheet motions (Wolfgang Dierking, personal communication).

Ice type 6, found in a few 1-2 days old leads, that is thought to be only a couple of hours old has the lowest backscatter coefficients for C- and L-band. This ice type also has significantly larger copolar phases for C- band than the other ice types and is the only ice type that shows negative phase differences for L-band, in correspondence with previous reported results for very young ice. Furthermore, it has the highest observed C-band copolar ratios. Ice 1-2 days old (Ice1) is characteristic for the large variability of the significantly negative P-band phases. Ice 0-3 days old (ice6, ice1 and ice5) has the highest C-band copolar ratios. Using copolar ratios and phases to discriminate ice of age 9-14

days (ice2) and older than 15 days (ice3) seem hard, but using L-band backscatter appears to give more contrast. It is possible that ice older than 15 days has slightly larger L and P-band phases than 9-14 days old ice. The large variability of L-band copolar ratio and phases is predicted by theory if the age is not accurately known.

Most of the phases for thin ice either has an offset relative zero degrees or has much larger variability or both compared to multi-year ice. Due to the large variability, it seems hard to discriminate thin ice types when only phase information is used, even though some ice types show some characteristic response.

We showed that the L-band backscatter tend to increase with the age of ice. This behavior is not observed for C-band; younger ice is observed to give higher backscatter than older thin ice, which is likely due to the development of frost flowers. However, the variations of L-band backscatter are rather high and there is pretty much mixing between classes if only one polarization and all pixels over all incidence angles are considered. Severe mixing between classes also occurs for combinations of different L-band channels. The best separations are found mainly by using C-band channels and for combinations with different polarizations. CHV combined with CHH/CVV but also CHV combined with LHH have been determined as giving the largest separation causing less misclassification, using a discriminate classifier. Ice less than one day old and multi-year ice are the ice types that separate best from the other types while the other ice types more or less overlap for most combinations. The calculated overall accuracy of each combination could be misleading, since it depends on the number of samples of each ice type. In the future, methods to determine normalized accuracies, independent of the number of samples of each class, must be considered.

The reason that C-band is the frequency most useful for separation of thin ice types might simply be because the sample data were selected mainly by using C-band HH channel. This means that there is more variability in the other band. This would have been avoided if data had been picked from a composite image including C, L and P-band and the phases for all bands. The conclusion is that the ice data of the C-band should be reliable whereas more consideration is needed for the results of the other bands.

10 Future work

In future work with this AIRSAR data set from the Beaufort Sea in 2004, more time must be spent on trying to understand what causes the large difference in absolute backscatter (LHH, LVV, LHV) of L-band between what has been observed in this study and in previous analyses. If the data was not correctly calibrated, this needs to be resolved. The CVV banding effect should be corrected for by designing a program for resolving this problem. More work is also needed to assess the quality of P-band and whether it is reasonable to get HH>VV over multi-year ice. In addition to the polarimetric parameters in this report, it would be interesting to include the correlation coefficients and the crosspolarized ratio (HV/HH), and investigate whether the separation between the ice types would be improved using any of these parameters. It also should be possible to include samples of incidence angles up to 60-65 degrees of ice older than a couple of days. New ice that is one day or younger may have signatures that are hidden by the system noise floor.

Another important issue is how to define different ice types and how to pick them. Instead of using only one or two channels of the same frequency band it would be better to pick samples from a composite image where the channels have the same importance. This would make it easier to detect and avoid deformations and inhomogeneities in the ice, causing less spread of the samples of each particular ice type. Only picking samples using C-band, disregarding the other bands include a lot of variability of the samples in L- and P-band, due to the sensitivity of ridging at these bands. Ice that is assumed to be 9-14 days old has a lot of variability, especially at C-band, and it is not sure that all samples of this ice type are of this age. Instead of assigning all samples to one group it might be better to divide this group into several others, such as level ice, deformed ice and ice which has developed frost flowers. It could also be a good idea to divide first-year and multi-year ice in level and deformed groups. Further studies might want to include samples of other ice types than thin ice, such as first-year ice, as well as analyze the signatures of deformed ice. In addition to the polarimetric data, acquisition of interferometric and infrared (IR) data was performed. It may be possible to obtain ice surface heights from interferometric data, which may be useful for future development of ridge detection models. Calibrated C, L and P-band would be needed for these investigations. Infrared radiation may be useful for detection of thin ice due to its large heat transfer from ocean to atmosphere compared to thick old ice. However, it is left as future work to investigate the separation between different thin ice types using this data. Another interesting thing would be to compare the AIRSAR and RADARSAT imagery and see if we miss any thin ice types in the RADARSAT images, due to its higher noise level. Do we miss only the thinnest ice, or is it more serious?

More work is needed to understand the nature of phase signatures of lead ice. The phases in this study have pretty large error bars which make the results hard to assess. If the phase images instead of backscatter images (CHH) had been used to define ice types, obviously the phases of the ice types would have had less variance. Large regions with very low and well-defined C-band phases are found in ice 11-12 days old in scene 6830, which could be an interesting thing to investigate and report in future work. Generally, the potential of copolar phases as an indicator of sea-ice thickness needs to be further investigated. Due to lack of in-situ data from this campaign it is impossible to relate the signatures to the

actual thickness. Future campaigns including in-situ measurements of this parameter are needed in order to investigate whether there is a connection between ice signatures and thickness.

Much improvement could be done regarding classification. Probably the accuracies could be increased by classifying the ice type pixels in ranges of different incidence angles where it is noted that the incidence angles do not change significantly. Normalization methods should be applied in order to be independent of groups of different number of pixels, for instance Kappa discrete multivariate techniques. It would also be interesting to evaluate other methods such as the unsupervised Wishart classifier.

11 References

Beaven, Scott Gerard. 1995. *Sea Ice Radar Backscatter Modeling, Measurements and the Fusion of Active and Passive Microwave Data.* 1995. pp. 75-83.

Carsey, Frank D., Barry, Roger G. and Weeks, Wilford F. 1992. Introduction. [book auth.] Frank D. Carsey. *Microwave Remote Sensing of Sea Ice.* Washington DC : American Geophysical Union, 1992, pp. 1-2.

Congalton, Russell G. 1991. *A Review of Assessing the Accuracy of Classification of Remotely Sensed Data.* s.l. : Remote Sens. Environ., 1991.

Curlander, J. C. and McDonough, R. N. 1991. *Synthetic Aperture Radar: Systems and Signal Processing.* New york : John Wiley & Sons, Inc, 1991.

Dierking, Wolfgang and Busche, Thomas. 2006. *Sea Ice Monitoring by L-band SAR: An Assessment Based on Literature and Comparisons of JERS-1 and ERS-1 Imagery.* s.l. : IEEE Transactions on Geoscience and Remote Sensing, 2006. pp. 957-970. Vols. 44, No. 2.

Drinkwater, Mark R. and Kwok, R. 1991. *Multifrequency Polarimetric Synthetic Aperture Radar Observations of Sea-Ice.* s.l. : Journal of Geophysical Research, 1991. pp. 20,679-20,698. Vol. 96.

Eriksson, Leif. 1998. *Analysis of SIR-C Dual-frequency Polarimetric Radar Signatures of Sea-Ice in the Weddell Sea.* Radio and Space Science, Chalmers University of Technology. Gothenburg : s.n., 1998.

ESA. 2007. ESA News. *European Space Agency.* [Online] ESA, September 14, 2007. http://www.esa.int/esaCP/SEMYTC13J6F_index_0.html.

Freeman, A., et al. 1991. *Calibration of NASA/JPL DC-8 SAR Data.* 1991.

Freeman, Anthony, Shen, Yuhsyen and Werner, Charles L. 1990. *Polarimetric SAR Calibration Experiment Using Active Radar Calibrators.* s.l. : IEEE Transactions on Geoscience and Remote Sensing, 1990. Vol. 28.

Grenfell, T. C., et al. 1992. Consideration for microwave remote sensing of thin sea ice. [ed.] F. Carsey. *Microwave Remote Sensing of sea ice.* Washington : American Geophysical Union, 1992, 14, pp. 291-301.

Henderson, Floyd M. 1998. *Principles & Applications of Imaging Radar.* 3. s.l. : John Wiley & Sons, Inc, 1998. Vol. 2.

Imel, David A. 2002. *What's Wrong With My AIRSAR Data?* s.l. : AIRSAR Earth Science and Applications Workshop 4-6 March 2002, 2002. pp. 4-6. Available at: airsar.jpl.nasa.gov/documents/workshop2002/papers/Q4.pdf.

Kwok, R., et al. 1995. *Retrieval of thin ice thickness from multifrequency polarimetric SAR data.* s.l. : Remote Sens. Environ., 1995. pp. 361-374. Vol. 51.

Kwok, Ronald and Cunningham, Glenn F. 1994. *Backscatter characteristics of the winter ice cover in the Beaufort Sea.* s.l. : Journal of Geophysical Research, 1994. pp. 7787-7802. Vol. 99.

Kwok, Ronald, et al. 1998. *Laboratory Measurements of Sea Ice: Connections to Microwave Remote Sensing.* s.l. : IEEE Transactions on Geoscience and Remote Sensing, 1998. Vol. 36.

Lou, Y. 2002. *How Accurate Are My AIRSAR Data.* [Presented at the AIRSAR Earth Science and Applications Workshop] Pasadena, USA : s.n., 2002.

Lou, Yunling. 2001. *CV Antenna Path Anomaly during the PacRim 2000 Flight Season.* s.l. : Interoffice Memorandum (334C-01-21), 2001.

Maykut, G. A. 1986. The surface heat and mass balance. [book auth.] Norbert Untersteiner. *The Geophysics of Sea Ice.* New York, NY : Plenum Press, 1986, pp. 422-423.

McCandless, Samuel W. and Jackson, Christopher R. 2004. Ch1. Principles of Synthetic Aperture Radar. [book auth.] C. R. Jackson and J.R. Apel. *Synthetic Aperture Radar Marine User's Manual.* Washington DC : s.n., 2004, pp. 12-21.

Nakamura, Kazuki, et al. 2005. *Observation of Sea-Ice Thickness in the Sea of Okhotsk by Using Dual-Frequency and Fully Polarimetric Airborne SAR (Pi-SAR) Data.* s.l. : IEEE Transactions on Geoscience and Remote Sensing, 2005. Vol. 43.

Nghiem, S. V. and Bertoia, C. 2001. *Study of Multi-Polarization C-band Backscatter Signatures for Arctic Sea Ice Mapping with Future Satellite SAR.* s.l. : Canadian Journal of Remote Sensing, 2001.

Nghiem, S. V., et al. 1995. *Polarimetric Signatures of Sea Ice; 2. Experimental Observations.* s.l. : Journal of Geophysical Research, 1995. Vols. 100, No. C7.

Onstott, Robert G. and Shuchman, A. Robert. 2004. Ch3. SAR Measurements of Sea Ice. [book auth.] Christoffer R. Jackson and John R. Apel. *Synthetic Aperture Radar Marine User's Manual.* Washington DC : s.n., 2004, pp. 84-89.

Onstott, Robert G. 1992. SAR and Scatterometer Signatures of Sea Ice. [book auth.] Frank D. Carsey. *Microwave Remote Sensing of Sea Ice.* Washington DC : s.n., 1992.

Pottier, E., Ferro-Famil, L. and Lopez, C. 2006. *PolSARpro Tutorial on Polarimetry and Interferometry.* 2006. Freely available at http://earth.esa.int/polsarpro/.

Raney, R. Keith, Luscombe, Anthony P. and Ahmed, Shabeer. 1991. RADARSAT. *Proceedings of the IEEE.* 1991, Vol. 79, 6, pp. 839-849.

Rignot, Eric and Drinkwater, Mark R. 1994. *Winter sea-ice mapping from multi-parameter synthetic-aperture radar data.* s.l. : Jornal of Glaciology, 1994. Vols. 40, No. 134.

Rigor, I., Colony, R. and Martin, S. 2000. *Variations in Surface Air Temperature Observations in the Arctic 1979-1997.* s.l. : Journal of Climate, 2000. pp. 896-914. Vol. 13.

Smith, Chris and Brown, Nicki. 1997. *ERDAS Field Guide.* Atlanta, Georgia : ERDAS Inc., 1997.

Stroeve, Julienne, et al. 2007. *Arctic sea ice decline: Faster than forecase.* s.l. : Geophysical Research Letters, 2007.

Ulaby, Fawwaz T., Moore, Rickard K. and Fung, Adrian K. 1986. *Microwave Remote Sensing: Active and Passive.* Dedham : Artech House Inc, 1986. pp. 1738-1741. Vol. III.

van Zyl, J. J. 1991. *AIRSAR Reference Manual.* [Available at: airsar.jpl.nasa.gov/documents/instrument.htm] 1991.

Winebrenner, D. P., Farmer, L. D. and Joughin, I. R. 1995. *On the response of polarimetric synthetic aperture radar signatures at 24-cm wavelength to sea ice thickness in Arctic leads.* s.l. : Radio Science, 1995. pp. 373-402. Vol. 30.

Winebrenner, Dale P., et al. 1989. *Sea-Ice Characterization Measurements Needed for Testing of Microwave Remote Sensing Models.* s.l. : Journal of Oceanic Engineering, 1989. pp. 149-158. Vols. 14, No. 2.

Woodhouse, Iain H. 2006. *Introduction to Microwave Remote Sensing.* Boca Raton, FL : CRC Press, 2006. 0-415-27123-1.

Appendix A **Ice terms**

Extract from the WMO Sea-Ice Nomenclature

PART II

ICE TERMS ARRANGED IN ALPHABETICAL ORDER

Aged ridge: *Ridge* which has undergone considerable weathering. These ridges are best described as undulations (8.2.2.4).

Anchor ice: Submerged ice attached or anchored to the bottom, irrespective of the nature of its formation (3.3).

Bare ice: Ice without snow cover (8.5).

Belt: A large feature of *pack ice* arrangement; longer than it is wide; from 1 km to more than 100 km in width (4.4.3).

Bergy bit: A large piece of floating *glacier ice*, generally showing less than 5 m above sea-level but more than 1 m and normally about 100–300 sq. m in area (10.4.4).

Beset: Situation of a vessel surrounded by ice and unable to move (12.1).

Big floe: (4.3.2.3) (see *Floe*).

Bight: An extensive crescent-shaped indentation in the *ice edge*, formed by either wind or current (4.4.6).

Brash ice: Accumulations of *floating ice* made up of fragments not more than 2 m across, the wreckage of other forms of ice (4.3.6).

Bummock: From the point of view of the submariner, a downward projection from the underside of the *ice canopy*; the counterpart of a *hummock* (13.4).

Calving: The breaking away of a mass of ice from an *ice wall*, *ice front* or *iceberg* (10.4.1).

Close pack ice: *Pack ice* in which the *concentration* is 7/10 to 8/10 (6/8 to less than 7/8), composed of *floes* mostly in contact (4.2.3).

Compacted ice edge: Close, clear-cut *ice edge* compacted by wind or current; usually on the windward side of an area of *pack ice* (4.4.8.1).

Compacting: Pieces of *floating ice* are said to be compacting when they are subjected to a converging motion, which increases ice *concentration* and/or produces stresses which may result in ice deformation (5.2).

Compact pack ice: *Pack ice* in which the *concentration is* 10/10 (8/8) and no water is visible (4.2.1).

Concentration: The ratio in tenths of the sea surface actually covered by ice to the total area of sea surface, both ice-covered and *ice-free*, at a specific location or over a defined area (4.2).

Concentration boundary: A line approximating the transition between two areas of *pack ice* with distinctly different *concentrations* (4.4.9.2).

Consolidated pack ice: *Pack ice* in which the *concentration* is 10/10 (8/8) and the *floes* are frozen together (4.2.1.1).

Consolidated ridge: A *ridge* in which the base has frozen together (8.2.2.5).

Crack: Any *fracture* which has not parted (7.1.1).

Dark nilas: *Nilas* which is under 5 cm in thickness and is very dark in colour (2.2.1).

Deformed ice: A general term for ice which has been squeezed together and in places forced upwards (and downwards). Subdivisions are *rafted ice*, *ridged ice* and *hummocked ice* (8.2).

Difficult area: A general qualitative expression to indicate, in a relative manner, that the severity of ice conditions prevailing in an area is such that navigation in it is difficult (12.5).

Diffuse ice edge: Poorly defined *ice edge* limiting an area of dispersed ice; usually on the leeward side of an area of *pack ice* (4.4.8.2).

Diverging: *Ice fields* or *floes* in an area are subjected to diverging or dispersive motion, thus reducing ice *concentration* and/or relieving stresses in the ice (5.1).

Dried ice: *Sea ice* from the surface of which melt-water has disappeared after the formation of *cracks* and *thaw holes*. During the period of drying, the surface whitens (9.3).

Easy area: A general qualitative expression to indicate, in a relative manner, that ice conditions prevailing in an area are such that navigation in it is not difficult (12.6).

Fast ice: *Sea ice* which forms and remains fast along the coast, where it is attached to the shore, to an *ice wall*, to an *ice front*, between shoals or grounded *icebergs*. Vertical fluctuations may be observed during changes of sea-level. Fast ice may be formed *in situ* from sea water or by freezing of *pack ice* of any age to the shore, and it may extend a few metres or several hundred kilometres from the coast. Fast ice may be more than one year old and may then be prefixed with the appropriate age category (*old*, *second-year*, or *multi-year*). If it is thicker than about 2 m above sea-level it is called an *ice shelf* (3.1).

Fast-ice boundary: The *ice boundary* at any given time between *fast ice* and *pack ice* (4.4.9.1).

Fast-ice edge: The demarcation at any given time between *fast ice* and *open water* (4.4.8.5).

Finger rafted ice: Type of *rafted ice* in which *floes* thrust "fingers" alternately over and under the other (8.2.1.1).

Finger rafting: Type of rafting whereby interlocking thrusts are formed, each floe thrusting "fingers" alternately over and under the other. Common in *nilas* and *grey ice* (6.4.1).

Firn: Old snow which has recrystallized into a dense material. Unlike snow, the particles are to some extent joined together; but, unlike ice, the air spaces in it still connect with each other (10.1).

First-year ice: *Sea ice* of not more than one winter's growth, developing from *young ice*; thickness 30 cm – 2 m. May be subdivided into *thin first-year ice* / white ice, *medium first-year ice* and *thick first-year ice* (2.5).

Flaw: A narrow separation zone between *pack ice* and *fast ice*, where the pieces of ice are in chaotic state; it forms when pack ice shears under the effect of a strong wind or current along the *fast ice boundary* (7.1.1.2) (cf. *shearing*).

Flaw lead: A passage-way between *pack-ice* and *fast ice* which is navigable by surface vessels (7.3.2).

Flaw polynya: A *polynya* between *pack ice* and *fast ice* (7.4.2)

Floating ice: Any form of ice found floating in water. The principal kinds of floating ice are *lake ice*, *river ice*, and *sea ice*, which form by the freezing of water at the surface, and *glacier ice (ice of land origin)* formed on land or in an *ice shelf*. The concept includes ice that is stranded or grounded (1.).

Floe: Any relatively flat piece of *sea ice* 20 m or more across. Floes are subdivided according to horizontal extent as follows (4.3.2):

GIANT: Over 10 km across (4.3.2.1).
VAST: 2–10 km across (4.3.2.2).
BIG: 500–2,000 m across (4.3.2.3).
MEDIUM: 100–500 m across (4.3.2.4).
SMALL: 20–100 m across (4.3.2.5).

Floeberg: A massive piece of *sea ice* composed of a *hummock*, or a group of *hummocks*, frozen together and separated from any ice surroundings. It may float up to 5 m above sea-level (4.3.4).

Flooded ice: *Sea ice* which has been flooded by melt-water or river water and is heavily loaded by water and wet snow (9.5).

Fracture: Any break or rupture through *very close pack ice*, *compact pack ice*, *consolidated pack-ice*, *fast ice*, or a single *floe* resulting from deformation processes. Fractures may contain *brash ice* and/or be covered with *nilas* and/or *young ice*. Length may vary from a few metres to many kilometres (7.1).

Fracture zone: An area which has a great number of fractures (7.2).

Fracturing: Pressure process whereby ice is permanently deformed, and rupture occurs. Most commonly used to describe breaking across *very close pack ice*, *compact pack ice* and *consolidated pack ice* (6.1).

Frazil ice: Fine spicules or plates of ice, suspended in water (2.1.1).

Friendly ice: From the point of view of the submariner, an *ice canopy* containing many large *skylights* or other features which permit a submarine to surface. There must be more than ten such features per 30 nautical miles (56 km) along the submarine's track (13.2).

Frost smoke: Fog-like clouds due to contact of cold air with relatively warm water, which can appear over openings in the ice, or leeward of the *ice edge*, and which may persist while ice is forming (11.3).

Giant floe: (4.3.2.1) (see *Floe*).

Glacier: A mass of snow and ice continuously moving from higher to lower ground or, if afloat, continuously spreading. The principal forms of glacier are: inland ice sheets, *ice shelves*, *ice streams*, ice caps, ice piedmonts, cirque glaciers and various types of mountain (valley) glaciers (10.2.1).

Glacier berg: An irregularly shaped *iceberg* (10.4.2.1).

Glacier ice: Ice in, or originating from, a *glacier*, whether on land or floating on the sea as *icebergs*, *bergy bits* or *growlers* (10.2).

Glacier tongue: Projecting seaward extension of a *glacier*, usually afloat. In the Antarctic glacier tongues may extend over many tens of kilometres (10.2.4).

Grease ice: A later stage of freezing than *frazil ice* when the crystals have coagulated to form a soupy layer on the surface. Grease ice reflects little light, giving the sea a matt appearance (2.1.2).

Grey ice: *Young ice* 10–15 cm thick. Less elastic than *nilas* and breaks on swell. Usually rafts under pressure (2.4.1).

Grey-white ice: *Young ice* 15-30 cm thick. Under pressure more likely to ridge than to raft (2.4.2).

Grounded hummock: Hummocked *grounded ice* formation. There are single grounded *hummocks* and lines (or chains) of grounded *hummocks* (3.4.2).

Grounded ice: *Floating ice* which is aground in shoal water (3.4) (cf. stranded ice).

Growler: Smaller piece of ice than a *bergy bit* or *floeberg*, often transparent but appearing green or almost black in colour, extending less than 1 m above the sea surface and normally occupying an area of about 20 sq. m (10.4.5).

Hostile ice: From the point of view of the submariner, an *ice canopy* containing no large *skylights* or other features which permit a submarine to surface (13.3).

Hummock: A hillock of broken ice which has been forced upwards by pressure. May be fresh or weathered. The submerged volume of broken ice under the hummock, forced downwards by pressure, is termed a *bummock* (8.2.3).

Hummocked ice: *Sea ice* piled haphazardly one piece over another to form an uneven surface. When weathered, has the appearance of smooth hillocks (8.2.3.1).

Hummocking: The pressure process by which *sea ice* is forced into *hummocks*. When the floes rotate in the process it is termed screwing (6.2).

Iceberg: A massive piece of ice of greatly varying shape, more than 5 m above sea-level, which has broken away from a *glacier*, and which may be afloat or aground. Icebergs may be described as *tabular*, dome-shaped, sloping, pinnacled, weathered or *glacier bergs* (10.4.2).

Iceberg tongue: A major accumulation of *icebergs* projecting from the coast, held in place by grounding and joined together by *fast ice* (10.4.2.3).

Ice blink: A whitish glare on low clouds above an accumulation of distant ice (11.2).

Ice-bound: A harbour, inlet, etc., is said to be ice-bound when navigation by ships is prevented on account of ice, except possibly with the assistance of an icebreaker (12.2).

Ice boundary: The demarcation at any given time between *fast ice* and *pack ice* or between areas of *pack ice* of different *concentrations* (4.4.9) (cf. ice edge).

Ice breccia: Ice pieces of different age frozen together (4.3.5).

Ice cake: Any relatively flat piece of *sea ice* less than 20 m across (4.3.3).

Ice canopy: *Pack ice* from the point of view of the submariner (13.1).

Ice cover: The ratio of an area of ice of any concentration to the total area of sea surface within some large geographic local; this local may be global, hemispheric, or prescribed by a specific oceanographic entity such as Baffin Bay or the Barents Sea (4.1).

Ice edge: The demarcation at any given time between the open sea and *sea ice* of any kind, whether fast or drifting. It may be termed *compacted* or *diffuse* (4.4.8) (cf. *ice boundary*).

Ice field: Area of *pack ice* consisting of any size of *floes*, which is greater than 10 km across (4.4.1) (cf. *patch*).

Icefoot: A narrow fringe of ice attached to the coast, unmoved by tides and remaining after the *fast ice* has moved away (3.2).

Ice-free: No *sea ice* present. There may be some *ice of land origin* (4.2.7) (cf. *open water*).

Ice front: The vertical cliff forming the seaward face of an *ice shelf* or other floating *glacier* varying in height from 2–50 m or more above sea-level (10.3.1) (cf. *ice wall*).

Ice island: A large piece of floating ice about 5 m above sea-level, which has broken away from an Arctic ice shelf, having a thickness of 30–50 m and an area of from a few thousand square metres to 500 sq km. or more, and usually characterized by a regularly undulating surface which gives it a ribbed appearance from the air (10.4.3).

Ice jam: An accumulation of broken *river ice* or *sea ice* caught in a narrow channel (4.4.7).

Ice keel: From the point of view of the submariner, a downward-projecting ridge on the underside of the *ice canopy*; the counterpart of a ridge. Ice keels may extend as much as 50 m below sea-level (13.5).

Ice limit: Climatological term referring to the extreme minimum or extreme maximum extent of the *ice edge* in any given month or period based on observations over a number of years. Term should be preceded by minimum or maximum (4.4.8.3) (cf. *mean ice edge*).

Ice massif: A concentration of *sea ice* covering hundreds of square kilometres, which is found in the same region every summer (4.4.2).

Ice of land origin: Ice formed on land or in an *ice shelf*, found floating in water. The concept includes ice that is stranded or grounded (1.2).

Ice patch: An area of *pack ice* less than 10 km across (4.4.1.4).

Ice port: An embayment in an *ice front*, often of a temporary nature, where ships can moor alongside and unload directly onto the ice shelf (12.7).

Ice rind: A brittle shiny crust of ice formed on a quiet surface by direct freezing or from *grease ice*, usually in water of low salinity. Thickness to about 5 cm. Easily broken by wind or swell, commonly breaking in rectangular pieces (2.2.3).

Ice shelf: A floating ice sheet of considerable thickness showing 2–50 m or more above sea-level, attached to the coast. Usually of great horizontal extent and with a level or gently undulating surface. Nourished by annual snow accumulation and often also by the seaward extension of land *glaciers*. Limited areas may be aground. The seaward edge is termed an *ice front* (q.v.) (10.3).

Ice stream: Part of an inland ice sheet in which the ice flows more rapidly and not necessarily in the same direction as the surrounding ice. The margins are sometimes clearly marked by a change in direction of the surface slope but may be indistinct (10.2.3).

Ice under pressure: Ice in which deformation processes are actively occurring and hence a potential impediment or danger to shipping (12.4).

Ice wall: An ice cliff forming the seaward margin of a *glacier* which is not afloat. An ice wall is aground, the rock basement being at or below sea-level (10.2.2) (cf. *ice front*).

Lake ice: Ice formed on a lake, regardless of observed location (1.3).

Large fracture: More than 500 m wide (7.1.5).

Large ice field: An *ice field* over 20 km across (4.4.1.1).

Lead: Any *fracture* or passage-way through *sea ice* which is navigable by surface vessels (7.3).

Level ice: *Sea ice* which is unaffected by deformation (8.1)

Light nilas: *Nilas* which is more than 5 cm in thickness and rather lighter in colour than *dark nilas* (2.2.2).

Mean ice edge: Average position of the *ice edge* in any given month or period based on observations over a number of years. Other terms which may be used are mean maximum ice edge and mean minimum ice edge (4.4.8.4) (cf. *ice limit*).

Medium first-year ice: *First-year ice* 70–120 cm thick (2.5.2).

Medium floe: (see *Floe*) (4.3.2.4).

Medium fracture: 200 to 500 m wide (7.1.4).

Medium ice field: An *ice field* 15–20 km across (4.4.1.2).

Multi-year ice: *Old ice* up to 3 m or more thick which has survived at least two summers' melt. *Hummocks* even smoother than in *second-year ice*, and the ice is almost salt-free. Colour, where bare, is usually blue. Melt pattern consists of large interconnecting irregular *puddles* and a well-developed drainage system (2.6.2).

New ice: A general term for recently formed ice which includes *frazil ice*, *grease ice*, *slush* and *shuga*. These types of ice are composed of ice crystals which are only weakly frozen together (if at all) and have a definite form only while they are afloat (2.1).

New ridge: *Ridge* newly formed with sharp peaks and slope of sides usually 40°. Fragments are visible from the air at low altitude (8.2.2.1).

Nilas: A thin elastic crust of ice, easily bending on waves and swell and under pressure, thrusting in a pattern of interlocking "fingers" *(finger rafting)*. Has a matt surface and is up to 10 cm in thickness. May be subdivided into *dark nilas* and *light nilas* (2.2).

Nip: Ice is said to nip when it forcibly presses against a ship. A vessel so caught, though undamaged, is said to have been nipped (12.3).

Old ice: *Sea ice* which has survived at least one summer's melt. Most topographic features are smoother than on *first-year ice*. May be subdivided into *second-year ice* and *multi-year ice* (2.6).

Open pack ice: *Pack ice* in which the ice *concentration* is 4/10 to 6/10 (3/8 to less than 6/8), with many *leads* and *polynyas*, and the *floes* are generally not in contact with one another (4.2.4).

Open water: A large area of freely navigable water in which *sea ice* is present in *concentrations* less than 1/10 (1/8). When there is no sea ice present, the area should be termed *ice-free*, even though icebergs are present (4.2.6).

Pack ice: Term used in a wide sense to include any area of *sea ice*, other than *fast ice*, no matter what form it takes or how it is disposed (4.).

Pancake ice: Predominantly circular pieces of ice from 30 cm – 3 m in diameter, and up to about 10 cm in thickness, with raised rims due to the pieces striking against one another. It may be formed on a slight swell from *grease ice*, *shuga* or *slush* or as a result of the breaking of *ice rind*, *nilas* or, under severe conditions of swell or waves, of *grey ice*. It also sometimes forms at some depth, at an interface between water bodies of different physical characteristics, from where it floats to the surface; its appearance may rapidly cover wide areas of water (4.3.1).

Polynya: Any non-linear shaped opening enclosed in ice. Polynyas may contain *brash ice* and/or be covered with *new ice*, *nilas* or *young ice*; submariners refer to these as *skylights*. Sometimes the polynya is limited on one side by the coast and is called a *shore polynya* or by *fast ice* and is called a *flaw polynya*. If it recurs in the same position every year, it is called a *recurring polynya* (7.4).

Puddle: An accumulation on ice of melt-water, mainly due to melting snow, but in the more advanced stages also to the melting of ice. Initial stage consists of patches of melted snow (9.1).

Rafted ice: Type of *deformed ice* formed by one piece of ice overriding another (8.2.1) (cf. finger rafting).

Rafting: Pressure processes whereby one piece of ice overrides another. Most common in *new* and *young ice* (6.4) (cf. *finger rafting*).

Ram: An underwater ice projection from an *ice wall*, *ice front*, *iceberg* or *floe*. Its formation is usually due to a more intensive melting and erosion of the unsubmerged part (8.4).

Recurring polynya: A *polynya* which recurs in the same position every year (7.4.3).

Ridge: A line or wall of broken ice forced up by pressure. May be fresh or weathered. The submerged volume of broken ice under a ridge, forced downwards by pressure, is termed an *ice keel* (8.2.2).

Ridged ice: Ice piled haphazardly one piece over another in the form of ridges or walls. Usually found in first-year ice (8.2.2.6) (cf. *ridging*).

Ridged-ice zone: An area in which much *ridged ice* with similar characteristics has formed (8.2.2.6.1).

Ridging: The pressure process by which *sea ice* is forced into *ridges* (6.3).

River ice: Ice formed on a river, regardless of observed location (1.4).

Rotten ice: *Sea ice* which has become honeycombed and which is in an advanced state of disintegration (9.4).

Sastrugi: Sharp, irregular ridges formed on a snow surface by wind erosion and deposition. On mobile *floating ice* the ridges are parallel to the direction of the prevailing wind at the time they were formed (8.6.1).

Sea ice: Any form of ice found at sea which has originated from the freezing of sea water (1.1).

Second-year ice: *Old ice* which has survived only one summer's melt. Because it is thicker and less dense than *first-year ice*, it stands higher out of the water. In contrast to *multi-year ice*, summer melting produces a regular pattern of numerous small *puddles*. Bare patches and puddles are usually greenish-blue (2.6.1).

Shearing: An area of *pack ice* is subject to shear when the ice motion varies significantly in the direction normal to the motion, subjecting the ice to rotational forces. These forces may result in phenomena similar to a *flaw* (q.v.) (5.3).

Shore lead: A *lead* between *pack ice* and the shore or between *pack ice* and an *ice front* (7.3.1).

Shore polynya: A *polynya* between *pack ice* and the coast or between *pack ice* and an *ice front* (7.4.1).

Shuga: An accumulation of spongy white ice lumps, a few centimetres across; they are formed from *grease ice* or *slush* and sometimes from *anchor ice* rising to the surface (2.1.4).

Skylight: From the point of view of the submariner, thin places in the *ice canopy*, usually less than 1 m thick and appearing from below as relatively light, translucent patches in dark surroundings. The undersurface of a skylight is normally flat. Skylights are called large if big enough for a submarine to attempt to surface through them (120 m), or small if not (13.6).

Slush: Snow which is saturated and mixed with water on land or ice surfaces, or as a viscous floating mass in water after a heavy snowfall (2.1.3).

Small floe: (4.3.2.5) (see *Floe*).

Small fracture: 50 to 200 m wide (7.1.3).

Small ice cake: An ice cake less than 2 m across (4.3.3.1).

Small ice field: An *ice field* 10–15 km across (4.4.1.3).

Snow-covered ice: Ice covered with snow (8.6).

Snowdrift: An accumulation of wind-blown snow deposited in the lee of obstructions or heaped by wind eddies. A crescent-shaped snowdrift, with ends pointing down-wind, is known as a snow barchan (8.6.2).

Standing floe: A separate *floe* standing vertically or inclined and enclosed by rather smooth ice (8.3).

Stranded ice: Ice which has been floating and has been deposited on the shore by retreating high water (3.4.1).

Strip: Long narrow area of *pack ice*, about 1 km or less in width, usually composed of small fragments detached from the main mass of ice, and run together under the influence of wind, swell or current (4.4.5).

Tabular berg: A flat-topped *iceberg*. Most tabular bergs form by *calving* from an *ice shelf* and show horizontal banding (10.4.2.2) (cf. *ice island*).

Thaw holes: Vertical holes in *sea ice* formed when surface *puddles melt through to the underlying water* (9.2).

Thick first-year ice: *First-year ice* over 120 cm thick (2.5.3).

Thin first-year ice/white ice: *First year ice* 30–70 cm thick (2.5.1).

Tide crack: Crack at the line of junction between an immovable *ice foot* or *ice wall* and *fast ice*, the latter subject to rise and fall of the tide (7.1.1.1).

Tongue: A projection of the ice edge up to several kilometres in length, caused by wind or current (4.4.4).

Vast floe: (4.3.2.2) (see *Floe*).

Very close pack ice: *Pack ice* in which the *concentration* is 9/10 to less than 10/10 (7/8 to less than 8/8) (4.2.2).

Very open pack ice: *Pack ice* in which the *concentration* is 1/10 to 3/10 (1/8 to less than 3/8) and water preponderates over ice (4.2.5).

Very small fracture: 0 to 50 m wide (7.1.2).

Very weathered ridge: *Ridge* with tops very rounded, slope of sides usually 20°–30° (8.2.2.3).

Water sky: Dark streaks on the underside of low clouds, indicating the presence of water features in the vicinity of *sea ice* (11.1).

Weathered ridge: *Ridge* with peaks slightly rounded and slope of sides usually 30° to 40°. Individual fragments are not discernible (8.2.2.2).

Weathering: Processes of ablation and accumulation which gradually eliminate irregularities in an ice surface (6.5).

White ice: See *Thin first-year ice* (2.5.1).

Young coastal ice: The initial stage of *fast ice* formation consisting of *nilas or young ice*, its width varying from a few metres up to 100–200 m from the shoreline (3.1.1).

Young ice: Ice in the transition stage between *nilas* and *first-year ice*, 10–30 cm in thickness. May be subdivided into *grey ice* and *grey-white ice* (2.4).

Appendix B **AIRSAR Survey Image**

The approximate positions of the six processed AIRSAR scenes are indicated in the two survey images: SeaIce218-1 and SeaIce218-2. Survey images are acquired with LVV radar channel.

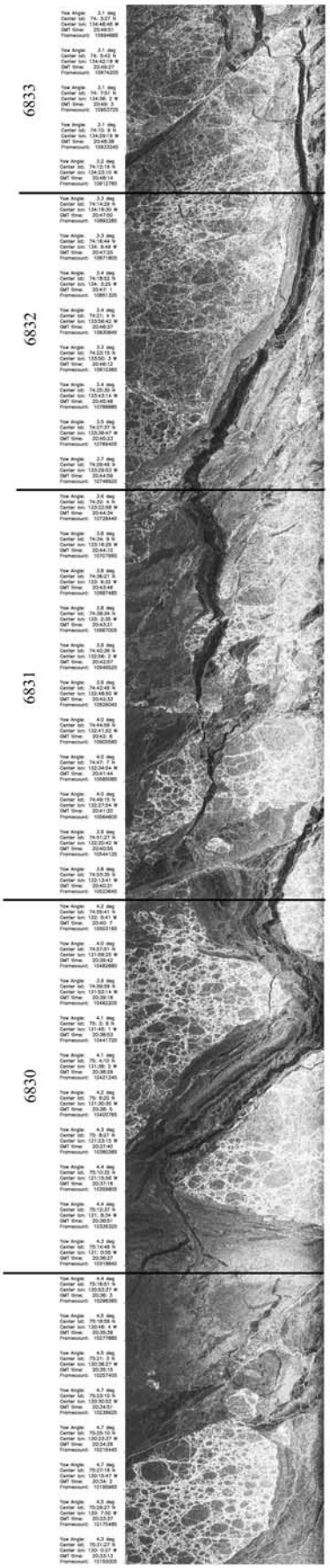
6833
6832
6831
6830

Run Name: Sealce218--1 Flight Date: 2004/12/2 HDDC ID: 04084
Radar Mode: POLSAR Chirp Bandwidth: 20 MHz Radar Altitude: 7812 M Swath Width: 20772 M Flight Direction
Radar Channel: Lvv
Illumination
60 40 20
6834

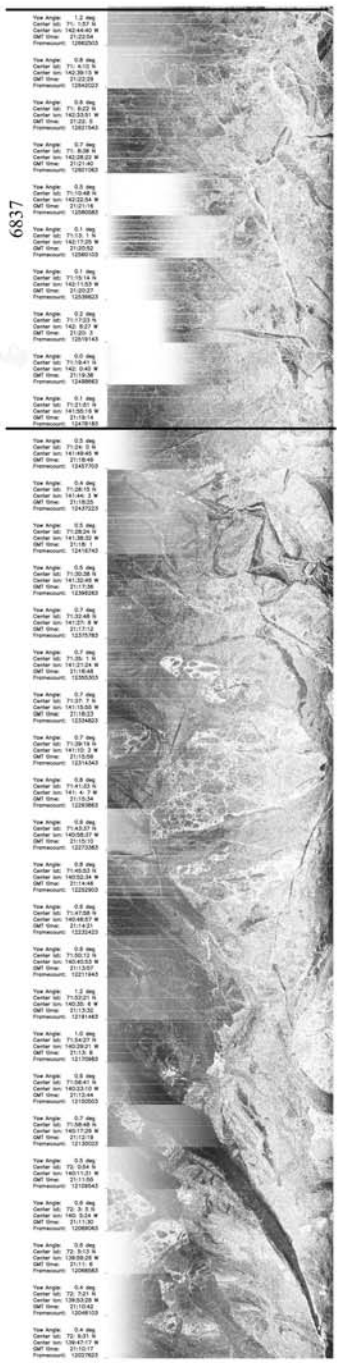
6837

Run Name: Sealce218--2 Flight Date: 2004/12/2 HDDC ID: 04085
Radar Mode: POLSAR Chirp Bandwidth: 20 MHz Radar Altitude: 7984 M Swath Width: 20920 M Flight Direction
Radar Channel: Lvv
Illumination
60 40 20

Appendix C **AIRSAR Scenes**

AIRSAR scenes: 6830, 6831, 6832, 6833, 6834 and 6837

INTEGRATED AIRSAR PROCESSOR (V. 6.37/)

SEAICE218-1

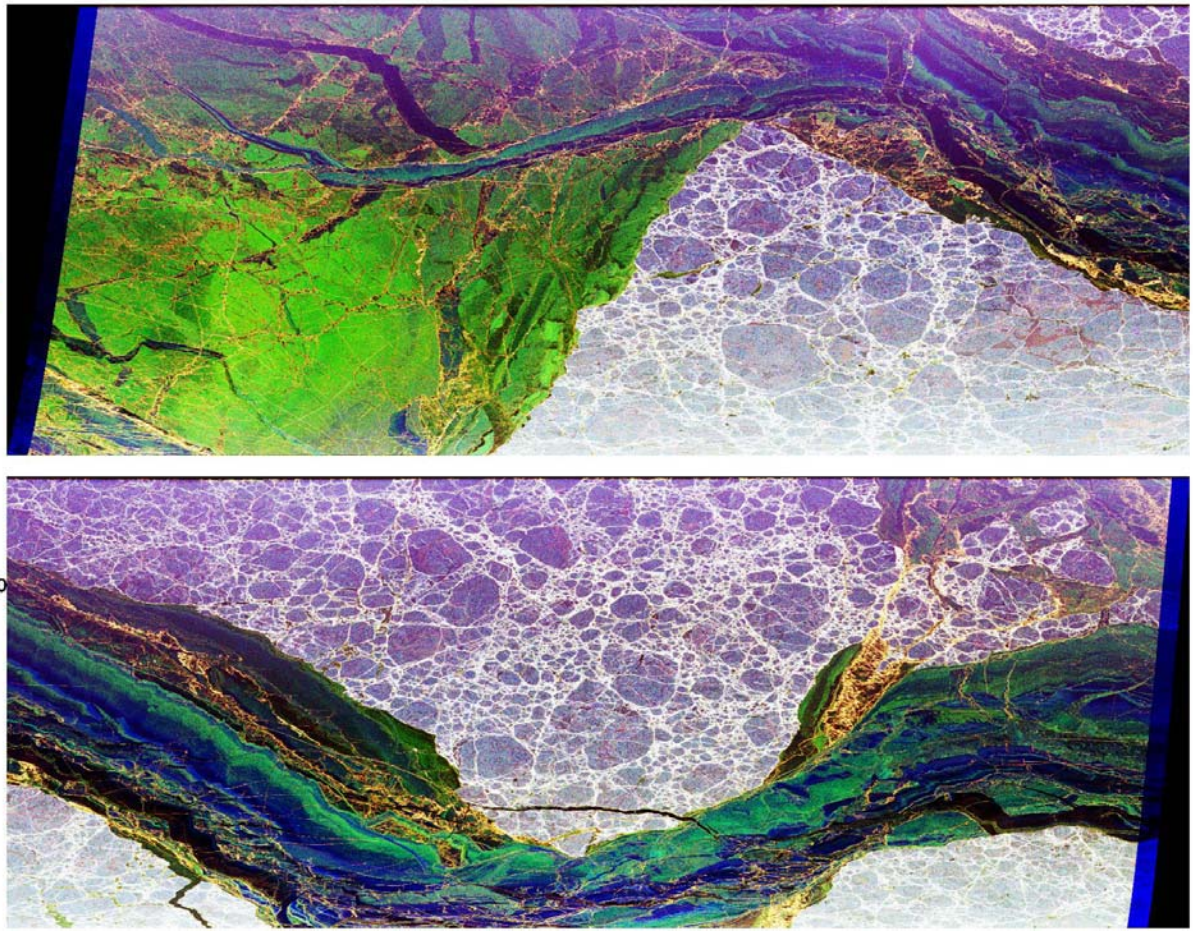

Radar Illumination

Velocity

P-Band Total Power
L-Band Total Power
C-Band Total Power

Date Acquired:
2-DEC-04
Date Processed:
26-FEB-07
CCTID: CM6830

Cntr lat: 75.10
Cntr lon: -131.63
Bandwidth: 20.00
Cross-track:
Slant Swath(km):17.0
samples in data: 2560
reduction ratio: 0.2
Along-track:
Swath(km):61.1
lines in data: 6611
reduction ratio: 0.5

NORTH

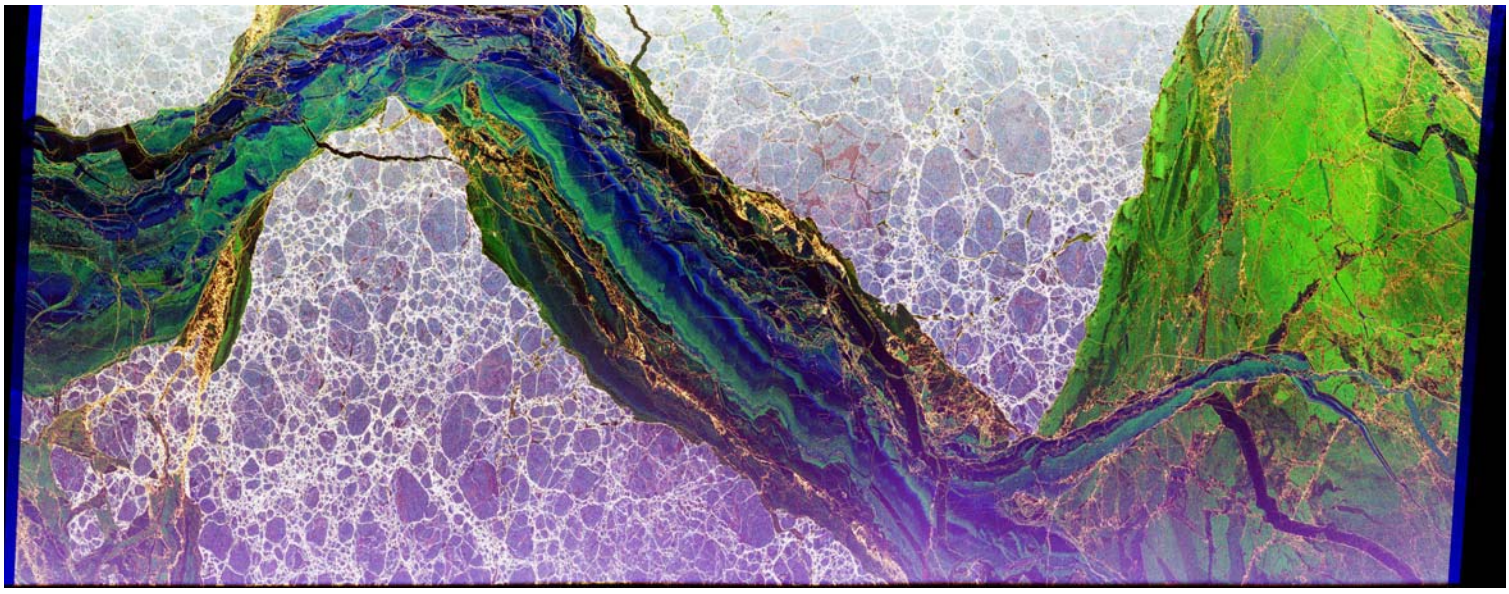

INTEGRATED AIRSAR PROCESSOR (V. 6.37/)

SEAICE218-1

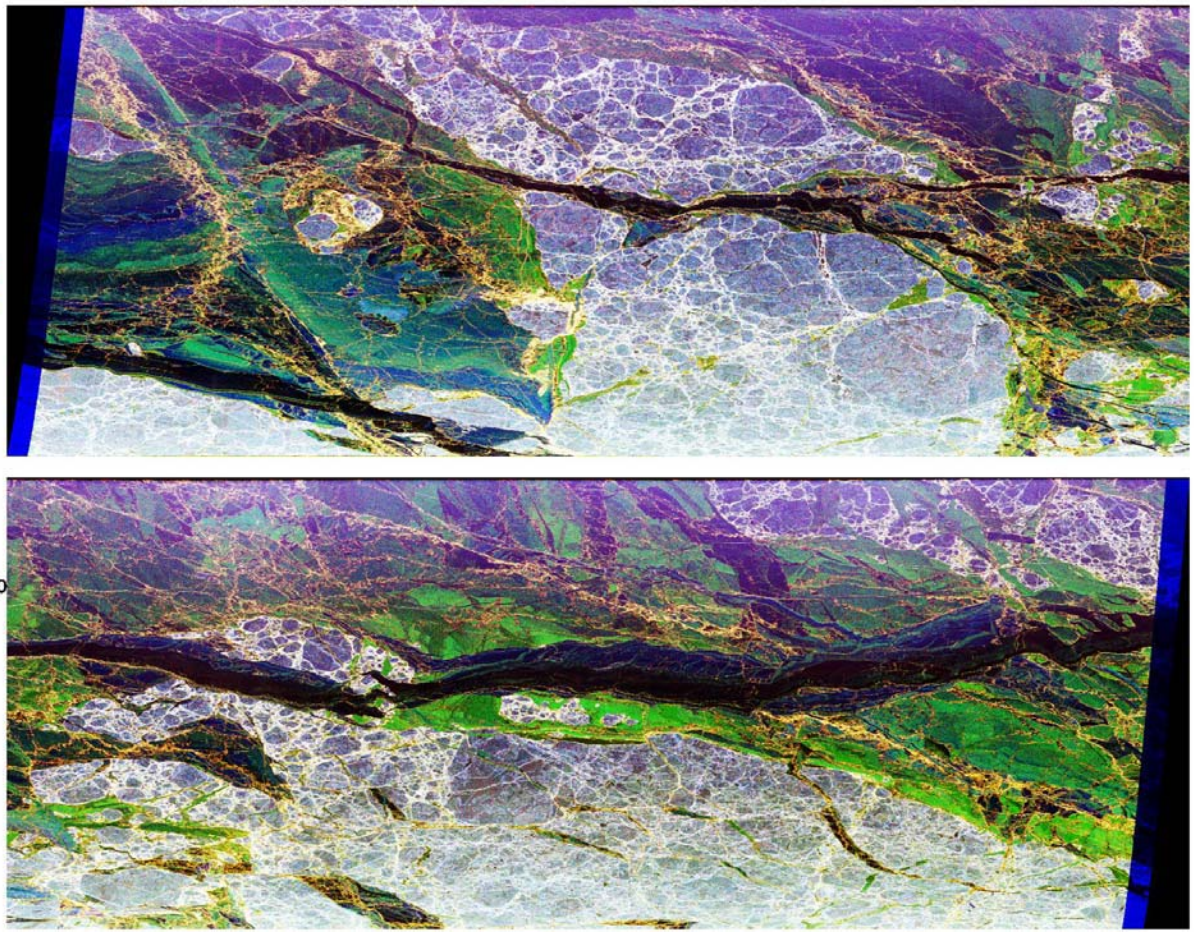

Radar Illumination

Velocity

P-Band Total Power
L-Band Total Power
C-Band Total Power

Date Acquired:
2-DEC-04
Date Processed:
26-FEB-07
CCTID: CM6831

Cntr lat: 74.70
Cntr lon: -132.94
Bandwidth: 20.00
Cross-track:
Slant Swath(km):17.0
samples in data: 2560
reduction ratio: 0.2
Along-track:
Swath(km):61.2
lines in data: 6626
reduction ratio: 0.5

NORTH

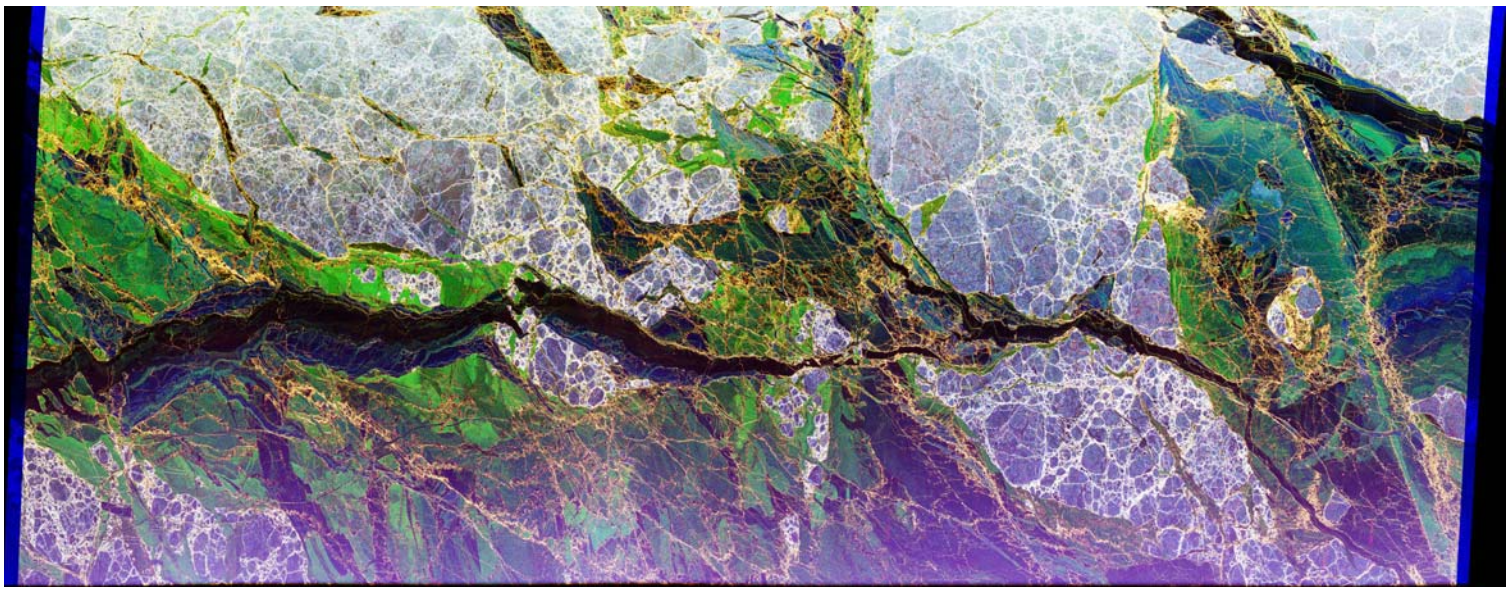

INTEGRATED AIRSAR PROCESSOR

{V. 6.38/2004A.BAAA}

SEAICE218-1

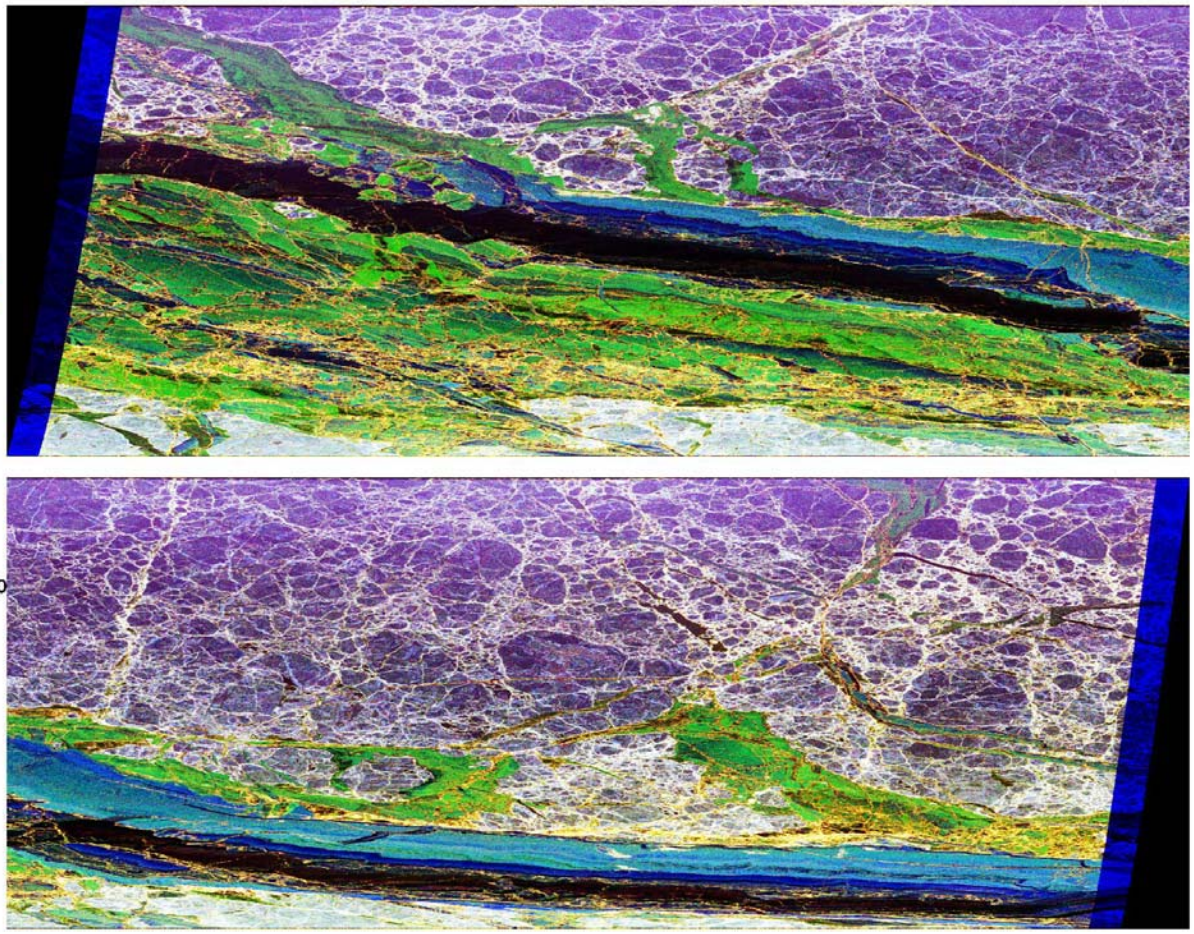

Radar Illumination

Velocity

P-Band Total Power
L-Band Total Power
C-Band Total Power

Date Acquired:
2-DEC-04
Date Processed:
26-FEB-07
CCTID: CM6832

Cntr lat: 74.37
Cntr lon: -133.99
Bandwidth: 20.00
Cross-track:
Slant Swath(km):17.0
samples in data: 2560
reduction ratio: 0.2
Along-track:
Swath(km):41.3
lines in data: 4466
reduction ratio: 0.7

NORTH

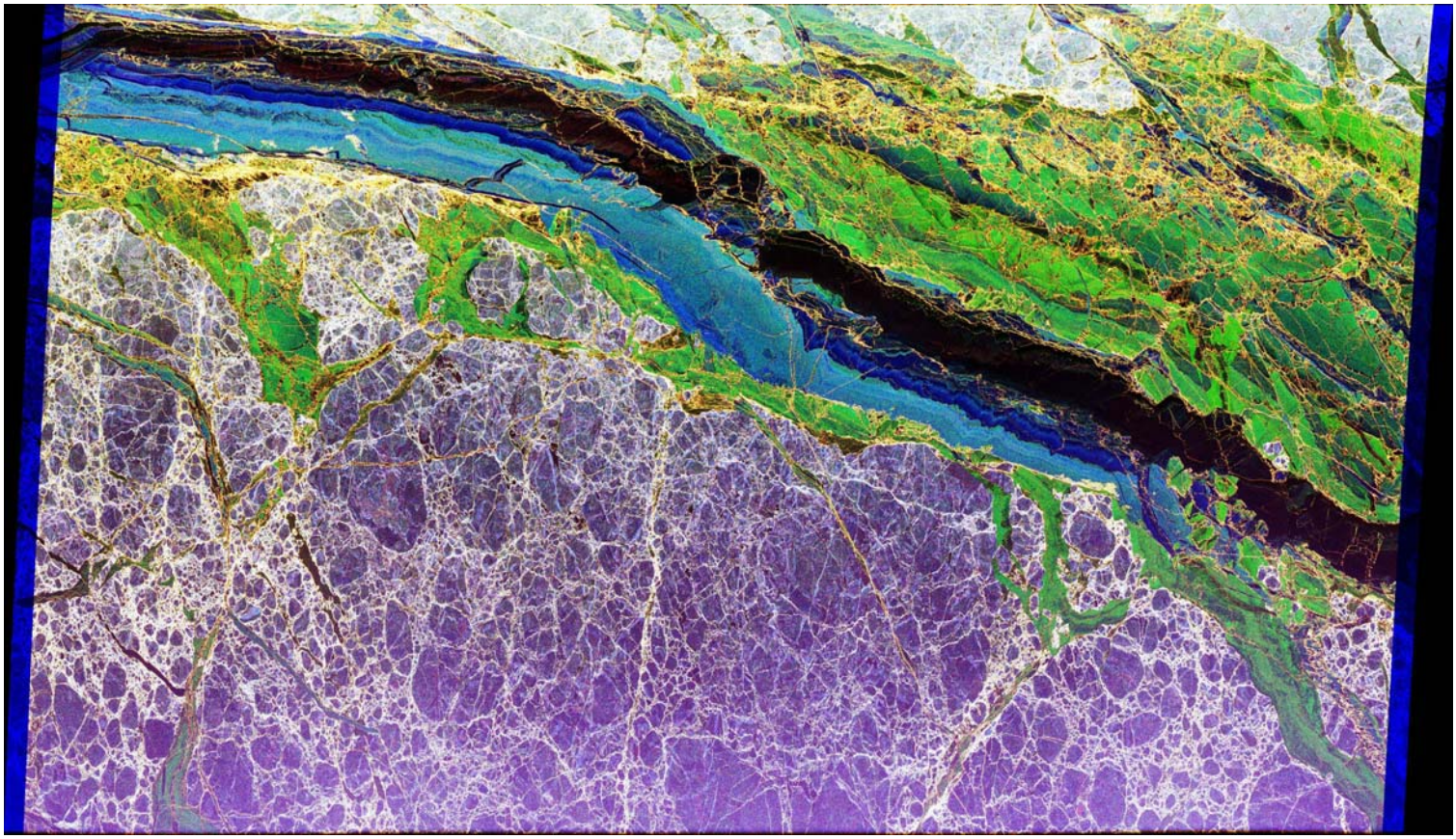

INTEGRATED AIRSAR PROCESSOR

{V. 6.38/2004A.BAAA}

SEAICE218-1

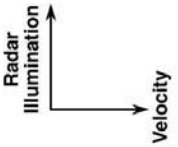

P-Band Total Power
L-Band Total Power
C-Band Total Power

Date Acquired:
2-DEC-04
Date Processed:
6-FEB-07
CCTID: CM6833

Cntr lat: 74.14
Cntr lon: -134.68
Bandwidth: 20.00
Cross-track:
Slant Swath(km):17.0
samples in data: 2560
reduction ratio: 0.2
Along-track:
Swath(km):30.7
lines in data: 3321
reduction ratio: 0.9

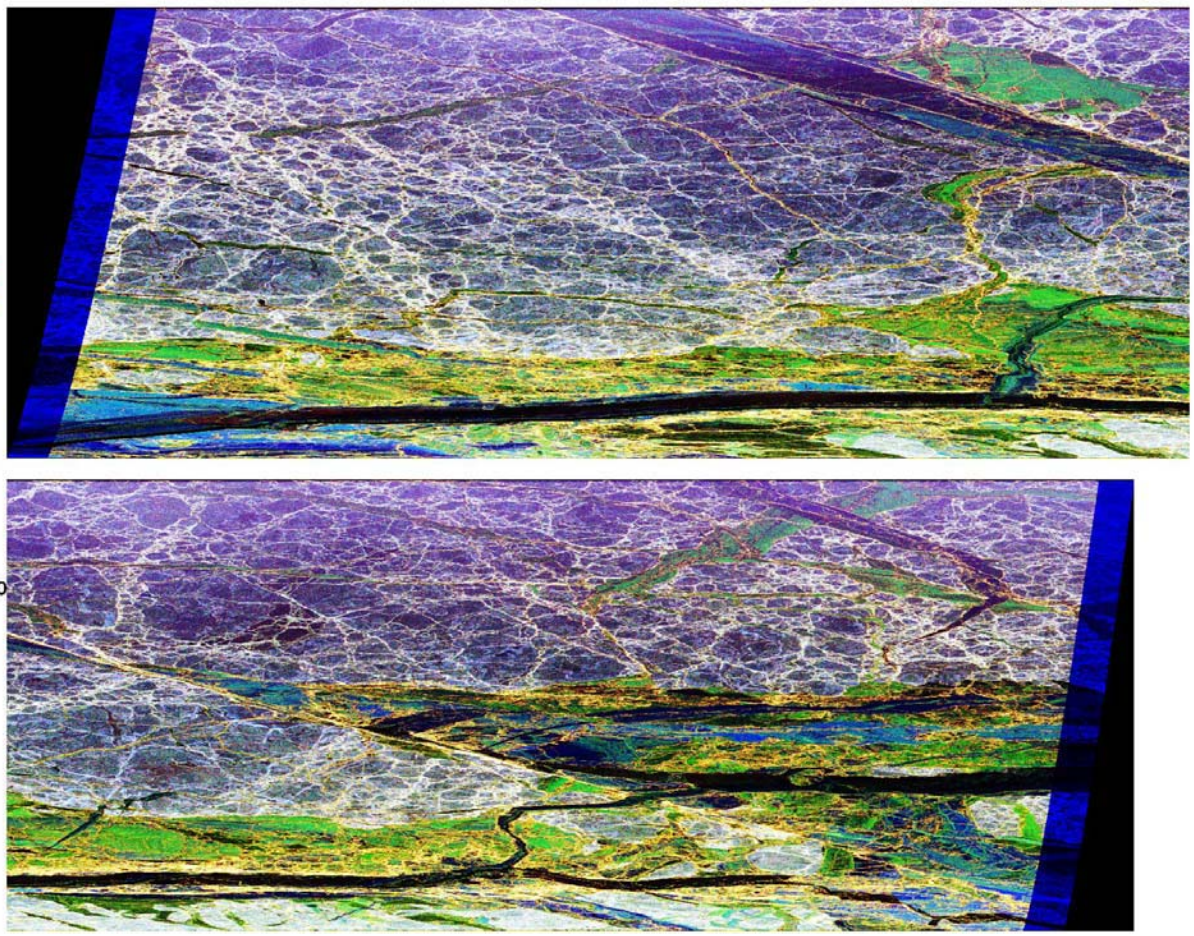

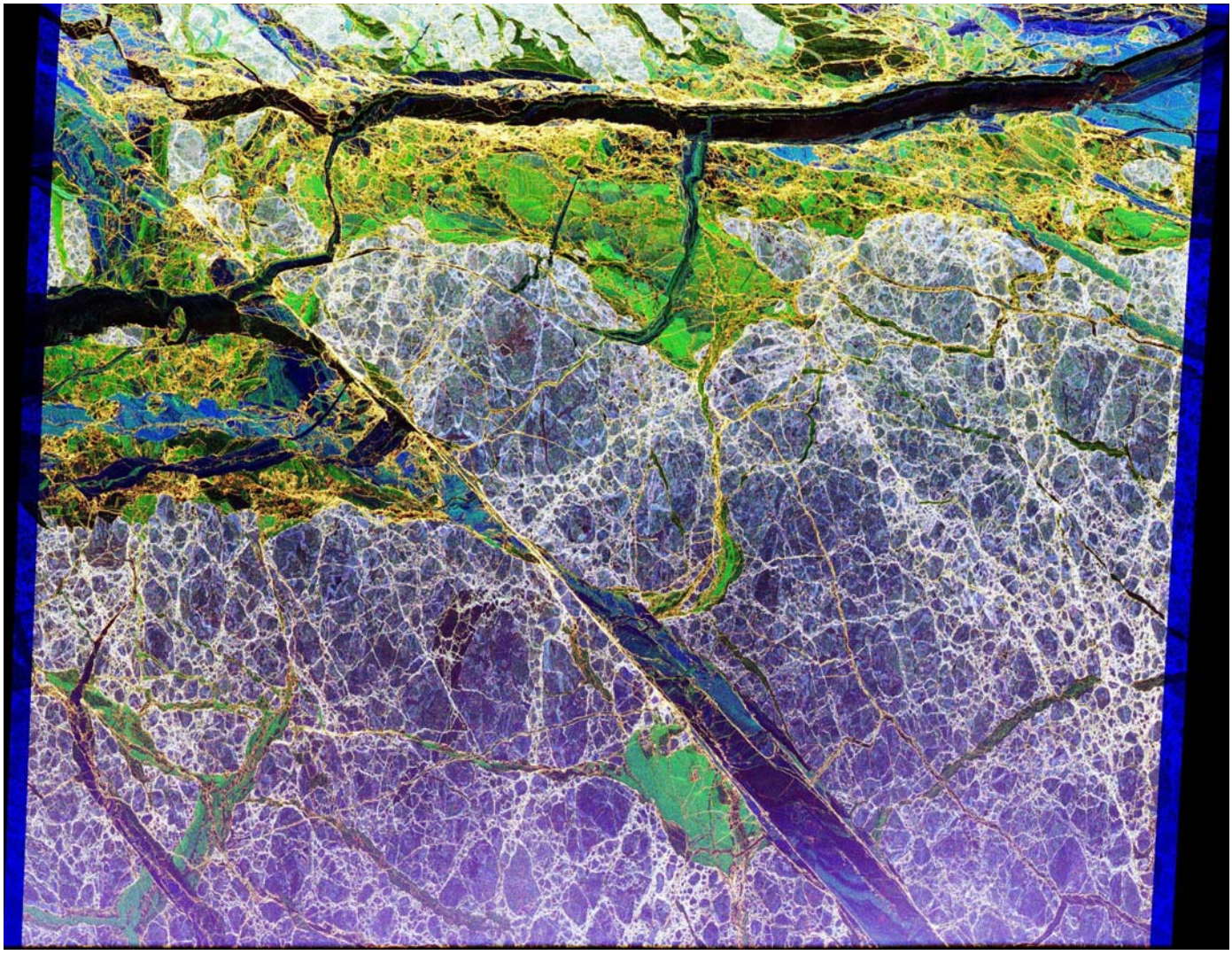

INTEGRATED AIRSAR PROCESSOR

{V. 6.38/2004A.BAAA}

SEAICE218-1

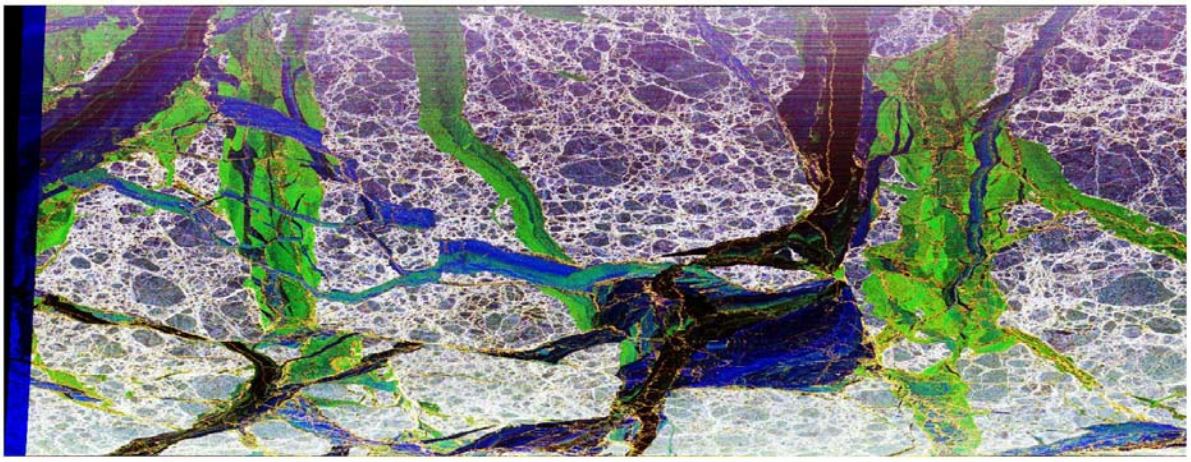

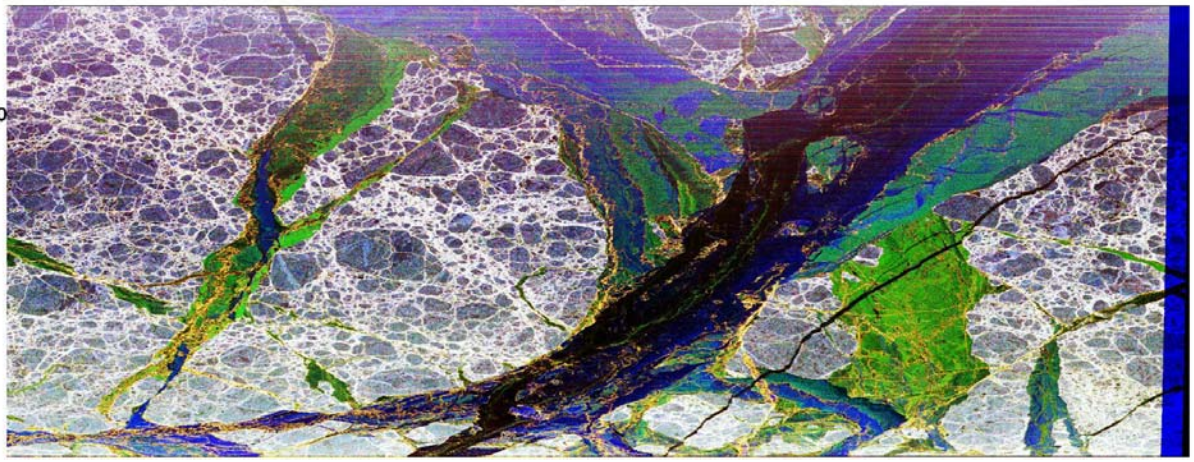

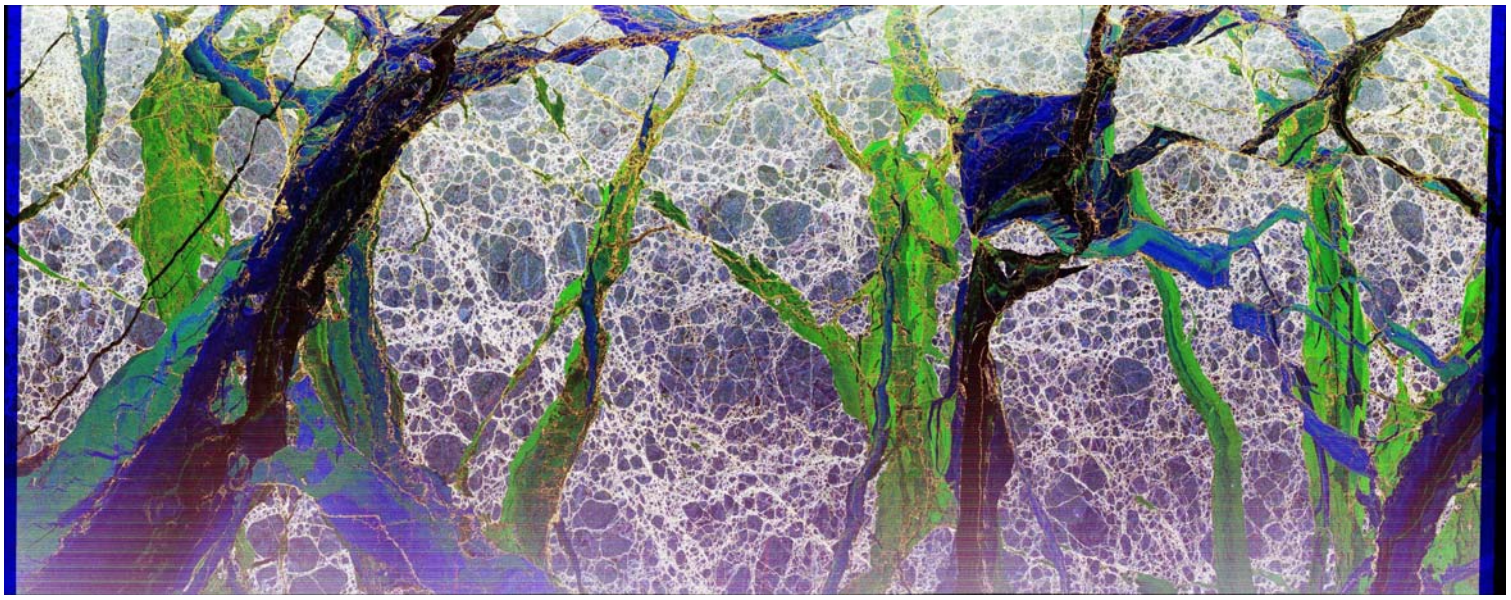

Radar Illumination

Velocity

P-Band Total Power
L-Band Total Power
C-Band Total Power

Date Acquired:
2-DEC-04
Date Processed:
8-FEB-07
CCTID: CM6834

Cntr lat: 72.82
Cntr lon: -138.15
Bandwidth: 20.00
Cross-track:
Slant Swath(km):17.0
samples in data: 2560
reduction ratio: 0.2
Along-track:
Swath(km):60.3
lines in data: 6520
reduction ratio: 0.5

NORTH

INTEGRATED AIRSAR PROCESSOR (V. 6.37/)

SEAICE218-2

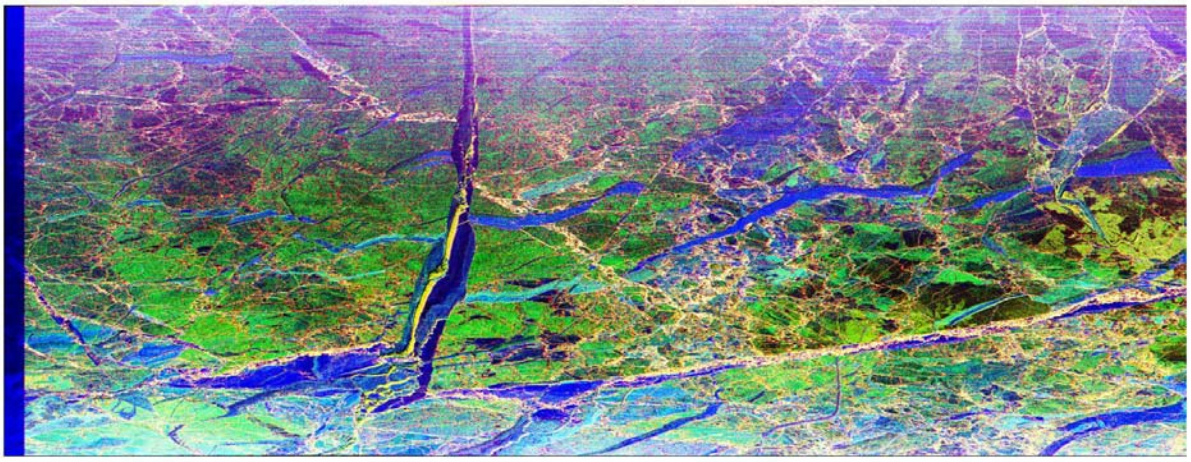

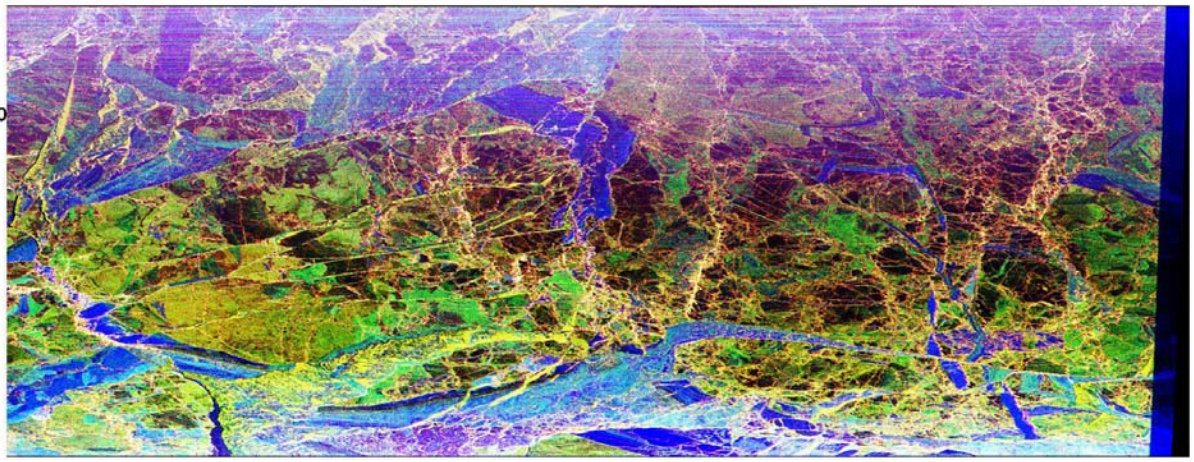

Radar Illumination

Velocity

P-Band Total Power
L-Band Total Power
C-Band Total Power

Date Acquired:
2-DEC-04
Date Processed:
8-MAR-07
CCTID: CM6837

Cntr lat: 71.16
Cntr lon: -142.51
Bandwidth: 20.00
Cross-track:
Slant Swath(km):17.0
samples in data: 2560
reduction ratio: 0.2
Along-track:
Swath(km):60.7
lines in data: 6564
reduction ratio: 0.5

NORTH

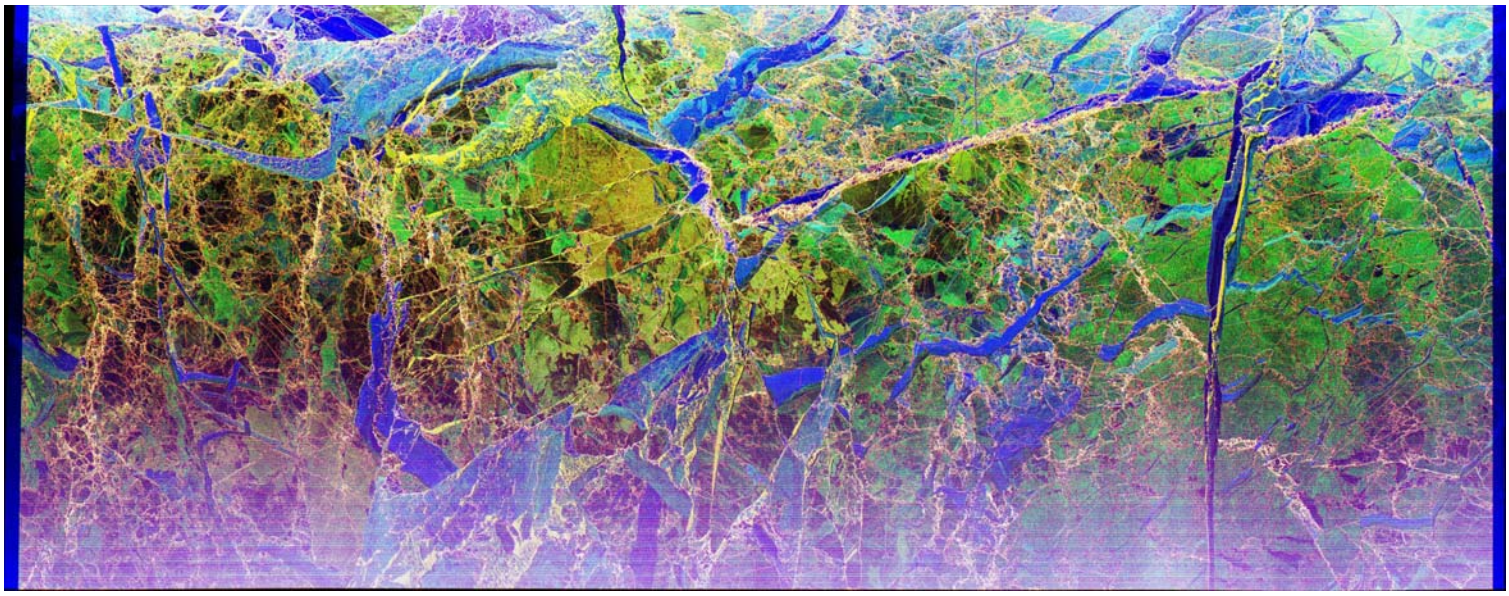

Appendix D **RADARSAT image sequences**

Six image sequences of RADARSAT overpasses of the five AIRSAR scenes (6830, 6831, 6832, 6833 and 6834) are included. The frames are acquired with C-HH polarization. Differences in brightness of the frames within each image sequence could be explained by ascending and descending orbit of the satellite.

RADARSAT imagery overpassing AIRSAR scene 6830 (DAY 322-339 2004)

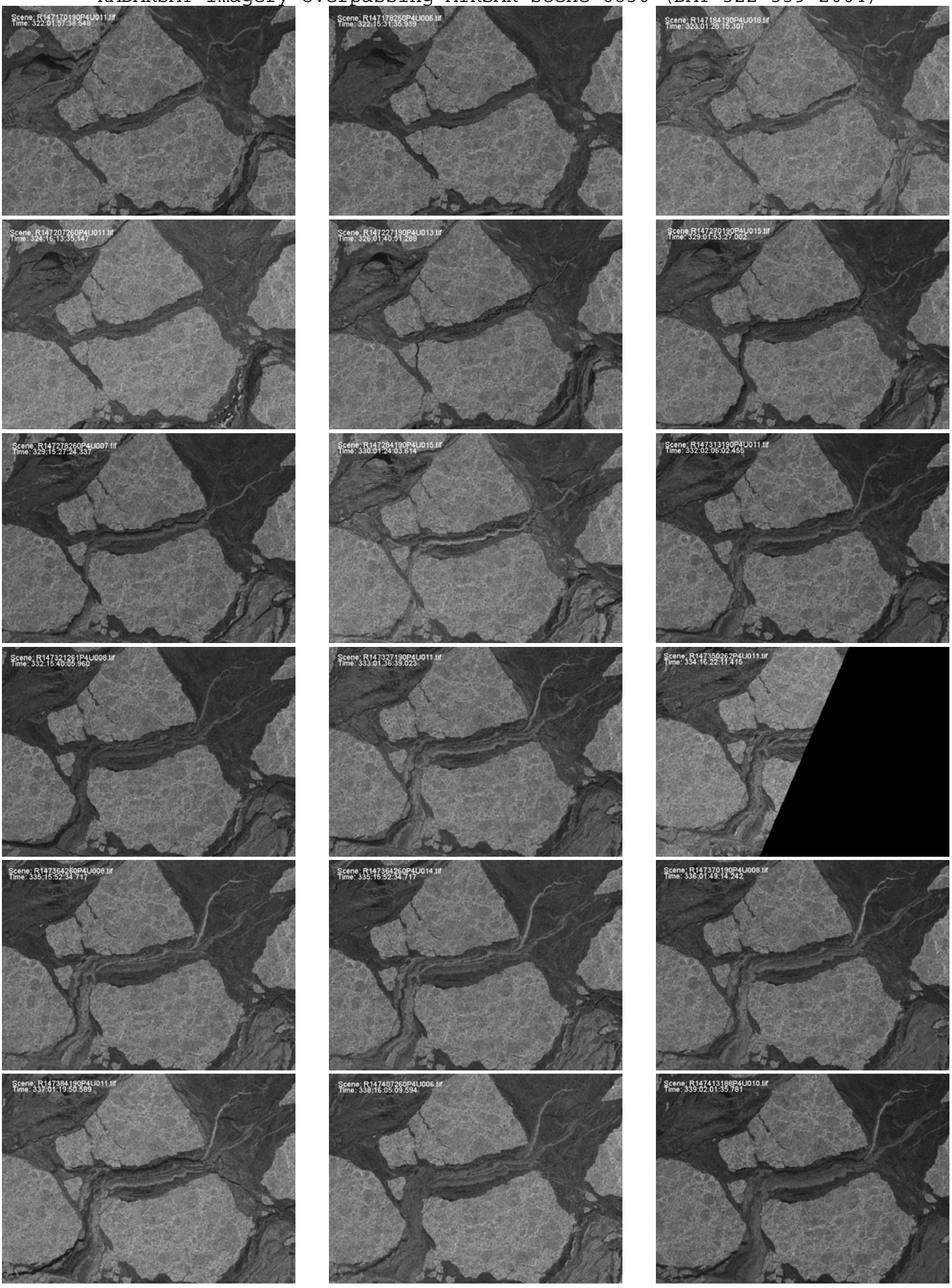

RADARSAT imagery overpassing AIRSAR scene 6831 (DAY 322-339 2004)

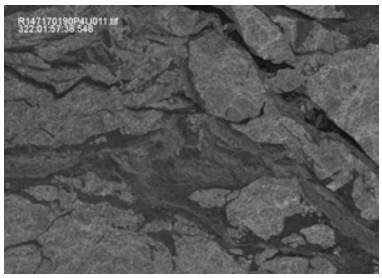

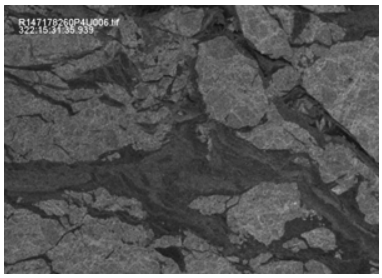

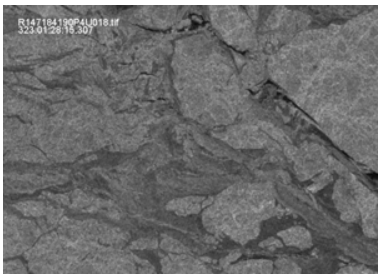

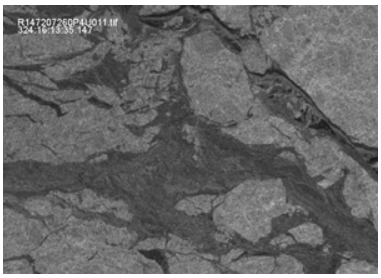

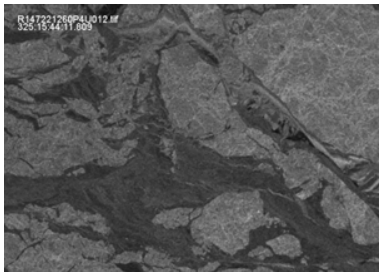

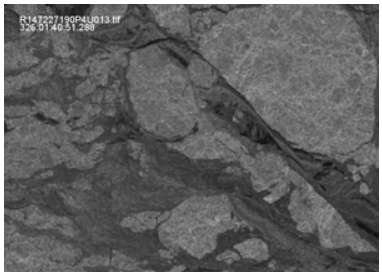

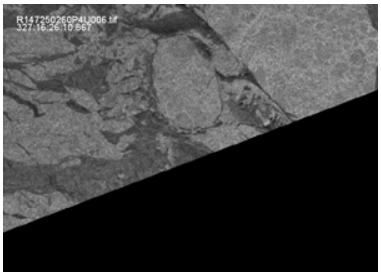

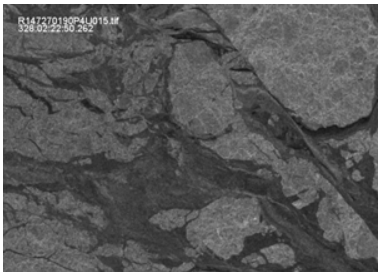

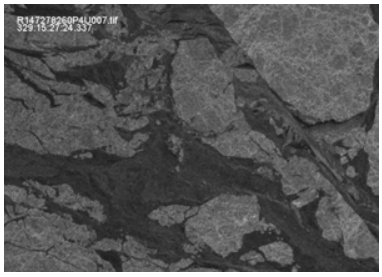

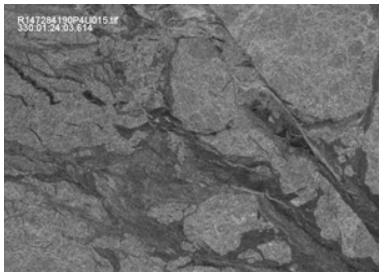

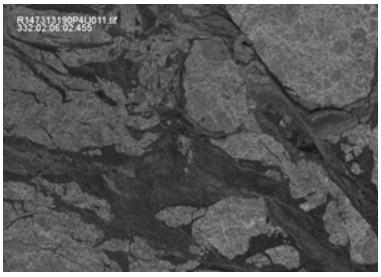

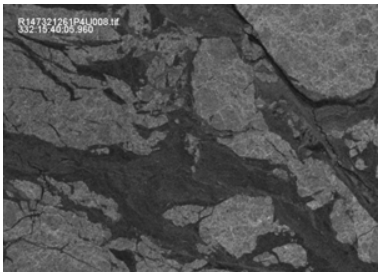

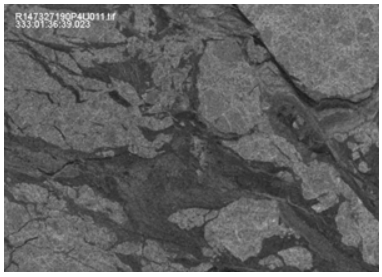

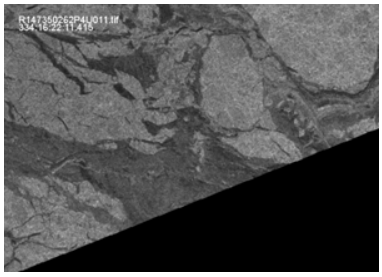

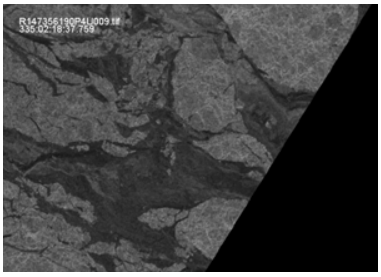

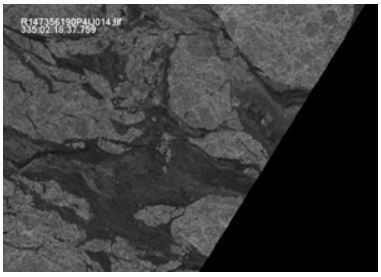

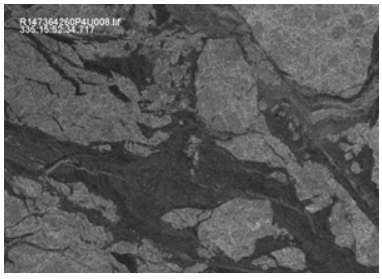

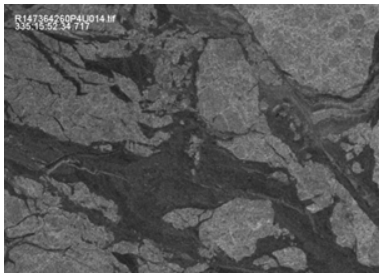

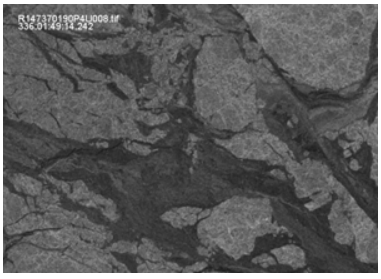

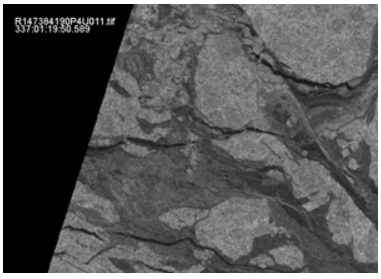

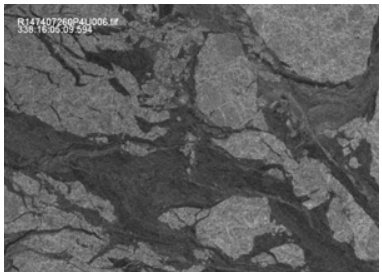

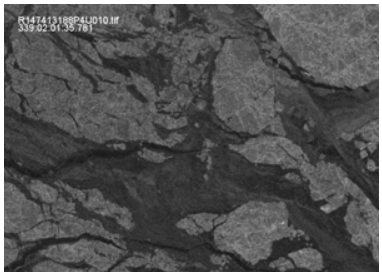

RADARSAT imagery overpassing AIRSAR scene 6832 (DAY 322-339 2004)

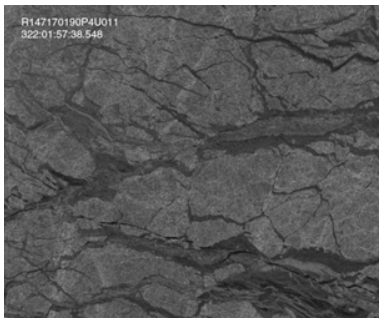

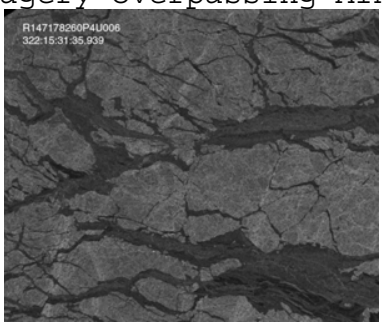

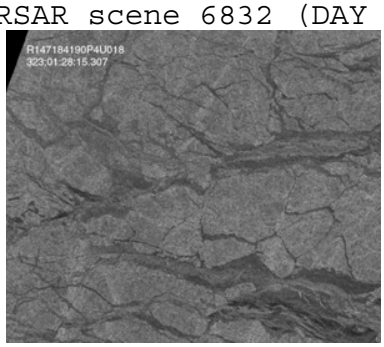

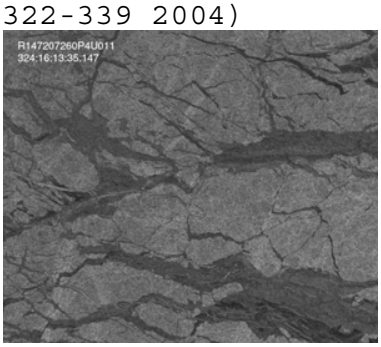

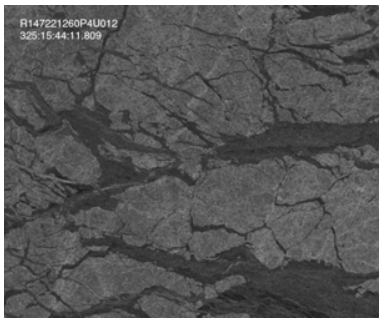

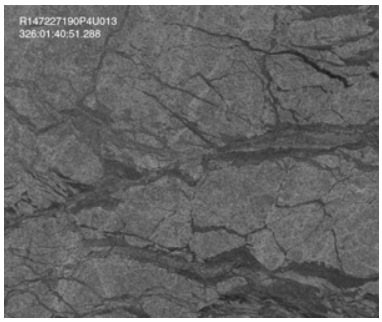

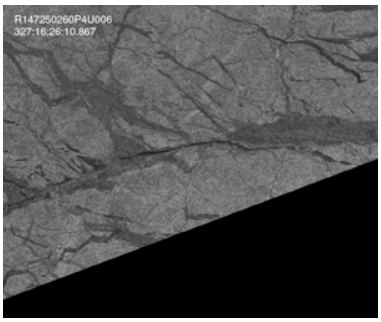

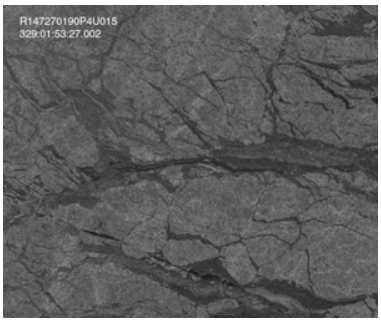

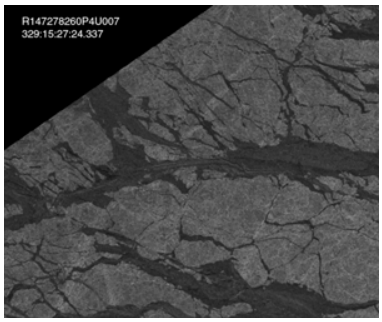

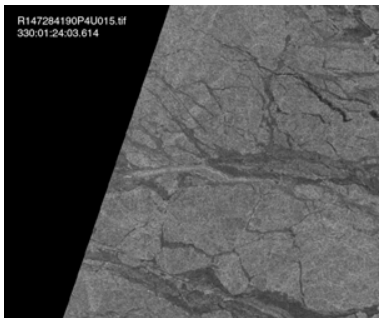

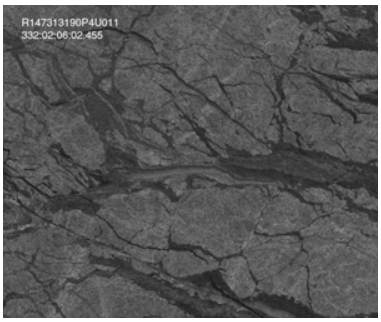

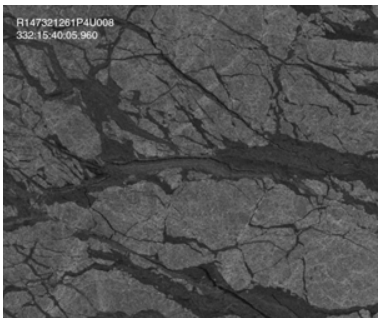

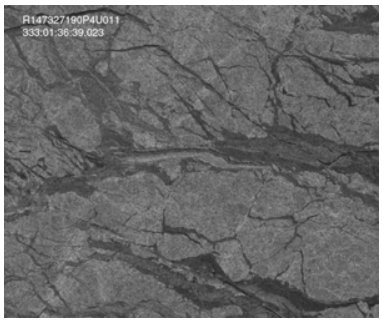

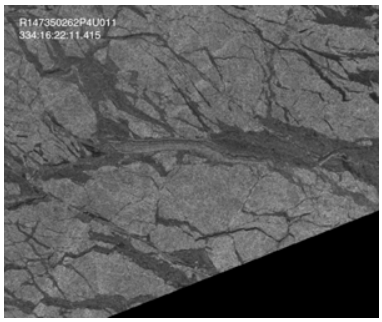

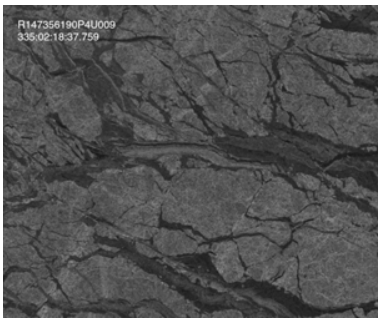

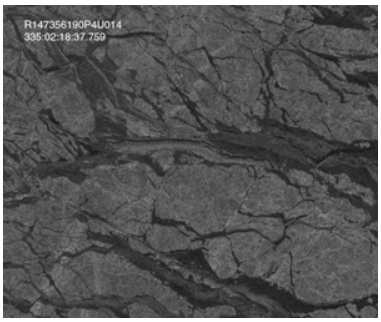

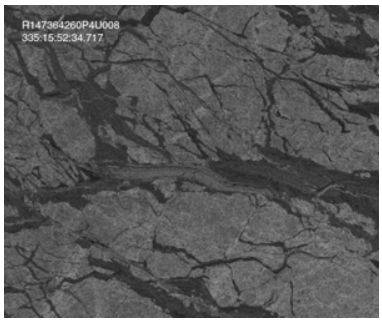

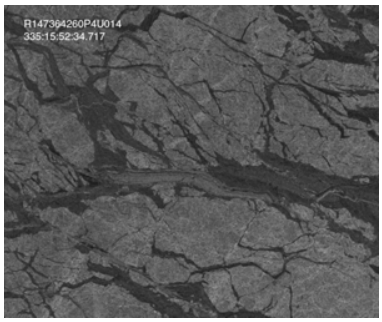

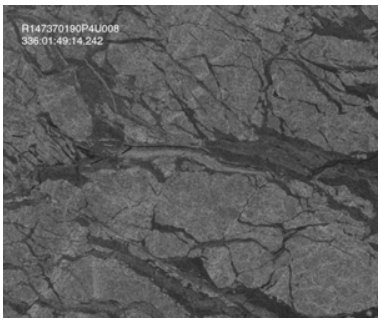

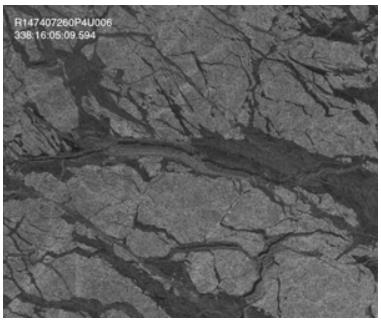

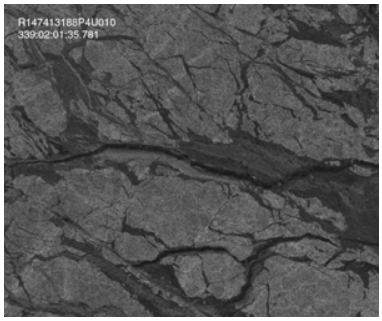

RADARSAT imagery overpassing AIRSAR scene 6833 (DAY 322-339 2004)

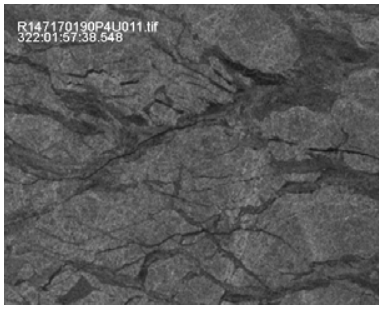

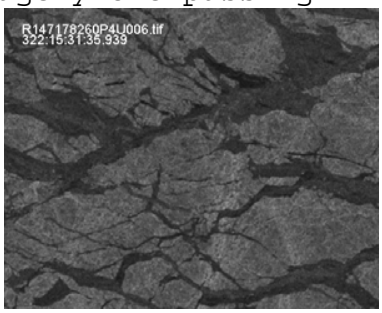

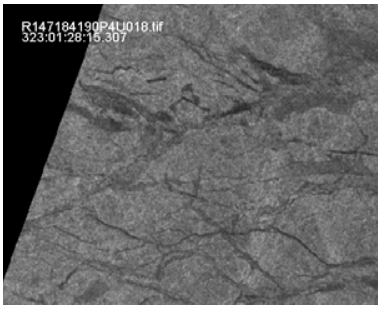

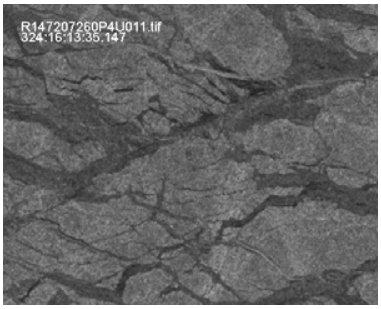

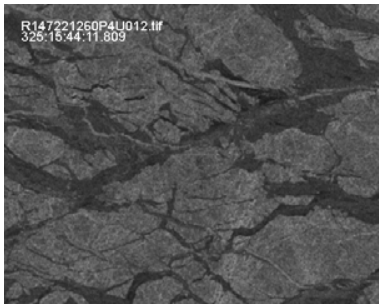

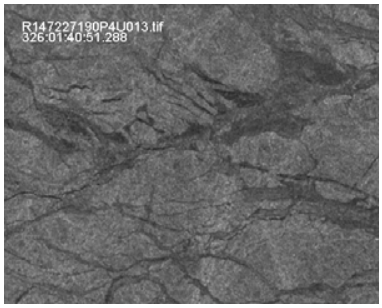

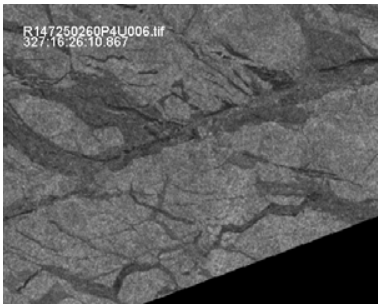

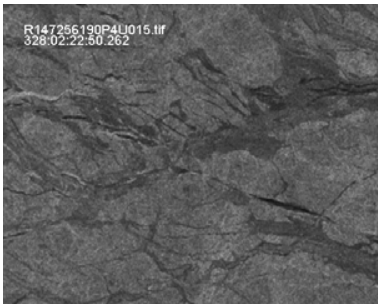

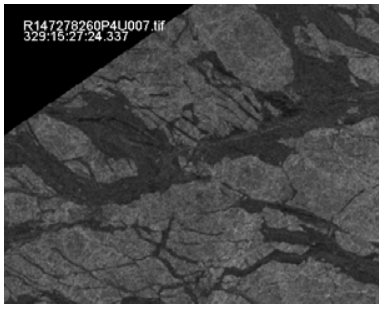

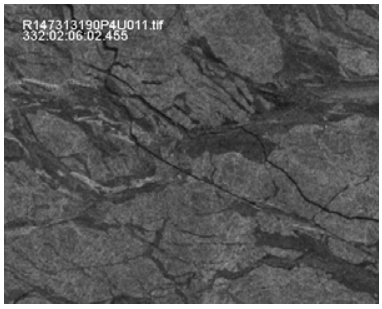

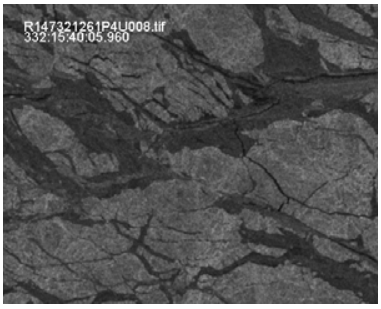

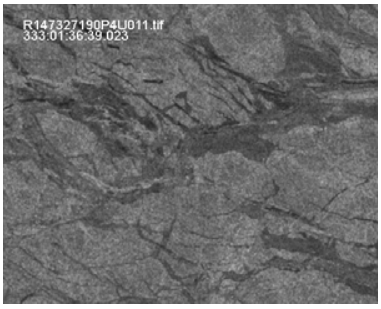

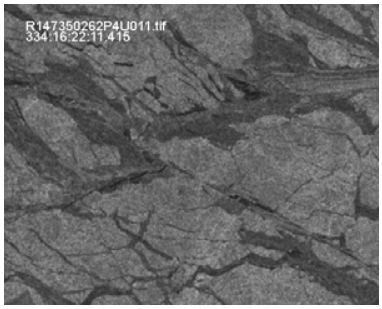

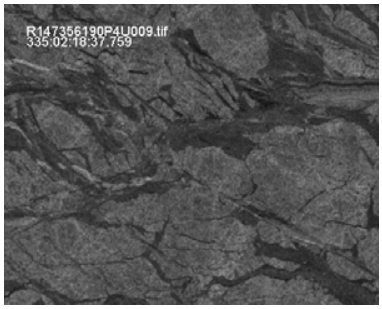

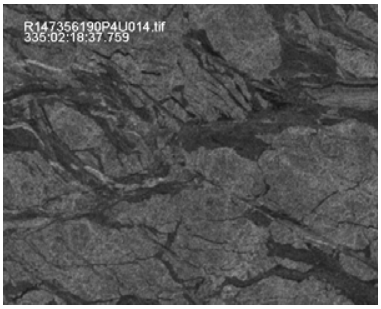

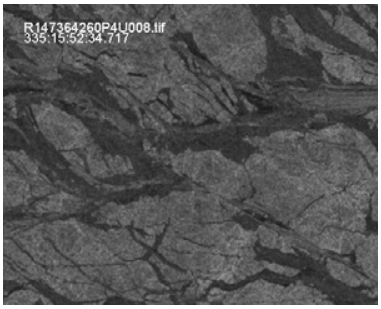

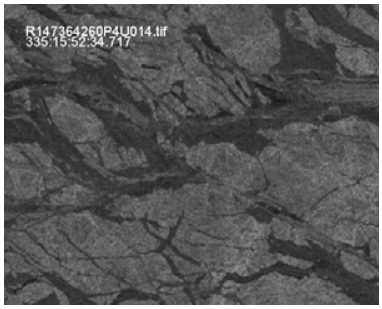

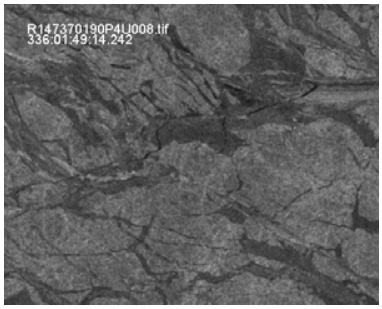

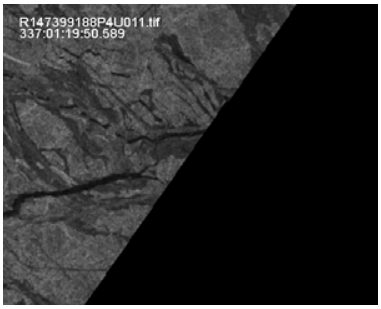

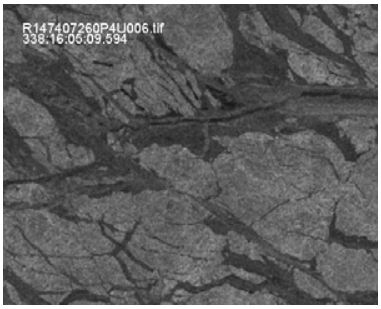

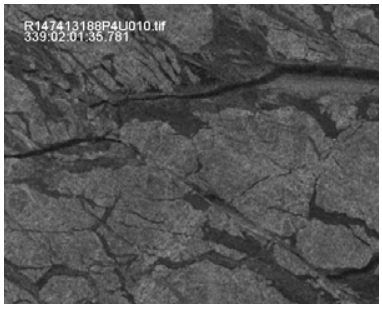

RADARSAT imagery overpassing AIRSAR scene 6834 (DAY 322-339 2004)

Appendix E **Summary of polarimetric signatures**

MEAN VALUES											STANDARD DEVIATIONS												
CHH Mean	CVV Mean	CHV Mean	LHH Mean	LVV Mean	LHV Mean	CHH/ CVV Mean	LHH/ LVV Mean	Phase CHHVV Mean	Phase LHHVV Mean	Phase PHHVV Mean	CHH Std	CVV Std	CHV Std	LHH Std	LVV Std	LHV Std	CHH/ CVV Std	LHH/ LVV Std	Phase CHHVV Std	Phase LHHVV Std	Phase PHHVV Std	Inc angle range	# Samples
Ice1 (1-2 days old)																							
-23.1	-19.2	-32.9	-34.3	-31.7	-42.3	-3.8	-2.7	1.0	2.1	9.4	0.7	0.8	0.3	2.1	2.1	1.1	0.6	0.7	3.7	4.3	6.5	Θ<35	132
-23.8	-18.9	-33.1	-36.8	-32.8	-43.8	-4.8	-3.6	1.1	3.1	-10.5	1.6	1.7	0.9	1.5	2.2	1.3	0.7	1.0	6.5	4.8	24.6	35<Θ<40	1102
-25.3	-20.2	-33.4	-38.0	-33.9	-43.4	-5.0	-3.7	3.4	2.6	-15.2	1.1	1.3	0.6	1.1	1.7	1.4	1.0	1.0	8.5	8.3	25.5	40<Θ<45	2835
-25.4	-19.2	-33.5	-38.1	-33.4	-43.5	-6.0	-4.2	3.5	5.7	-23.7	1.1	1.3	0.6	1.5	2.1	1.3	1.0	1.1	7.5	9.4	35.4	45<Θ<50	1433
-26.1	-19.4	-33.1	-38.5	-33.5	-43.1	-6.6	-4.5	3.8	7.1	-13.7	1.2	1.3	0.6	2.0	2.3	1.7	1.0	1.4	7.8	8.9	32.0	50<Θ<55	2256
Ice2 (9-14 days old)																							
-18.2	-15.7	-29.3	-30.9	-26.7	-44.1	-2.4	-4.2	-12.6	7.4	3.0	0.2	0.3	0.2	0.6	0.8	0.4	0.2	0.3	3.6	1.3	1.3	Θ<35	21
-18.4	-16.4	-29.7	-28.6	-26.1	-38.6	-2.0	-2.7	-2.4	3.5	6.7	0.7	0.7	0.7	3.1	2.5	3.3	0.5	1.4	7.6	3.8	5.7	35<Θ<40	448
-17.0	-15.6	-28.0	-32.3	-27.0	-42.3	-1.5	-5.0	6.1	11.9	0.2	1.7	0.8	1.5	2.3	2.6	1.7	1.2	1.2	15.6	6.5	8.1	40<Θ<45	898
-16.0	-14.6	-26.2	-31.5	-25.2	-40.9	-1.5	-6.6	8.3	18.6	-2.4	2.2	1.1	1.9	3.3	3.0	2.6	1.3	0.9	11.2	7.8	9.1	45<Θ<50	1246
-17.6	-16.0	-27.6	-33.7	-26.3	-40.6	-1.7	-7.2	8.9	24.0	-5.2	2.3	1.3	2.1	3.2	3.4	2.6	1.2	1.1	11.9	12.3	13.1	50<Θ<55	1045
Ice3 (>15 days old)																							
-19.5	-18.8	-32.9	-24.3	-21.4	-40.5	-0.7	-3.0	6.8	10.5	7.2	0.4	0.5	0.5	0.5	0.3	0.4	0.6	0.3	1.5	3.3	2.3	Θ<35	67
-20.6	-19.9	-33.7	-25.1	-21.5	-41.6	-0.7	-3.5	5.1	14.1	7.2	0.7	0.7	0.4	0.4	0.8	0.6	0.6	0.7	4.7	5.7	2.7	35<Θ<40	100
-20.2	-18.9	-32.9	-26.3	-22.4	-39.8	-1.3	-3.8	10.9	19.5	7.8	1.5	1.4	1.2	2.0	2.0	2.4	0.6	1.0	7.5	8.0	5.5	40<Θ<45	312
-20.6	-19.5	-32.1	-26.8	-22.7	-38.6	-1.1	-4.2	4.8	25.0	16.8	1.6	1.4	1.6	3.7	3.3	3.6	0.6	1.6	7.4	11.5	6.5	45<Θ<50	645
-21.8	-20.1	-31.8	-28.0	-23.8	-38.4	-1.6	-4.2	1.0	30.1	17.2	1.4	1.4	1.5	3.4	3.0	3.7	0.7	1.8	6.6	14.3	8.7	50<Θ<55	1168
Ice4 (MY ice)																							
-10.7	-8.7	-18.0	-16.1	-14.8	-26.3	-1.8	-1.4	-4.2	0.5	0.1	0.9	1.1	1.5	1.4	1.2	3.6	0.6	0.4	3.2	1.4	1.6	Θ<35	72
-11.9	-10.0	-19.2	-18.7	-17.0	-28.1	-1.9	-1.8	-2.5	-0.2	0.1	1.0	1.2	2.0	2.1	2.0	4.8	0.4	0.4	3.5	1.7	2.8	35<Θ<40	192
-13.1	-11.1	-20.6	-21.1	-19.1	-30.6	-1.9	-2.2	0.6	0.4	-0.4	1.2	1.4	2.0	2.6	2.1	4.5	0.5	0.6	4.4	3.1	3.7	40<Θ<45	294
-14.4	-12.4	-22.0	-23.2	-21.0	-32.5	-2.1	-2.4	-1.2	-0.2	0.7	1.3	1.3	2.1	2.6	2.2	4.4	0.3	0.5	4.8	1.7	3.3	45<Θ<50	533
-14.6	-12.6	-21.7	-23.7	-21.5	-32.1	-2.0	-2.6	-2.2	-1.8	-0.4	1.4	1.3	2.2	2.8	2.4	4.8	0.3	0.6	5.0	2.5	3.3	50<Θ<55	721
Ice5 (2-3 days old)																							
-24.2	-17.8	-31.7	-37.8	-30.7	-44.0	-6.4	-6.3	11.9	-0.5	3.7	0.9	0.6	0.5	1.0	2.2	0.6	0.9	1.8	4.1	6.4	9.0	50<Θ<55	407
Ice6 (~Hours old)																							
-30.6	-25.3	-36.7	-35.9	-33.3	-44.7	-5.2	-2.6	17.6	-6.8	0.6	0.7	0.8	0.5	1.1	0.8	1.1	0.5	0.6	9.7	4.2	5.7	Θ<35	405
-31.0	-25.0	-37.0	-40.1	-35.7	-45.2	-5.8	-4.0	39.0	17.2	12.1	1.2	1.5	0.7	1.5	2.0	0.5	0.8	0.8	10.7	8.9	9.5	35<Θ<40	603
-32.4	-25.8	-36.8	-37.9	-33.8	-43.4	-6.5	-4.0	40.2	-6.4	1.5	0.7	1.0	0.5	0.8	1.0	0.8	0.6	0.6	11.5	6.0	5.2	40<Θ<45	770
-32.1	-24.2	-35.4	-41.8	-35.6	-45.1	-7.9	-6.1	44.9	-1.1	-0.7	0.5	0.9	0.3	0.8	0.9	1.1	0.6	0.6	11.0	7.0	10.9	45<Θ<50	102
-32.3	-24.2	-35.5	-40.9	-34.7	-45.1	-7.7	-5.8	35.1	-2.6	-1.6	0.8	1.6	0.4	1.4	1.9	1.3	0.9	1.0	14.3	4.1	6.1	50<Θ<55	61

Appendix F **Polarimetric signatures for all transects**

Type refers to ice type:

Type 1 Ice 1-2 day old (Ice1)
Type 2 Ice 9-14 days old (Ice2)
Type3 Ice >15 days (Ice3)
Type4 MY ice (Ice4)
Type5 Ice 2-3 days old (Ice5)
Type6 Ice <1 day old (Ice6)

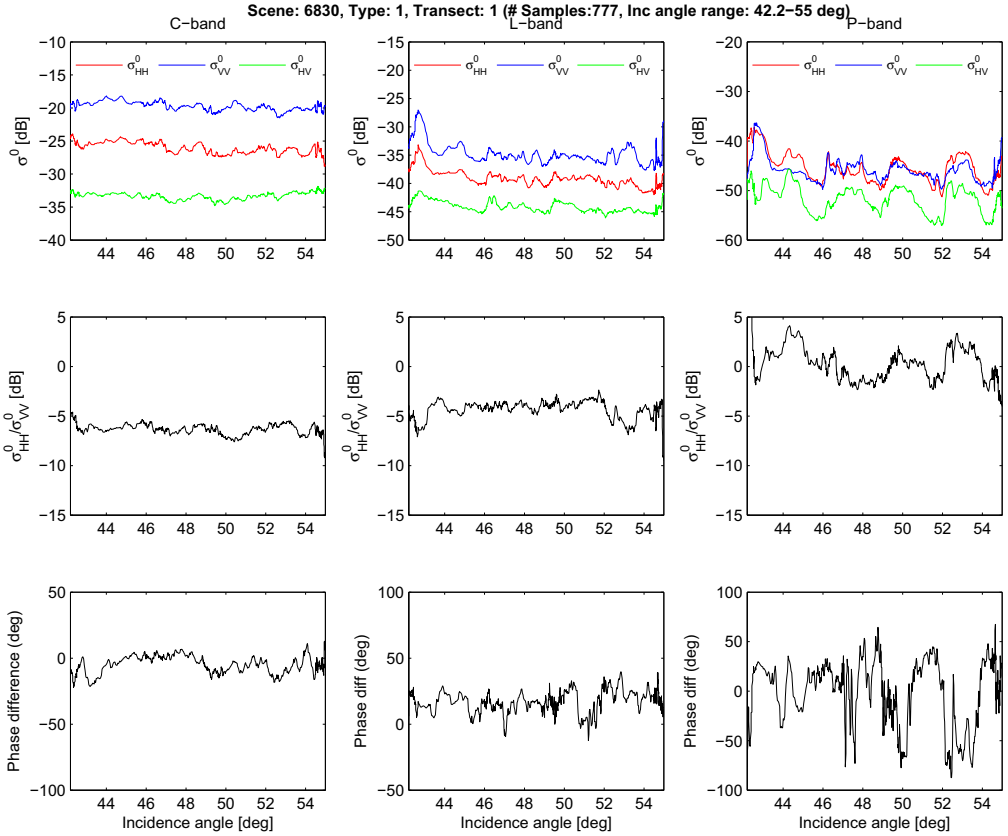
Scene: 6830, Type: 1, Transect: 1 (# Samples:777, Inc angle range: 42.2−55 deg)
C−band
L−band
P−band
σ0 [dB]
σ0HH/σ0VV [dB]
Phase difference (deg)
Phase diff (deg)
Incidence angle [deg]

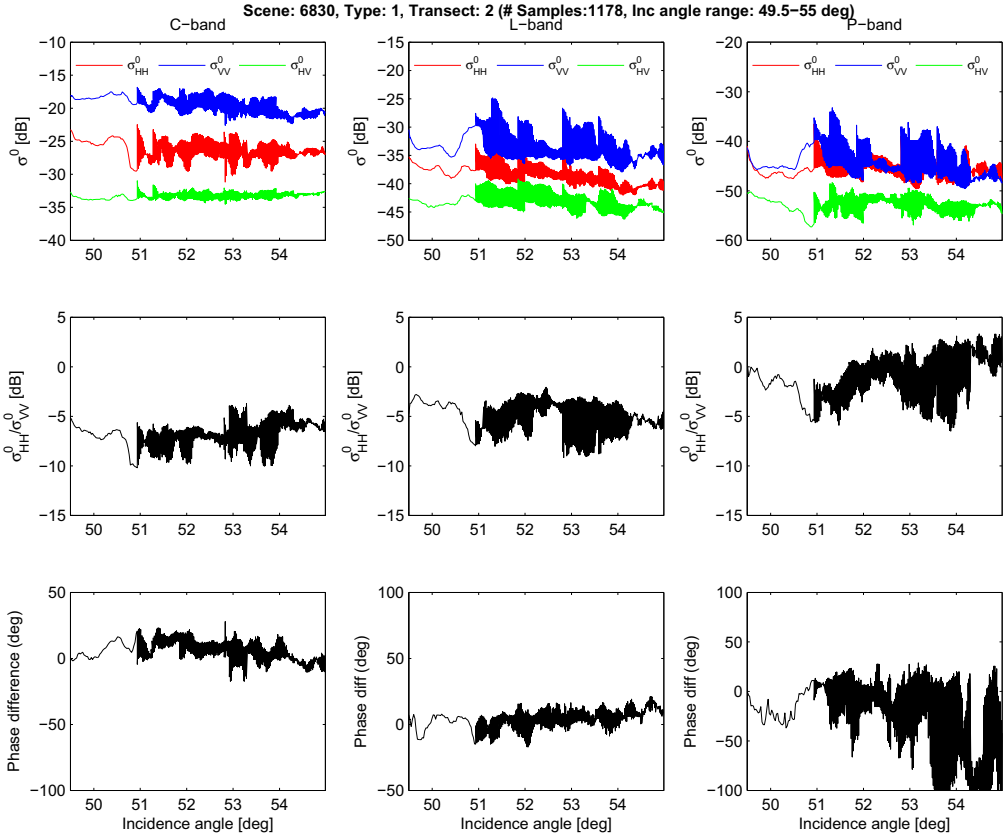
Scene: 6830, Type: 1, Transect: 2 (# Samples:1178, Inc angle range: 49.5−55 deg)
C−band
L−band
P−band
σ0 [dB]
σ0HH/σ0VV [dB]
Phase difference (deg)
Phase diff (deg)
Incidence angle [deg]

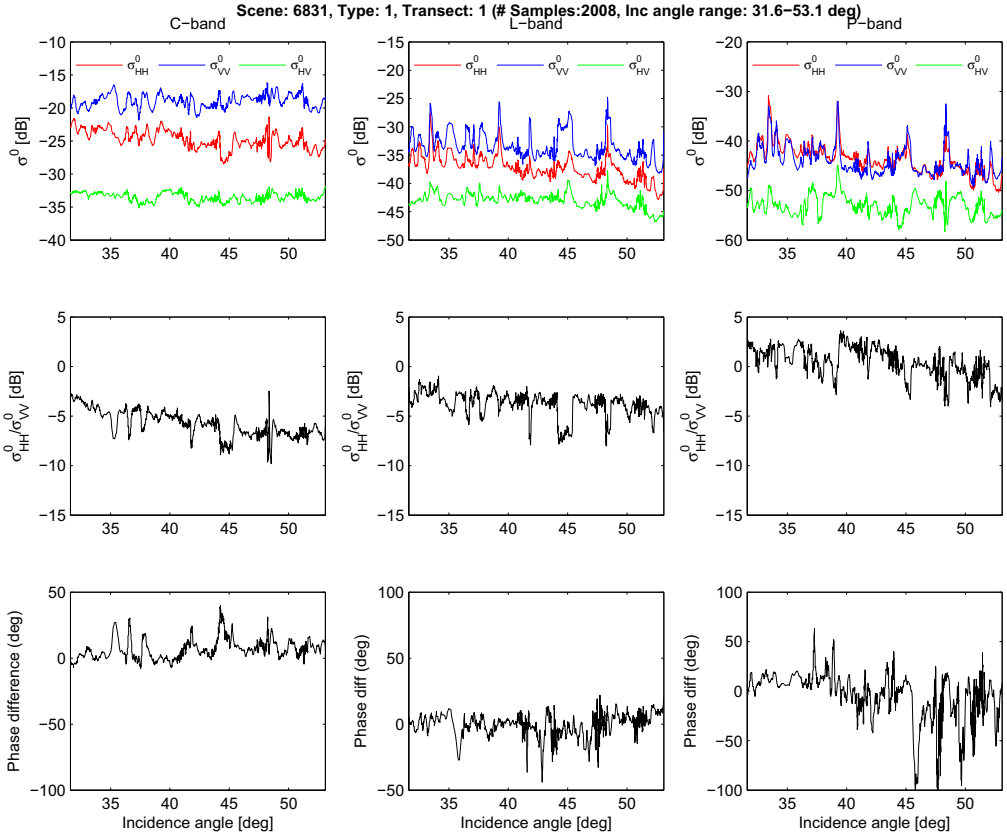
Scene: 6831, Type: 1, Transect: 1 (# Samples:2008, Inc angle range: 31.6−53.1 deg)
C−band
L−band
P−band
σ0 [dB]
σ0HH/σ0VV [dB]
Phase difference (deg)
Phase diff (deg)
Incidence angle [deg]

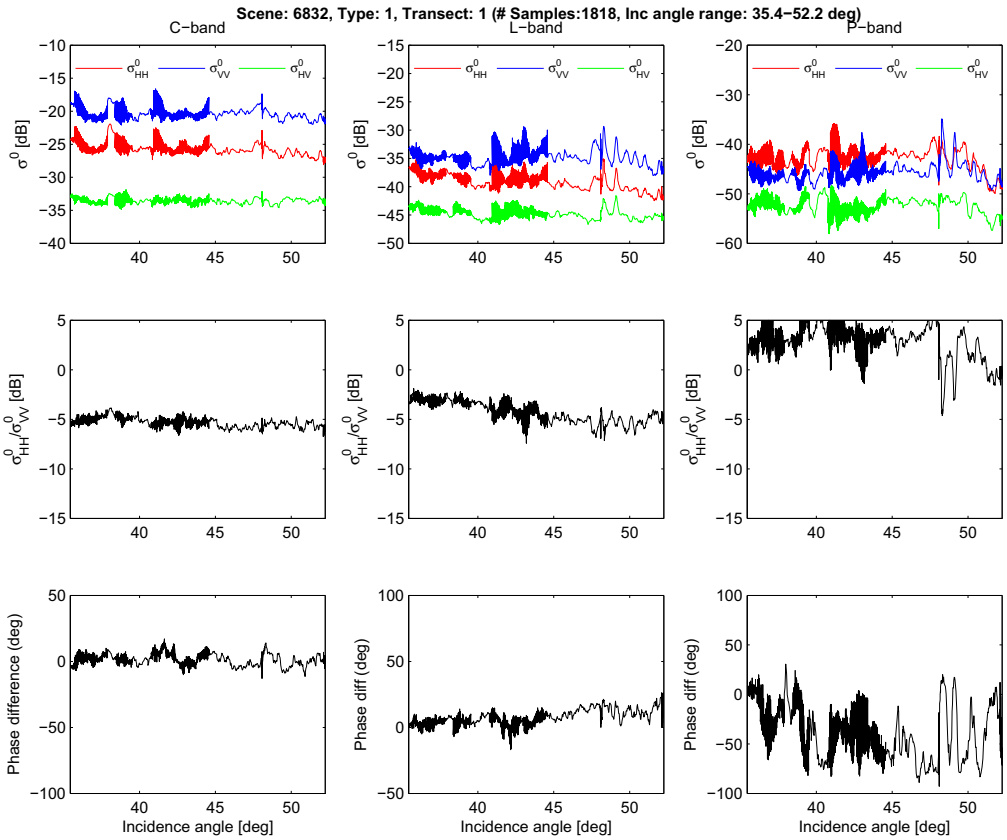
Scene: 6832, Type: 1, Transect: 1 (# Samples:1818, Inc angle range: 35.4−52.2 deg)
C−band
L−band
P−band
σ0 [dB]
σ0HH/σ0VV [dB]
Phase difference (deg)
Phase diff (deg)
Incidence angle [deg]

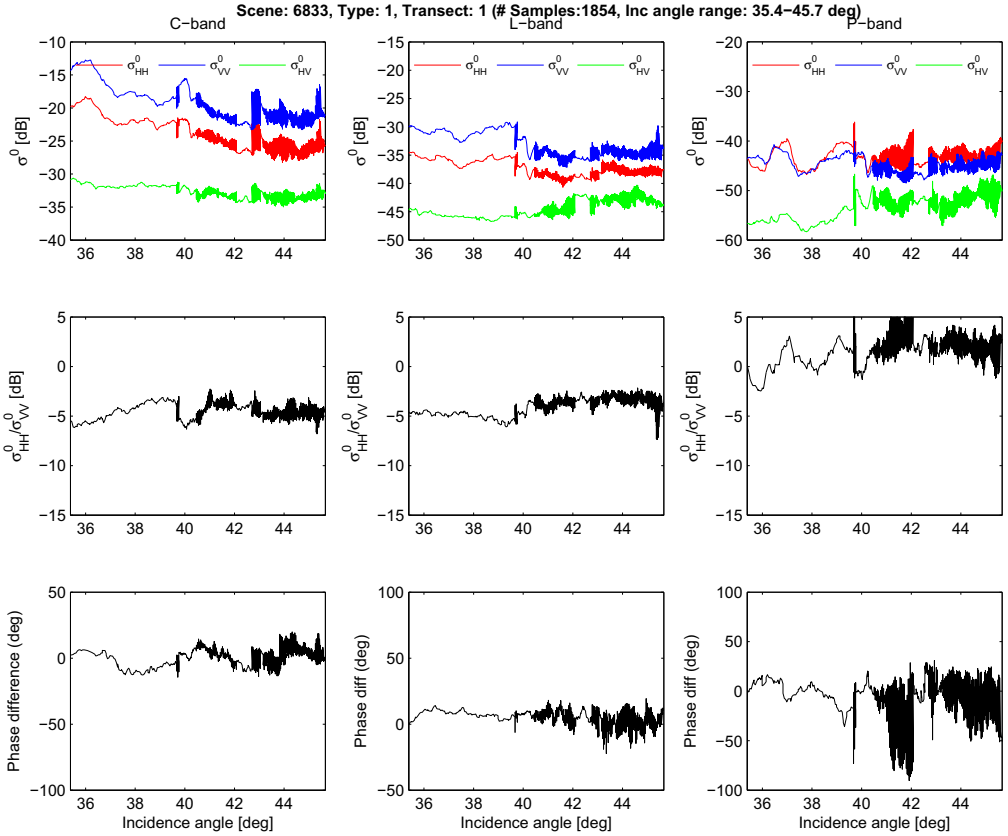
Scene: 6833, Type: 1, Transect: 1 (# Samples:1854, Inc angle range: 35.4−45.7 deg)
C−band
L−band
P−band
σ⁰HH
σ⁰VV
σ⁰HV
σ⁰ [dB]
σ⁰HH/σ⁰VV [dB]
Phase difference (deg)
Phase diff (deg)
Incidence angle [deg]

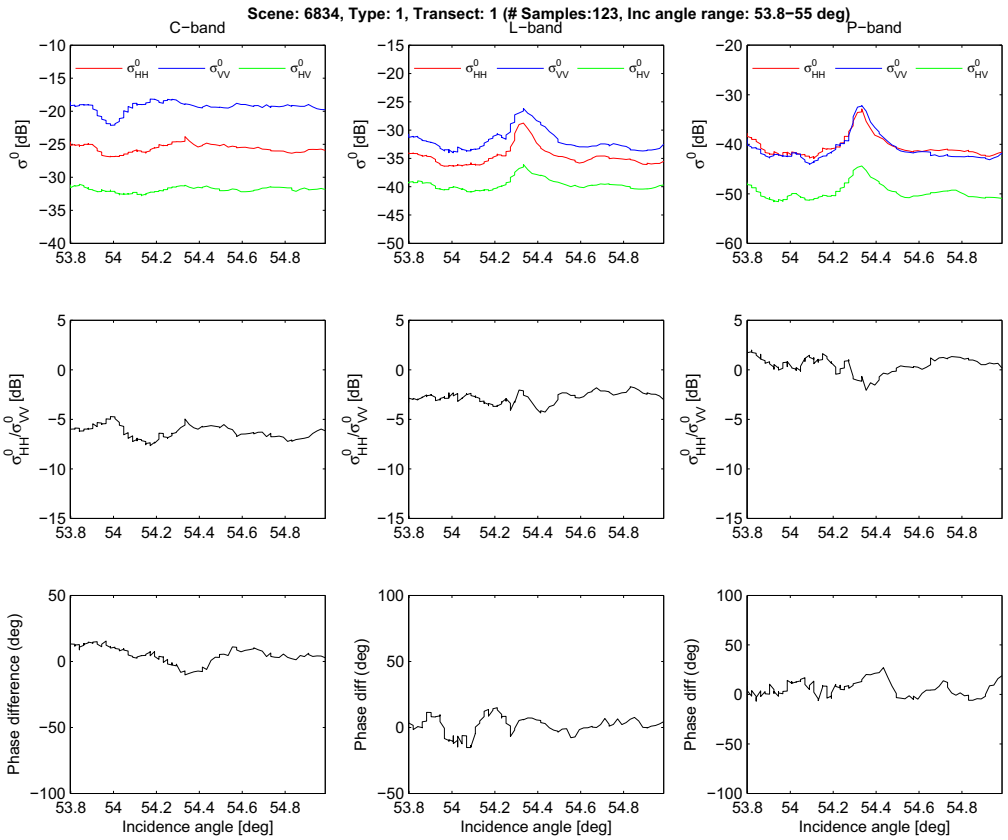
Scene: 6834, Type: 1, Transect: 1 (# Samples:123, Inc angle range: 53.8−55 deg)
C−band
L−band
P−band
σ⁰HH
σ⁰VV
σ⁰HV
σ⁰ [dB]
σ⁰HH/σ⁰VV [dB]
Phase difference (deg)
Phase diff (deg)
Incidence angle [deg]

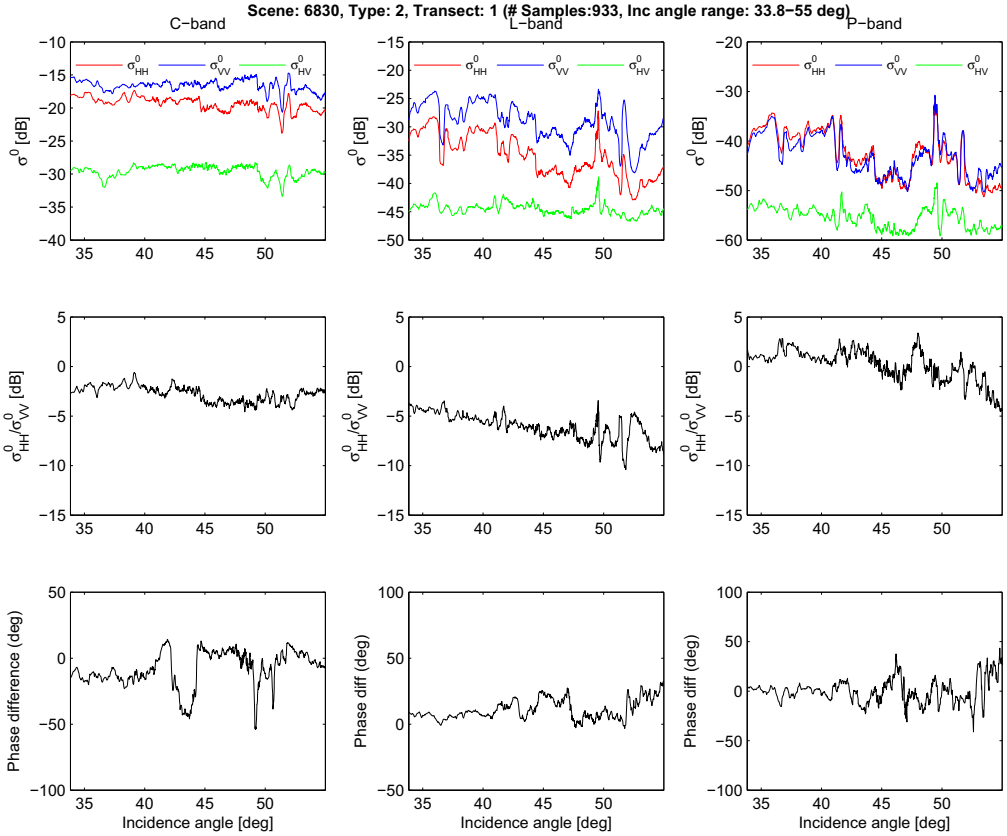
Scene: 6830, Type: 2, Transect: 1 (# Samples:933, Inc angle range: 33.8−55 deg)
C−band
L−band
P−band
σ0HH
σ0VV
σ0HV
σ0 [dB]
σ0HH/σ0VV [dB]
Phase difference (deg)
Phase diff (deg)
Incidence angle [deg]

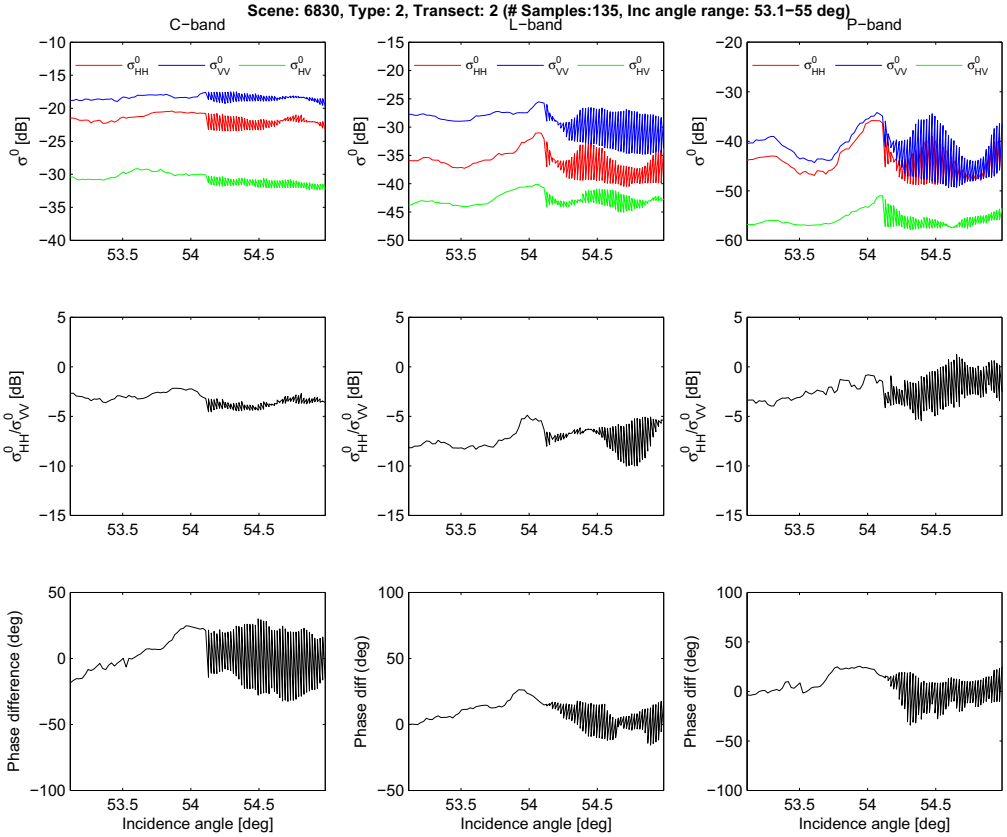
Scene: 6830, Type: 2, Transect: 2 (# Samples:135, Inc angle range: 53.1−55 deg)
C−band
L−band
P−band
σ0HH
σ0VV
σ0HV
σ0 [dB]
σ0HH/σ0VV [dB]
Phase difference (deg)
Phase diff (deg)
Incidence angle [deg]

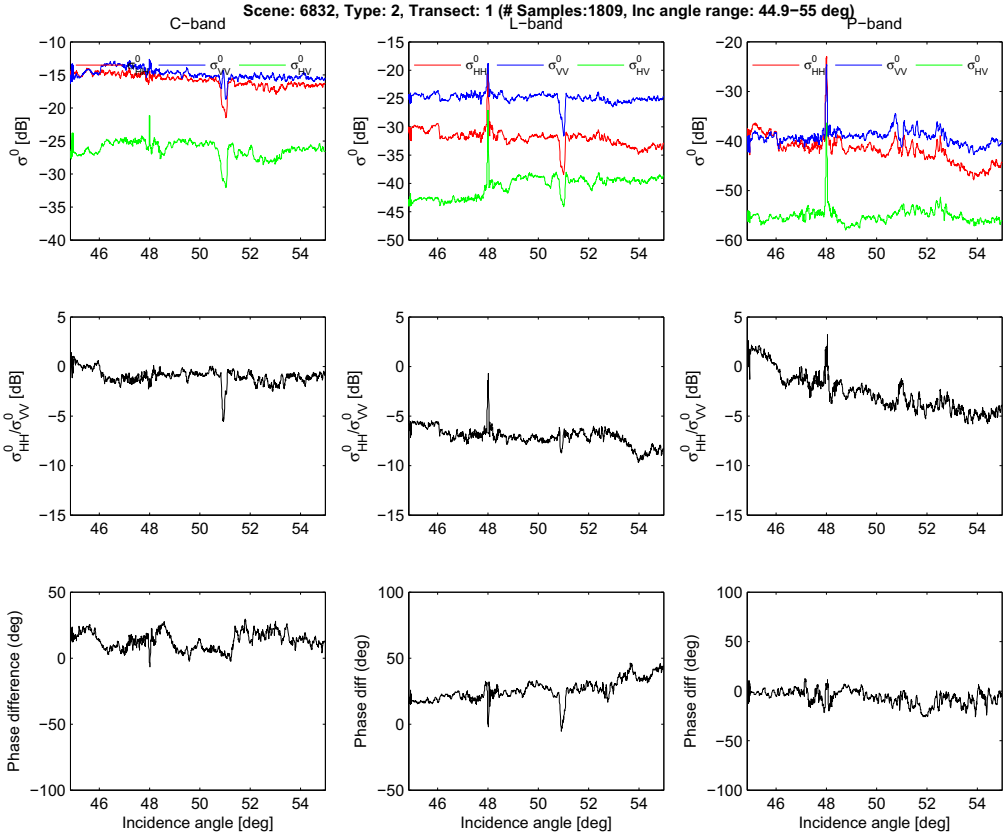
Scene: 6832, Type: 2, Transect: 1 (# Samples:1809, Inc angle range: 44.9−55 deg)
C−band
L−band
P−band
σ0 [dB]
σ0HH/σ0VV [dB]
Phase difference (deg)
Phase diff (deg)
Incidence angle [deg]

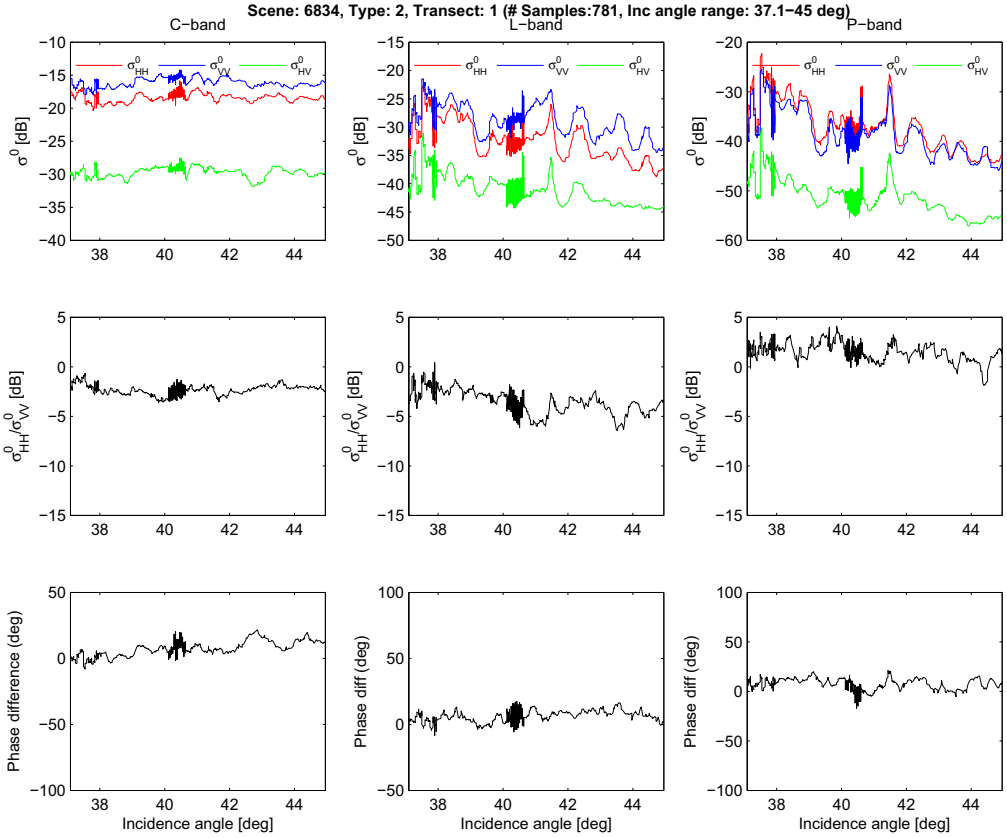
Scene: 6834, Type: 2, Transect: 1 (# Samples:781, Inc angle range: 37.1−45 deg)
C−band
L−band
P−band
σ0 [dB]
σ0HH/σ0VV [dB]
Phase difference (deg)
Phase diff (deg)
Incidence angle [deg]

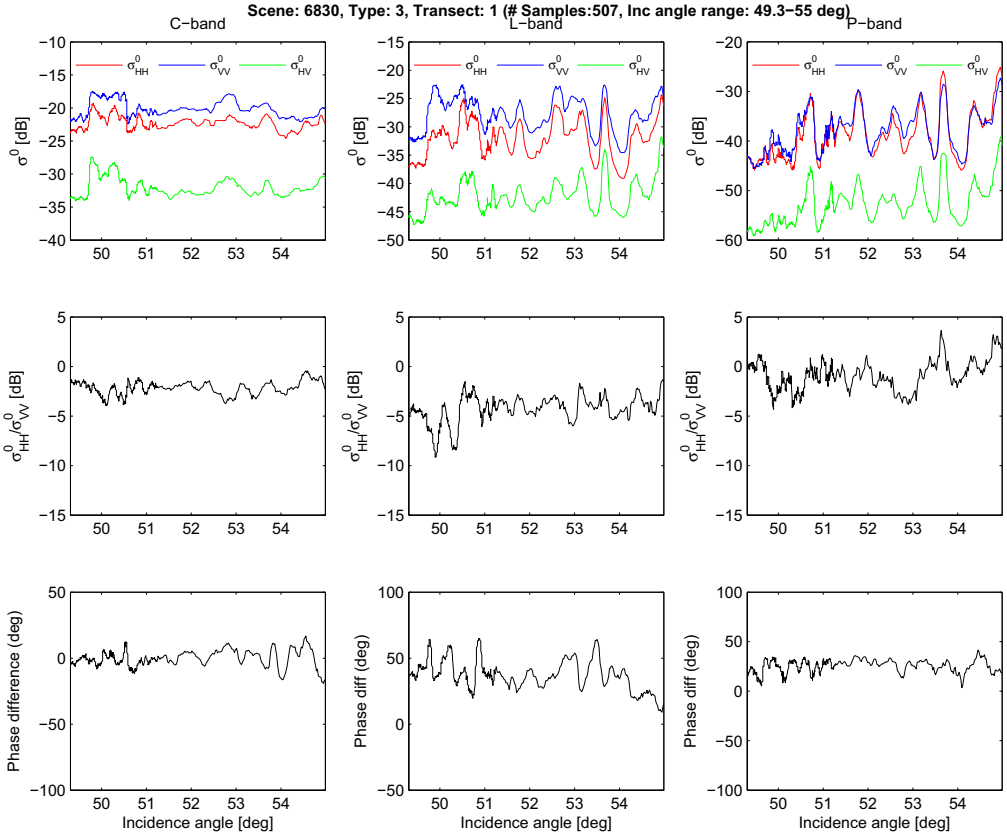
Scene: 6830, Type: 3, Transect: 1 (# Samples:507, Inc angle range: 49.3−55 deg)
C−band
L−band
P−band
σ0 [dB]
σ0HH/σ0VV [dB]
Phase difference (deg)
Phase diff (deg)
Incidence angle [deg]

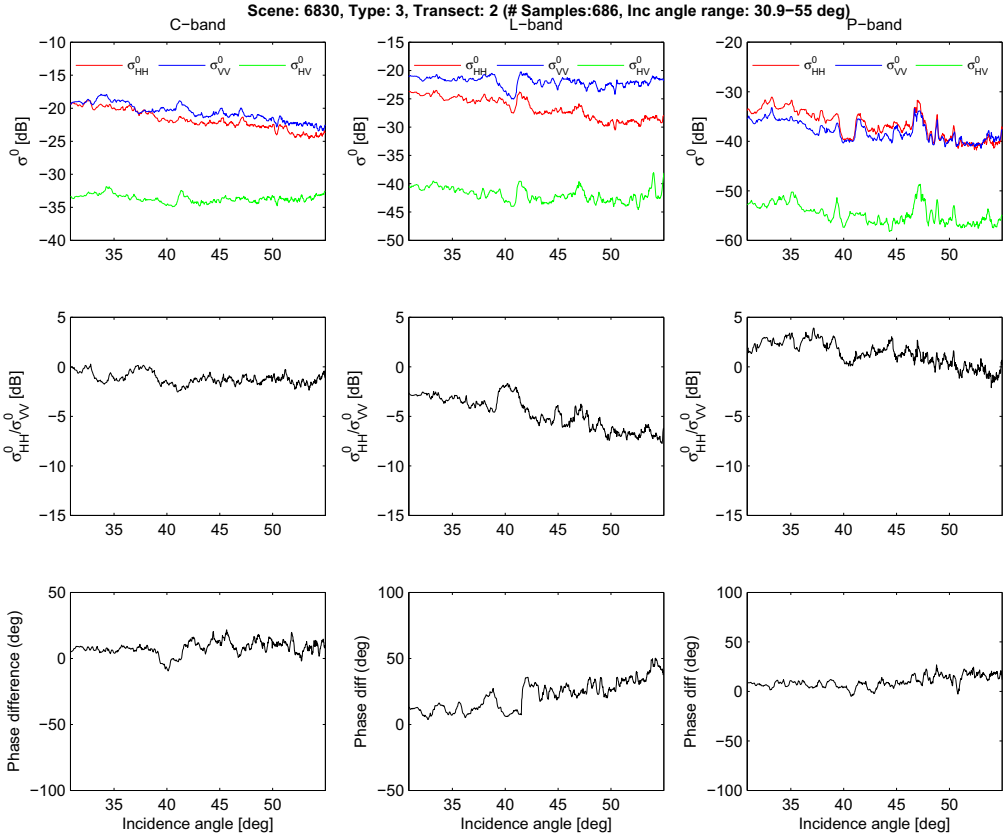
Scene: 6830, Type: 3, Transect: 2 (# Samples:686, Inc angle range: 30.9−55 deg)
C−band
L−band
P−band
σ0 [dB]
σ0HH/σ0VV [dB]
Phase difference (deg)
Phase diff (deg)
Incidence angle [deg]

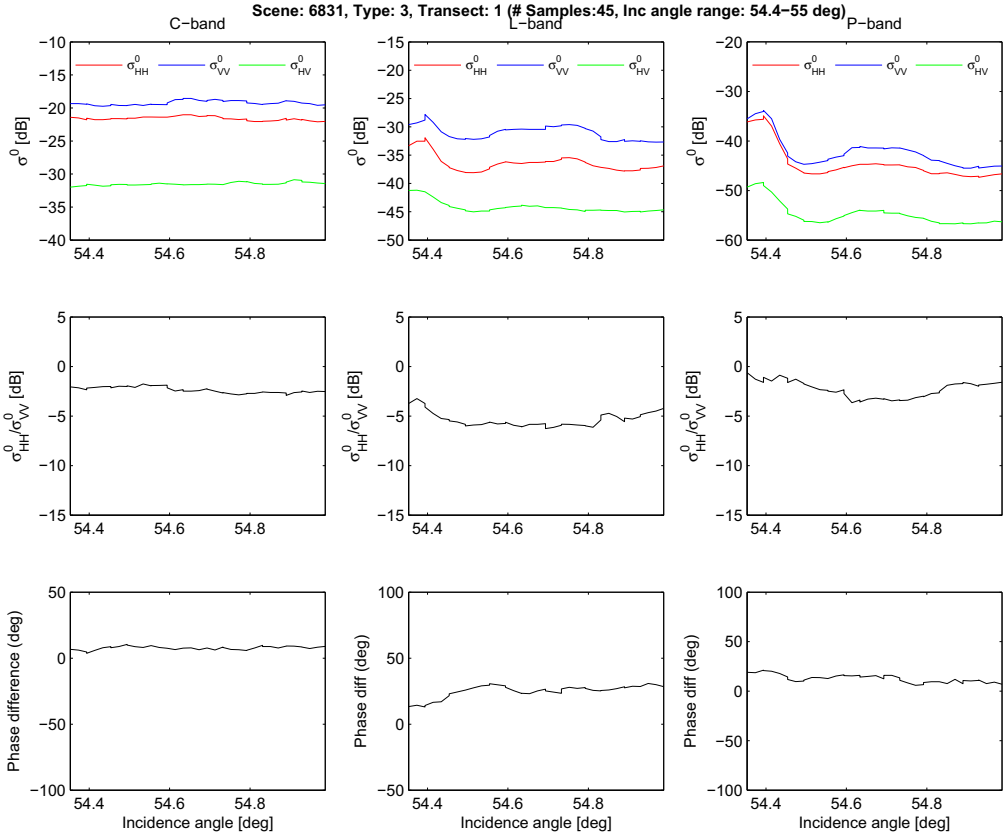
Scene: 6831, Type: 3, Transect: 1 (# Samples:45, Inc angle range: 54.4−55 deg)
C−band
L−band
P−band
σ⁰ [dB]
σ⁰HH/σ⁰VV [dB]
Phase difference (deg)
Phase diff (deg)
Incidence angle [deg]

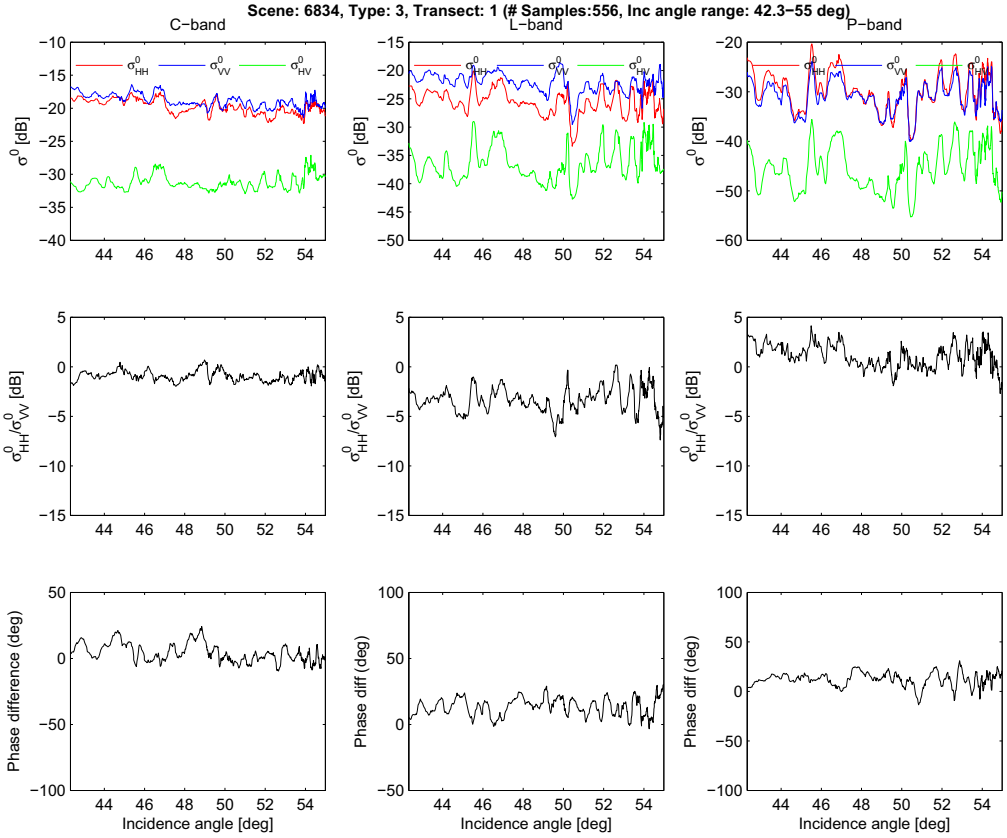
Scene: 6834, Type: 3, Transect: 1 (# Samples:556, Inc angle range: 42.3−55 deg)
C−band
L−band
P−band
σ⁰ [dB]
σ⁰HH/σ⁰VV [dB]
Phase difference (deg)
Phase diff (deg)
Incidence angle [deg]

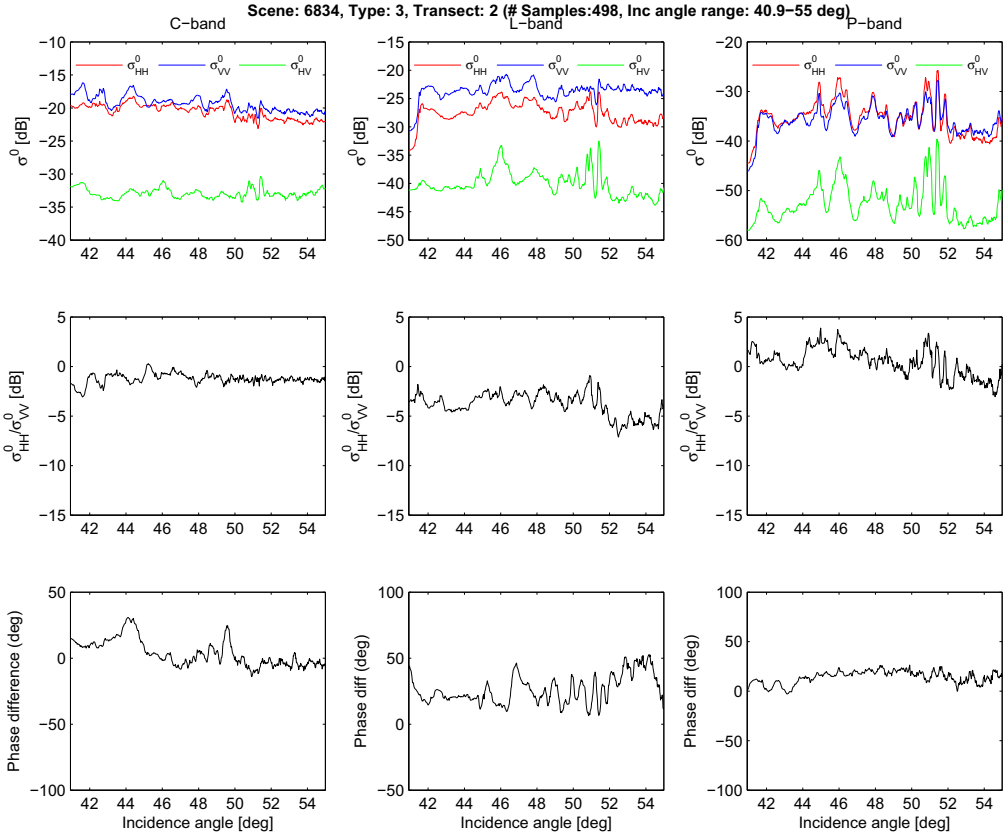
Scene: 6834, Type: 3, Transect: 2 (# Samples:498, Inc angle range: 40.9−55 deg)
C−band
L−band
P−band
σ0HH
σ0VV
σ0HV
σ0 [dB]
σ0HH/σ0VV [dB]
Phase difference (deg)
Phase diff (deg)
Incidence angle [deg]

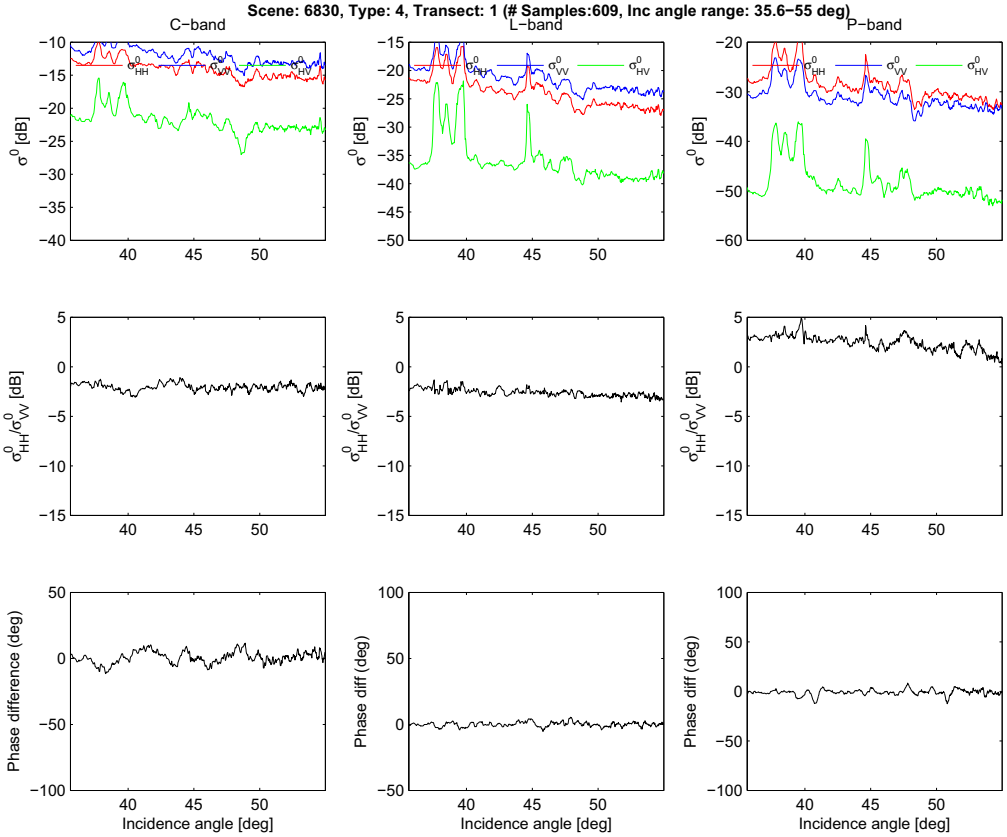
Scene: 6830, Type: 4, Transect: 1 (# Samples:609, Inc angle range: 35.6−55 deg)
C−band
L−band
P−band
σ0HH
σ0VV
σ0HV
σ0 [dB]
σ0HH/σ0VV [dB]
Phase difference (deg)
Phase diff (deg)
Incidence angle [deg]

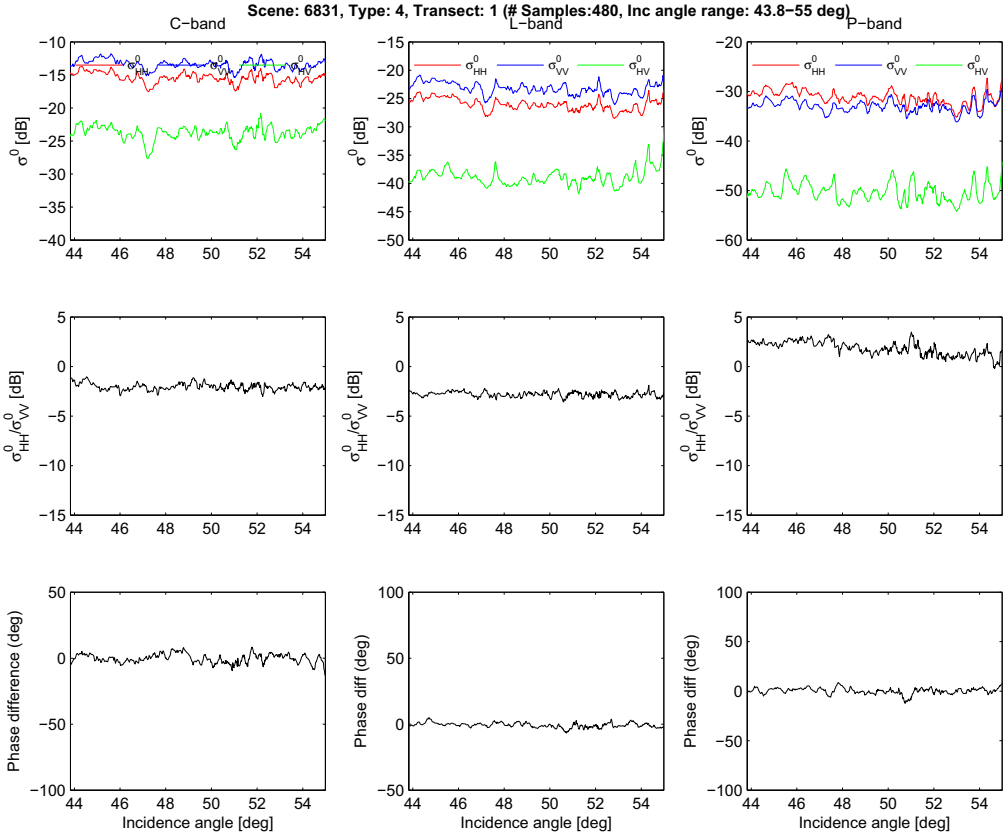
Scene: 6831, Type: 4, Transect: 1 (# Samples:480, Inc angle range: 43.8−55 deg)
C−band
L−band
P−band
σ0 [dB]
σ0HH
σ0VV
σ0HV
σ0HH/σ0VV [dB]
Phase difference (deg)
Phase diff (deg)
Incidence angle [deg]

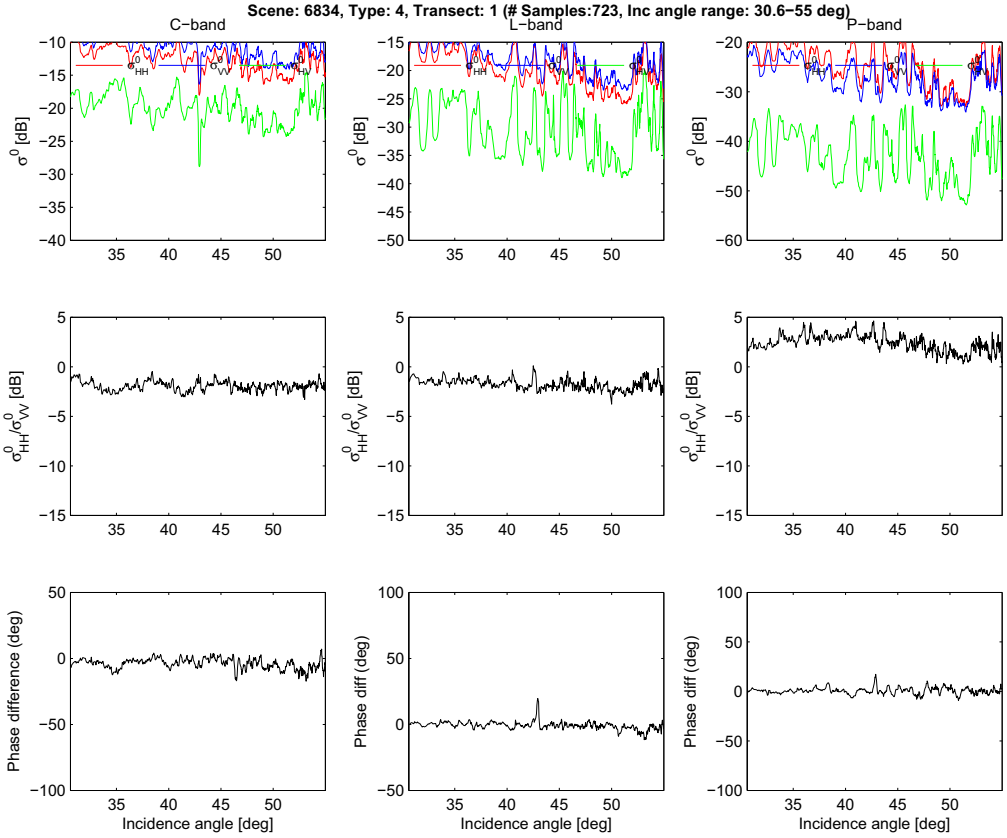
Scene: 6834, Type: 4, Transect: 1 (# Samples:723, Inc angle range: 30.6−55 deg)
C−band
L−band
P−band
σ0 [dB]
σ0HH
σ0VV
σ0HV
σ0HH/σ0VV [dB]
Phase difference (deg)
Phase diff (deg)
Incidence angle [deg]

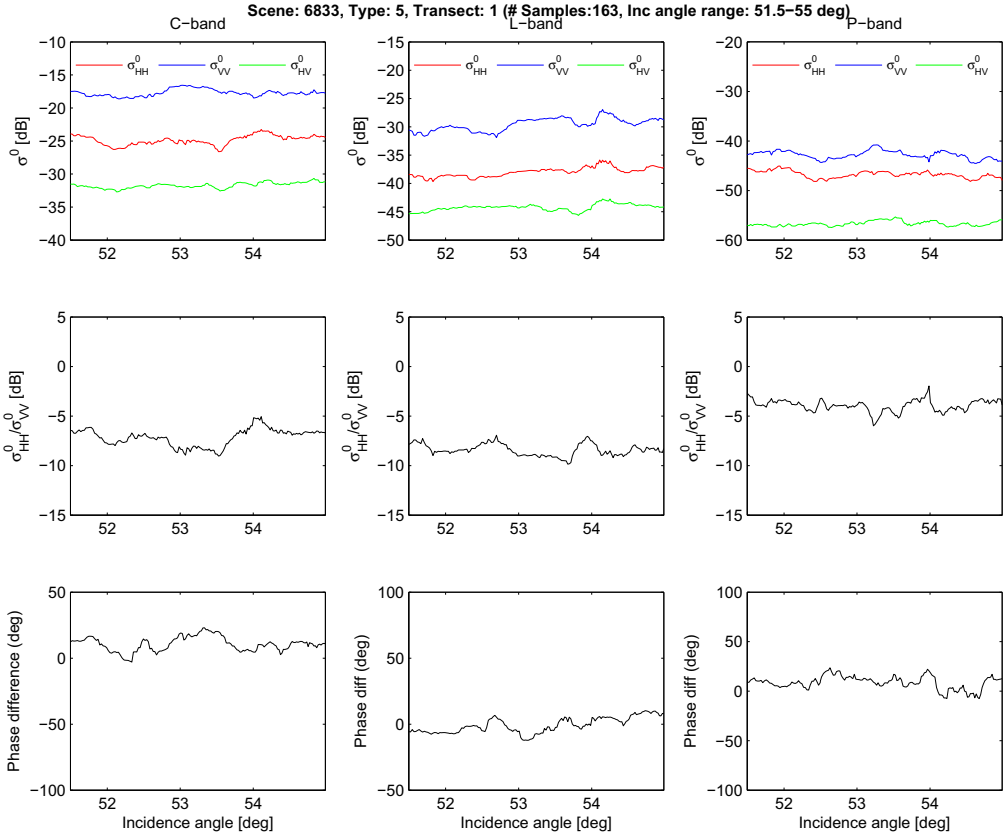
Scene: 6833, Type: 5, Transect: 1 (# Samples:163, Inc angle range: 51.5−55 deg)
C−band
L−band
P−band
σ0HH
σ0VV
σ0HV
σ0 [dB]
σ0HH/σ0VV [dB]
Phase difference (deg)
Phase diff (deg)
Incidence angle [deg]

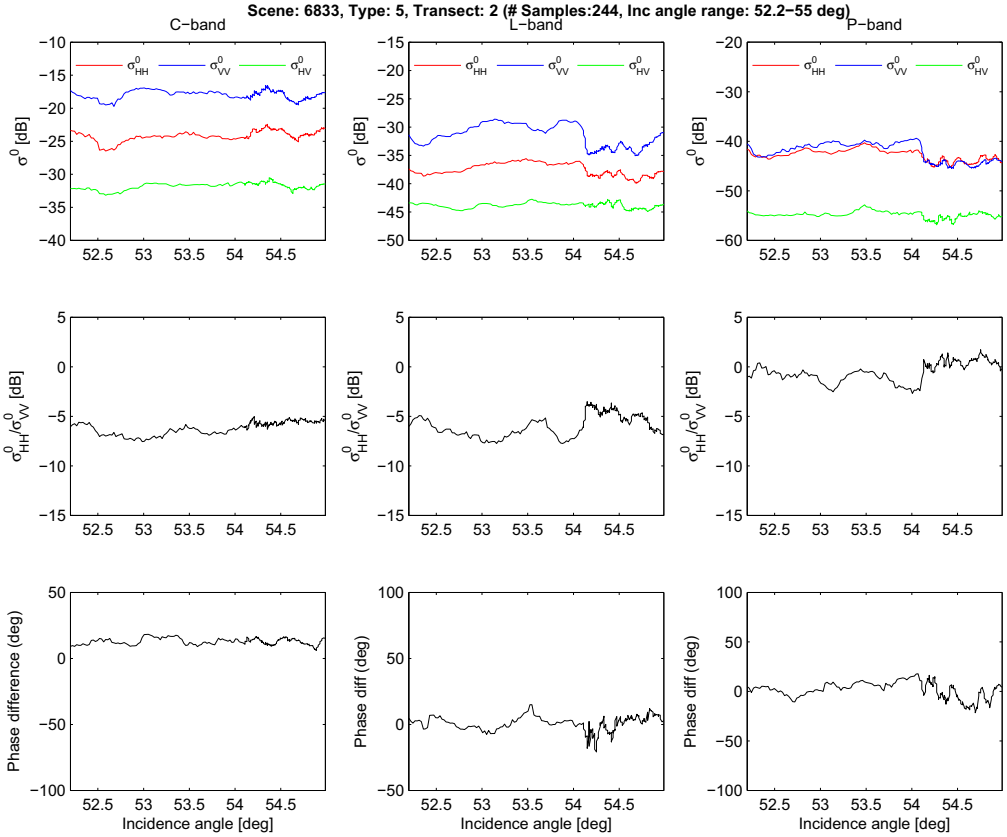
Scene: 6833, Type: 5, Transect: 2 (# Samples:244, Inc angle range: 52.2−55 deg)
C−band
L−band
P−band
σ0HH
σ0VV
σ0HV
σ0 [dB]
σ0HH/σ0VV [dB]
Phase difference (deg)
Phase diff (deg)
Incidence angle [deg]

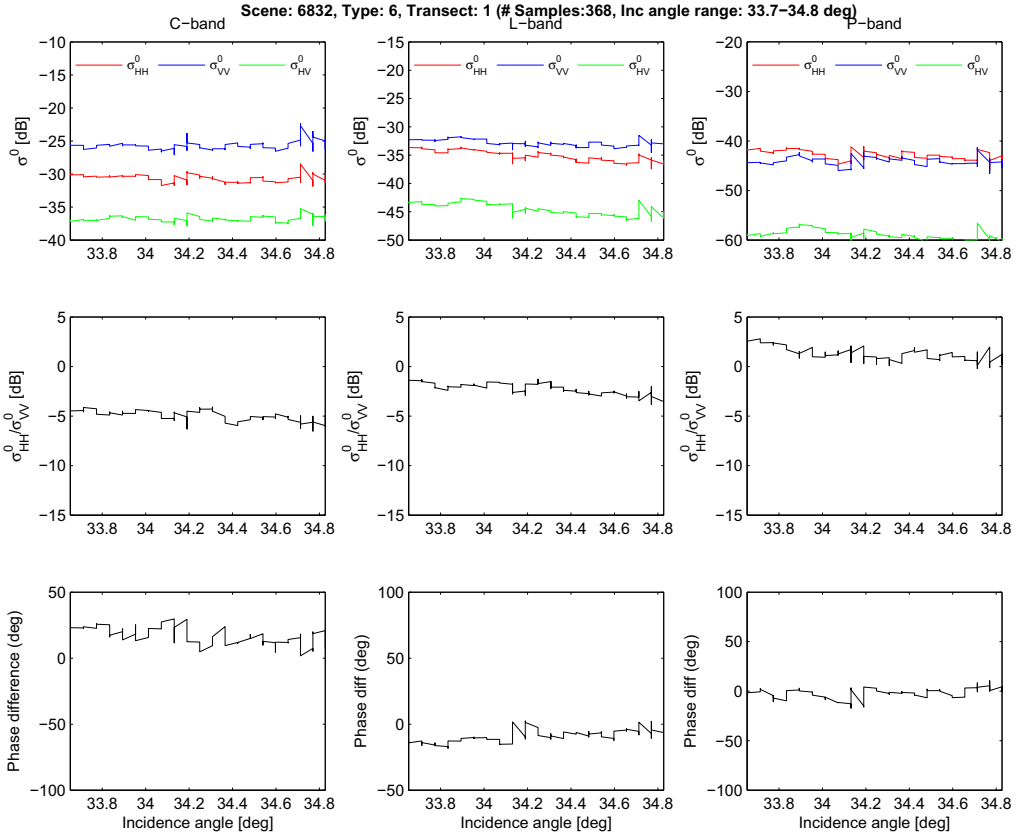
Scene: 6832, Type: 6, Transect: 1 (# Samples:368, Inc angle range: 33.7−34.8 deg)
C−band
L−band
P−band
σ⁰HH
σ⁰VV
σ⁰HV
σ⁰ [dB]
σ⁰HH/σ⁰VV [dB]
Phase difference (deg)
Phase diff (deg)
Incidence angle [deg]

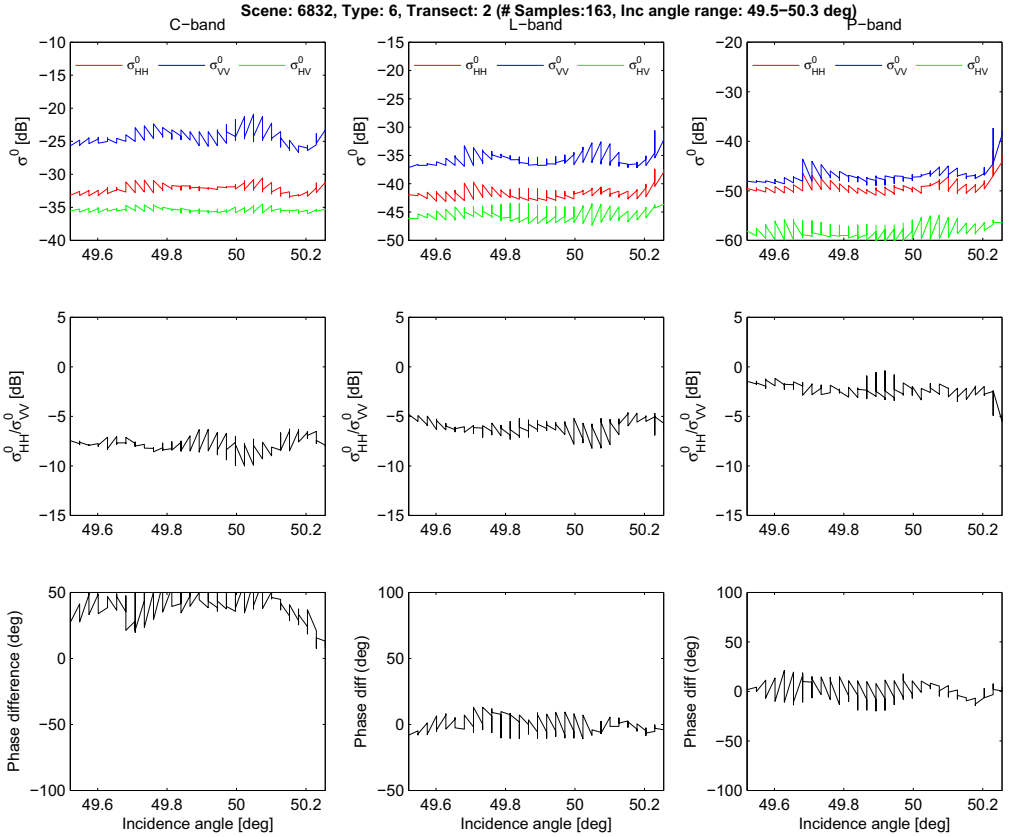
Scene: 6832, Type: 6, Transect: 2 (# Samples:163, Inc angle range: 49.5−50.3 deg)
C−band
L−band
P−band
σ⁰HH
σ⁰VV
σ⁰HV
σ⁰ [dB]
σ⁰HH/σ⁰VV [dB]
Phase difference (deg)
Phase diff (deg)
Incidence angle [deg]

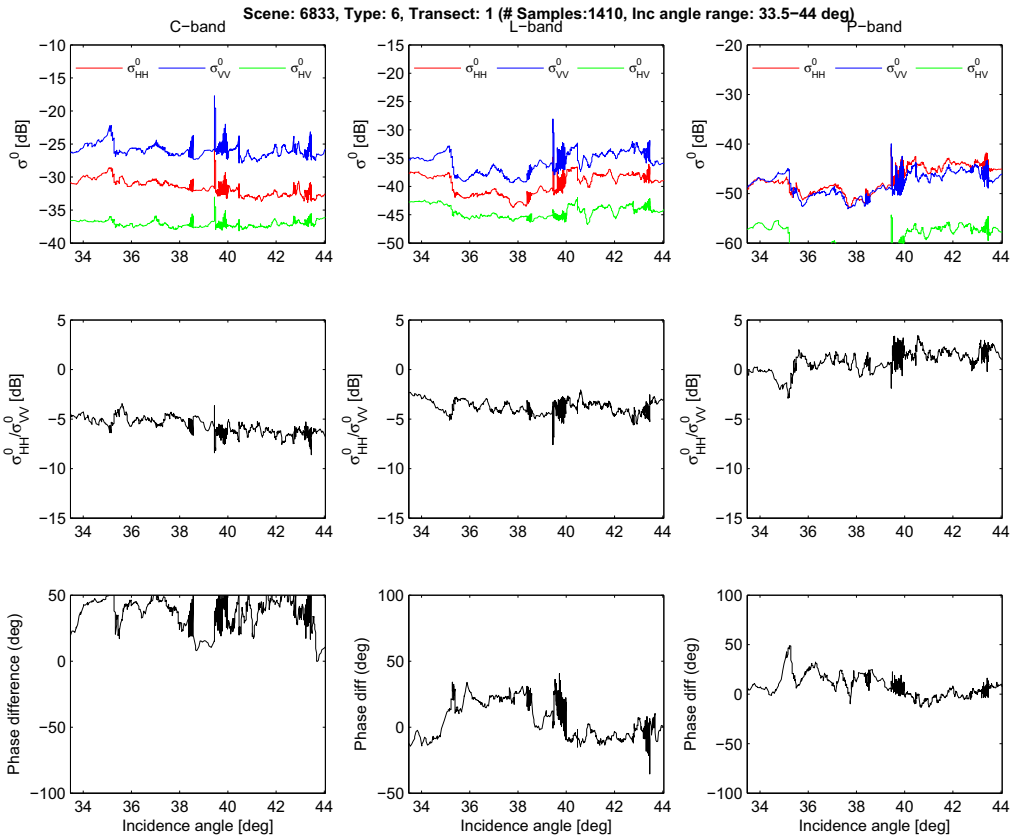
Scene: 6833, Type: 6, Transect: 1 (# Samples:1410, Inc angle range: 33.5−44 deg)
C−band
L−band
P−band
σ⁰HH
σ⁰VV
σ⁰HV
σ⁰ [dB]
σ⁰HH/σ⁰VV [dB]
Phase difference (deg)
Phase diff (deg)
Incidence angle [deg]

Appendix G Combination of parameters over all incidence angels

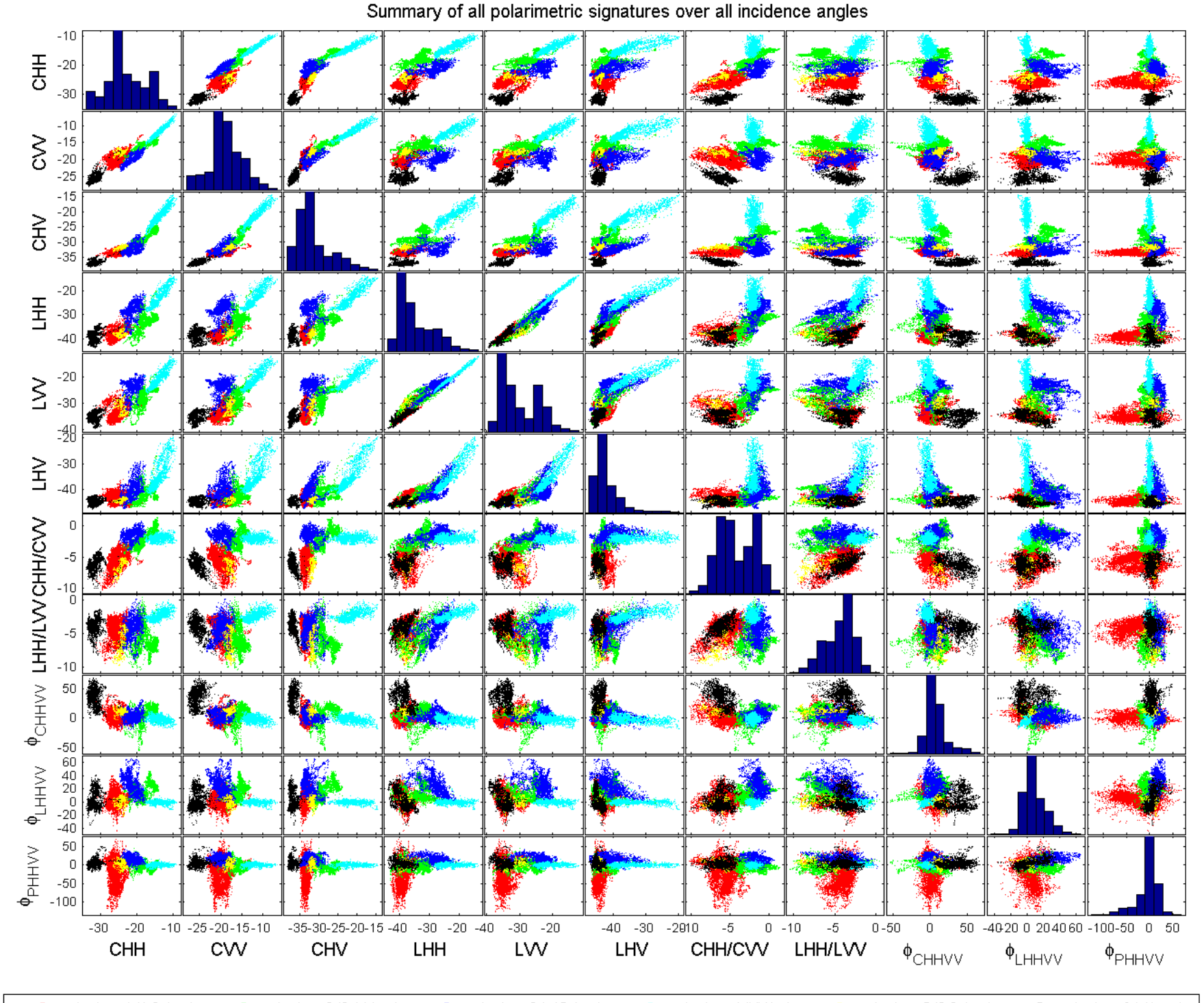
Summary of all polarimetric signatures over all incidence angles
CHH
CVV
CHV
LHH
LVV
LHV
CHH/CVV
LHH/LVV
ϕ_{CHHVV}
ϕ_{LHHVV}
ϕ_{PHHVV}
Ice type 1 (1-2 days)
Ice type 2 (9-14days)
Ice type 3 (>15 days)
Ice type 4 (MY ice)
Ice type 5 (2-3 days)
Ice type 6 (~Hours)

Appendix H **Combination of parameters in five different ranges of incidence angles**

Five different ranges of incidence angles: $\theta=30^{o}$-35^{o}, 35^{o}-40^{o}, 40^{o}-45^{o}, 45^{o}-50^{o} and 50^{o}-55^{o}

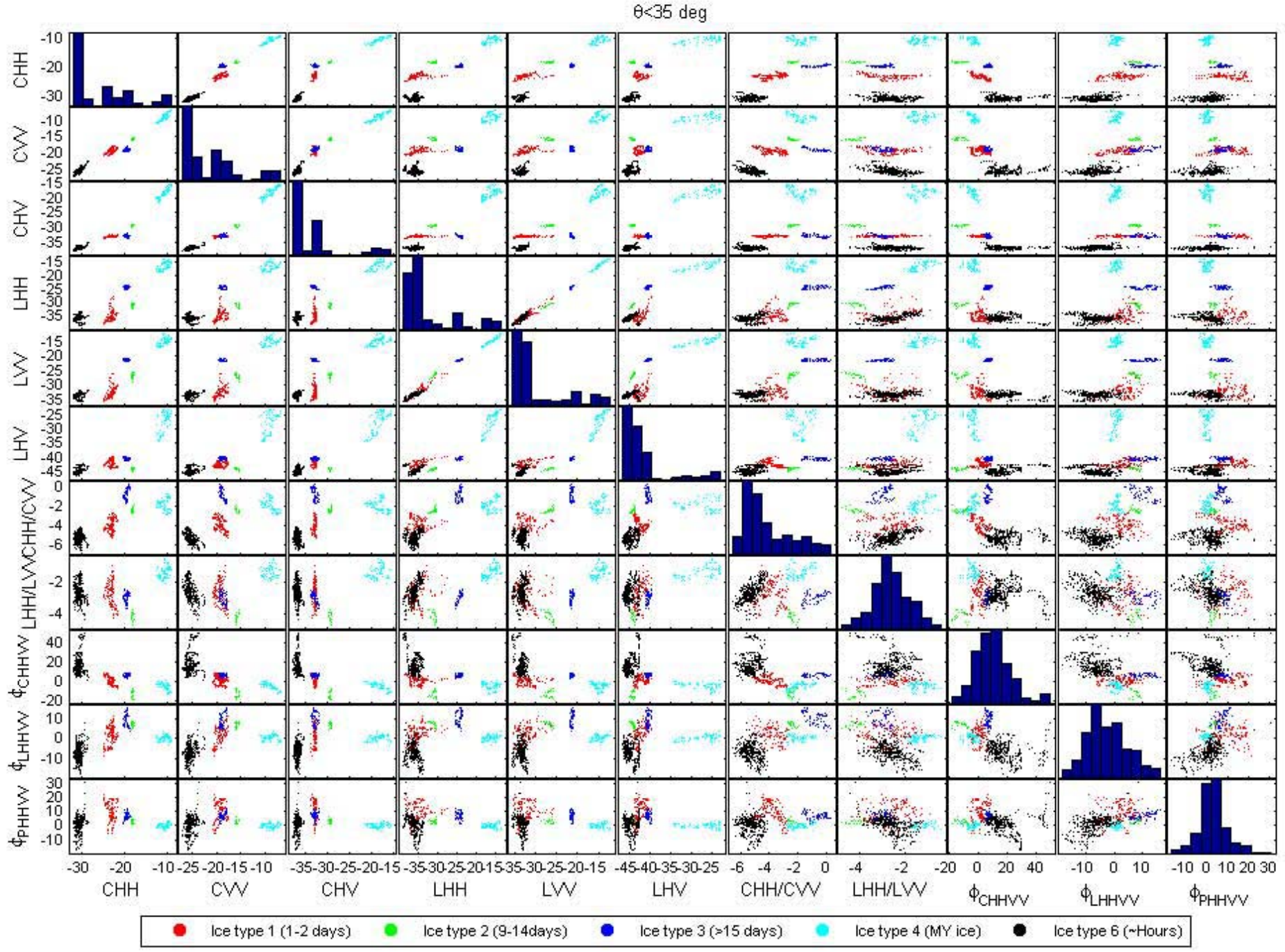
θ<35 deg
CHH
CVV
CHV
LHH
LVV
LHV
CHH/CVV
LHH/LVV
ϕCHHVV
ϕLHHVV
ϕPHHVV
Ice type 1 (1-2 days)
Ice type 2 (9-14days)
Ice type 3 (>15 days)
Ice type 4 (MY ice)
Ice type 6 (~Hours)

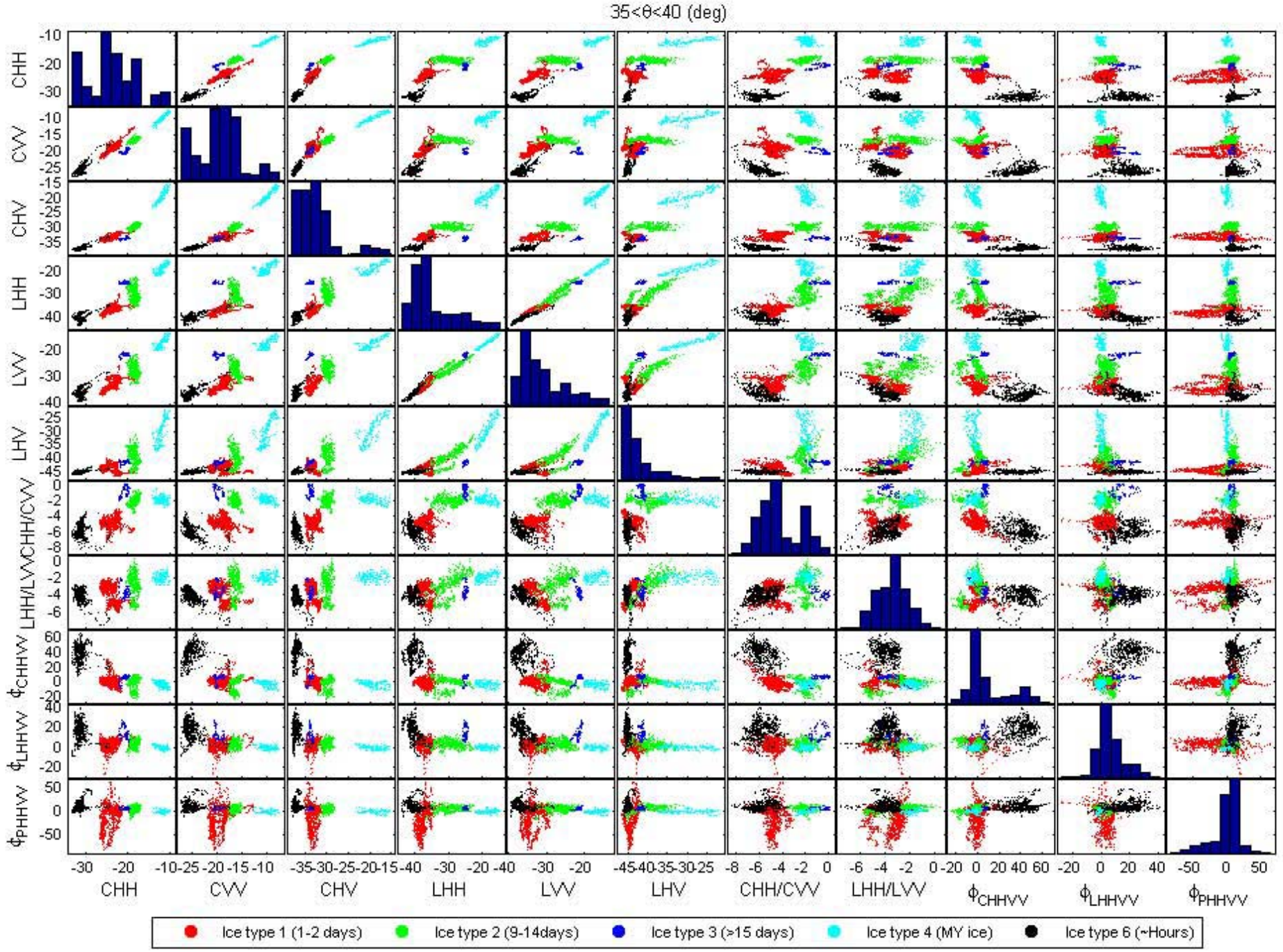
35<θ<40 (deg)
CHH
CVV
CHV
LHH
LVV
LHV
CHH/CVV
LHH/LVV
ϕ_{CHHVV}
ϕ_{LHHVV}
ϕ_{PHHVV}
Ice type 1 (1-2 days)
Ice type 2 (9-14days)
Ice type 3 (>15 days)
Ice type 4 (MY ice)
Ice type 6 (~Hours)

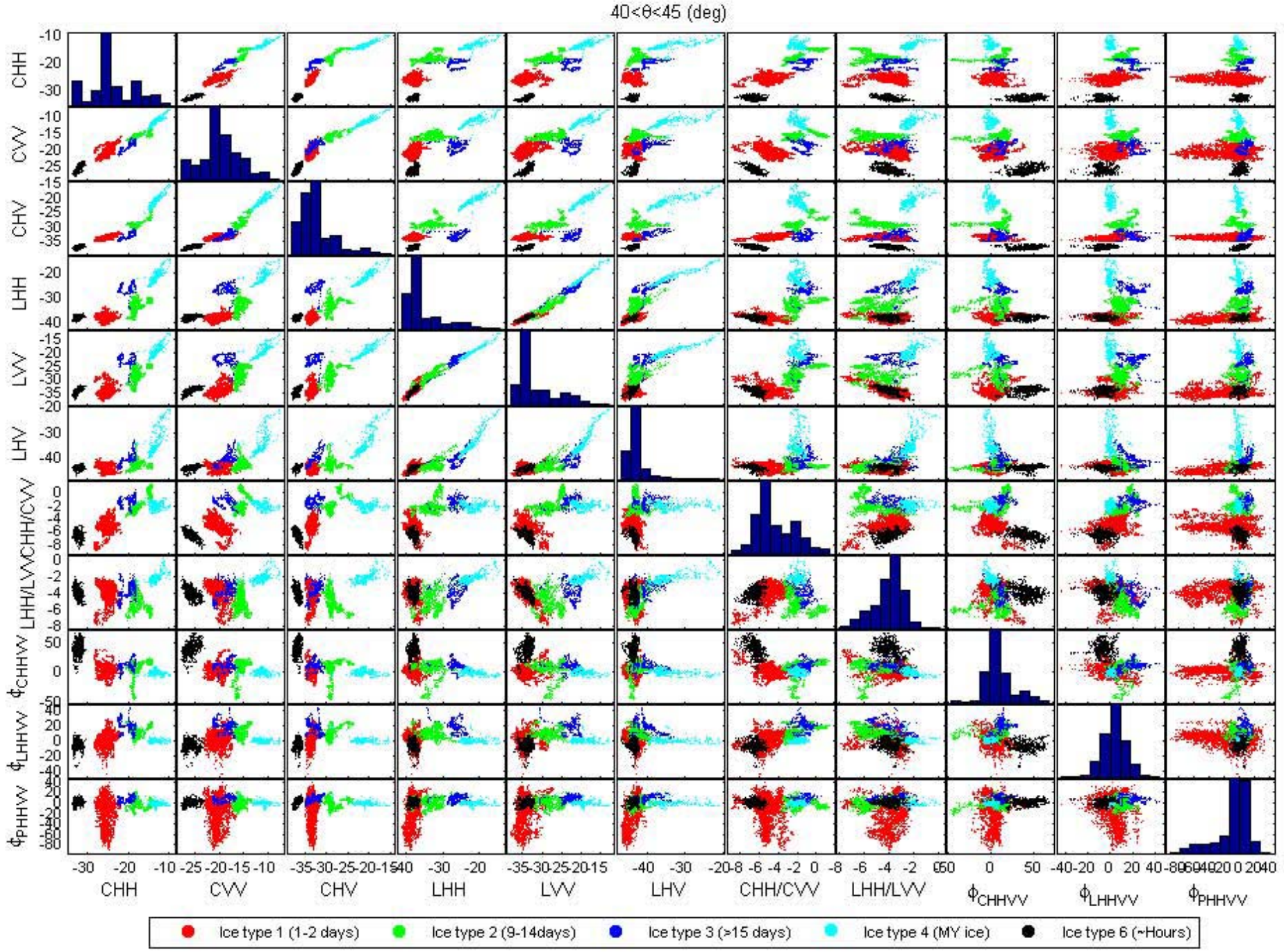
40<θ<45 (deg)
CHH
CVV
CHV
LHH
LVV
LHV
CHH/CVV
LHH/LVV
ϕCHHVV
ϕLHHVV
ϕPHHVV
Ice type 1 (1-2 days)
Ice type 2 (9-14days)
Ice type 3 (>15 days)
Ice type 4 (MY ice)
Ice type 6 (~Hours)

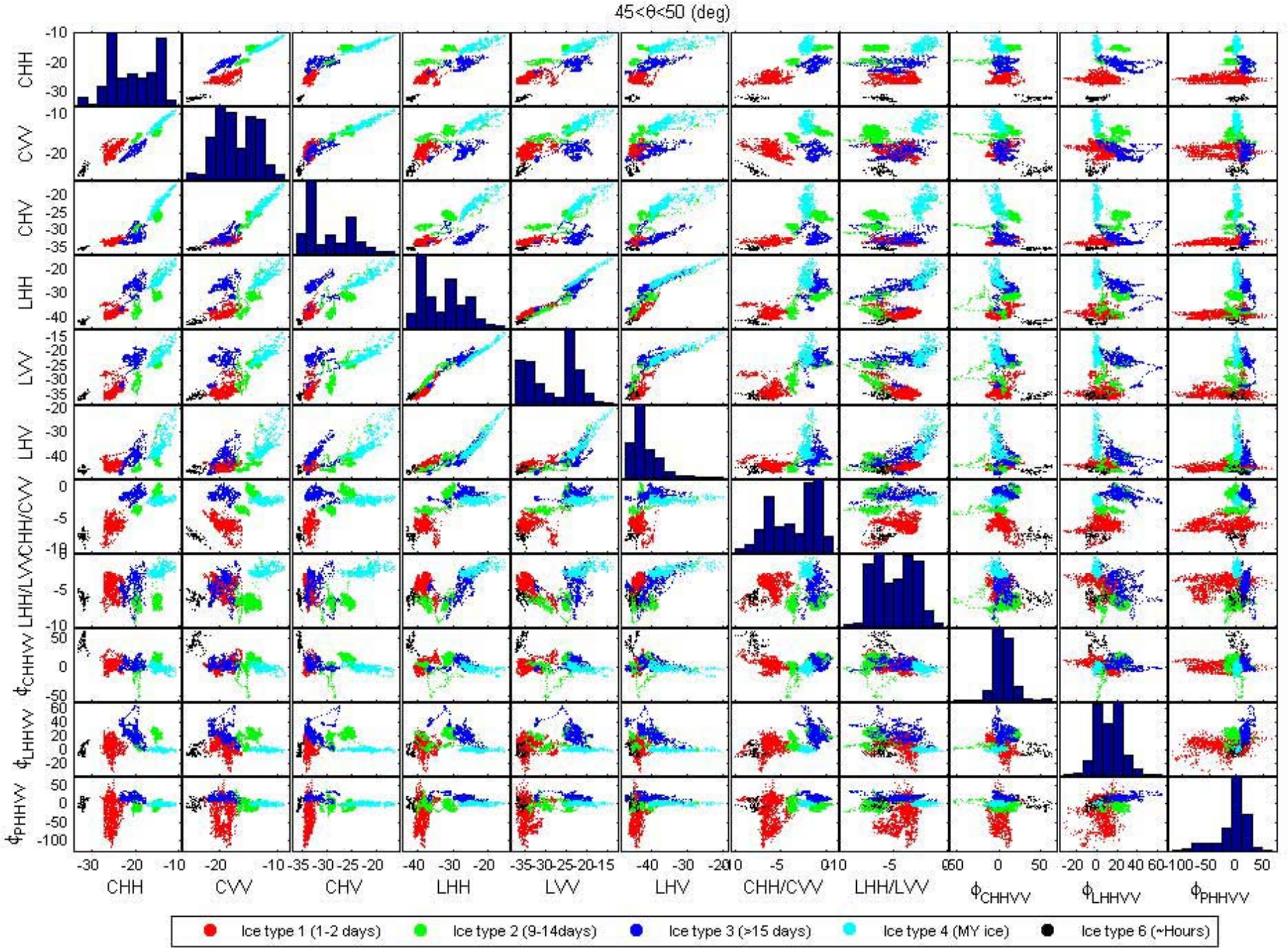
45<θ<50 (deg)
CHH
CVV
CHV
LHH
LVV
LHV
CHH/CVV
LHH/LVV
ϕ_{CHHVV}
ϕ_{LHHVV}
ϕ_{PHHVV}
Ice type 1 (1-2 days)
Ice type 2 (9-14days)
Ice type 3 (>15 days)
Ice type 4 (MY ice)
Ice type 6 (~Hours)

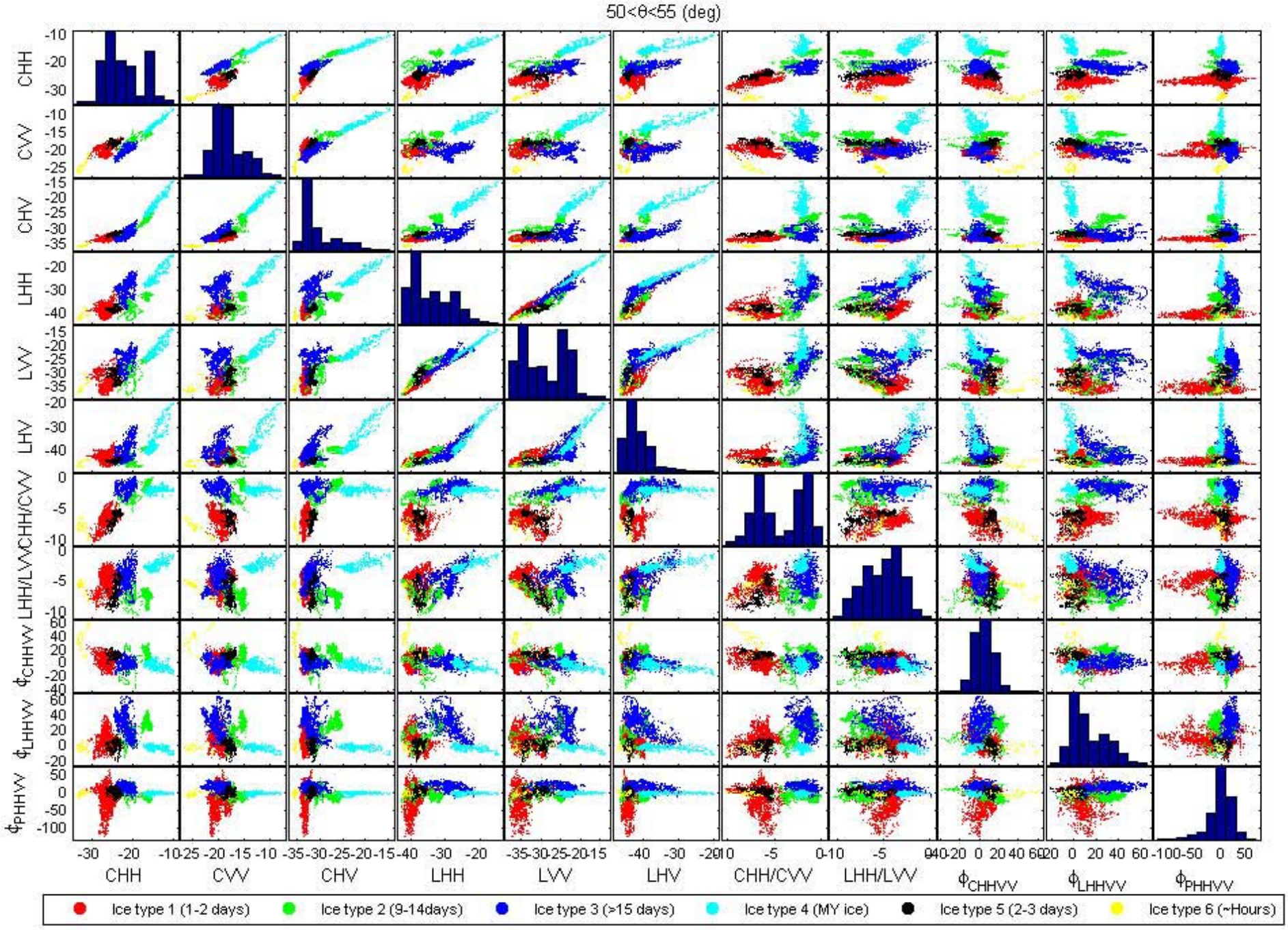
50<θ<55 (deg)
CHH
CVV
CHV
LHH
LVV
LHV
CHH/CVV
LHH/LVV
ϕ_{CHHVV}
ϕ_{LHHVV}
ϕ_{PHHVV}
Ice type 1 (1-2 days)
Ice type 2 (9-14days)
Ice type 3 (>15 days)
Ice type 4 (MY ice)
Ice type 5 (2-3 days)
Ice type 6 (~Hours)

Appendix I **Classification accuracies for different parameter combinations**

Misclassification error for six ice types (Quadratic classification)

		Ice1	Ice2	Ice3	Ice4	Ice5	Ice6	Overall
Param1	**Param2**	**1-2 day**	**12 days**	**>15 days**	**MY ice**	**2-3 days**	**<1 day**	**Error**
CHV	CHH/CVV	8,3%	10,8%	10,5%	2,6%	5,2%	1,3%	7,7%
CHH/CVV	CHV	8,3%	10,8%	10,5%	2,6%	5,2%	1,3%	7,7%
LHH	CHV	9,3%	11,8%	12,4%	2,3%	4,9%	1,7%	8,6%
CHV	LHH	9,3%	11,8%	12,4%	2,3%	4,9%	1,7%	8,6%
CHH	CHV	11,9%	13,6%	18,5%	2,8%	5,9%	1,0%	10,9%
CHV	CHH	11,9%	13,6%	18,5%	2,8%	5,9%	1,0%	10,9%
CHV	\phi_{LHHVV}	13,4%	10,3%	24,9%	0,3%	7,6%	1,7%	11,5%
\phi_{LHHVV}	CHV	13,4%	10,3%	24,9%	0,3%	7,6%	1,7%	11,5%
LVV	CHV	11,8%	27,9%	17,2%	3,8%	6,9%	2,0%	13,8%
CHV	LVV	11,8%	27,9%	17,2%	3,8%	6,9%	2,0%	13,8%
LHH/LVV	CHH	15,5%	18,4%	22,2%	0,3%	12,0%	1,7%	13,8%
CHH	LHH/LVV	15,5%	18,4%	22,2%	0,3%	12,0%	1,7%	13,8%
CHH	CVV	24,5%	10,9%	6,4%	3,9%	7,1%	1,6%	14,4%
CHH	CHH/CVV	24,5%	10,9%	6,4%	3,9%	7,1%	1,6%	14,4%
CVV	CHH	24,5%	10,9%	6,4%	3,9%	7,1%	1,6%	14,4%
CVV	CHH/CVV	24,5%	10,9%	6,4%	3,9%	7,1%	1,6%	14,4%
CHH/CVV	CHH	24,5%	10,9%	6,4%	3,9%	7,1%	1,6%	14,4%
CHH/CVV	CVV	24,5%	10,9%	6,4%	3,9%	7,1%	1,6%	14,4%
LHH	CVV	24,5%	13,6%	10,0%	1,2%	8,6%	2,9%	15,3%
CVV	LHH	24,5%	13,6%	10,0%	1,2%	8,6%	2,9%	15,3%
LHV	CHV	12,8%	20,2%	48,2%	4,3%	5,2%	2,6%	16,7%
CHV	LHV	12,8%	20,2%	48,2%	4,3%	5,2%	2,6%	16,7%
LVV	CHH	24,6%	25,2%	8,9%	4,4%	10,1%	0,8%	17,8%
CHH	LVV	24,6%	25,2%	8,9%	4,4%	10,1%	0,8%	17,8%
LHH/LVV	CHV	15,1%	14,7%	62,4%	0,6%	14,7%	2,8%	18,3%
CHV	LHH/LVV	15,1%	14,7%	62,4%	0,6%	14,7%	2,8%	18,3%
LVV	CVV	24,3%	28,5%	9,1%	5,4%	14,5%	2,1%	18,6%
CVV	LVV	24,3%	28,5%	9,1%	5,4%	14,5%	2,1%	18,6%
LHH	CHH	35,1%	8,5%	9,8%	0,6%	18,9%	1,1%	18,8%
CHH	LHH	35,1%	8,5%	9,8%	0,6%	18,9%	1,1%	18,8%
CHV	\phi_{CHHVV}	11,9%	15,8%	76,5%	3,1%	8,1%	1,7%	18,9%
\phi_{CHHVV}	CHV	11,9%	15,8%	76,5%	3,1%	8,1%	1,7%	18,9%
CHH	\phi_{LHHVV}	32,3%	15,4%	16,1%	0,4%	13,8%	1,8%	19,8%
\phi_{LHHVV}	CHH	32,3%	15,4%	16,1%	0,4%	13,8%	1,8%	19,8%
CVV	CHV	16,5%	18,5%	63,6%	4,2%	6,9%	2,0%	19,9%
CHV	CVV	16,5%	18,5%	63,6%	4,2%	6,9%	2,0%	19,9%
LHV	CHH	27,4%	20,3%	22,8%	9,4%	10,8%	1,7%	20,3%
CHH	LHV	27,4%	20,3%	22,8%	9,4%	10,8%	1,7%	20,3%
CHH	\phi_{CHHVV}	26,1%	24,5%	25,9%	4,5%	12,5%	1,2%	20,5%
\phi_{CHHVV}	CHH	26,1%	24,5%	25,9%	4,5%	12,5%	1,2%	20,5%
LHV	CVV	26,3%	16,4%	40,5%	7,3%	3,9%	2,7%	21,1%
CVV	LHV	26,3%	16,4%	40,5%	7,3%	3,9%	2,7%	21,1%
CVV	\phi_{LHHVV}	33,7%	14,5%	23,9%	0,4%	8,4%	3,2%	21,3%
\phi_{LHHVV}	CVV	33,7%	14,5%	23,9%	0,4%	8,4%	3,2%	21,3%

		Ice1	Ice2	Ice3	Ice4	Ice5	Ice6	Overall
Param1	**Param2**	**1-2 day**	**12 days**	**>15 days**	**MY ice**	**2-3 days**	**<1 day**	**Error**
CHV	CHV	11,5%	17,9%	93,8%	4,3%	8,8%	2,5%	21,6%
CHV	\phi_{PHHVV}	33,0%	24,1%	27,2%	4,2%	14,3%	2,4%	23,8%
\phi_{PHHVV}	CHV	33,0%	24,1%	27,2%	4,2%	14,3%	2,4%	23,8%
CHH	\phi_{PHHVV}	32,6%	37,3%	16,5%	6,7%	12,3%	2,1%	25,1%
\phi_{PHHVV}	CHH	32,6%	37,3%	16,5%	6,7%	12,3%	2,1%	25,1%
LHH/LVV	CVV	35,7%	18,4%	50,6%	0,4%	14,7%	3,1%	26,5%
CVV	LHH/LVV	35,7%	18,4%	50,6%	0,4%	14,7%	3,1%	26,5%
CVV	\phi_{PHHVV}	44,1%	26,5%	19,2%	5,0%	16,7%	3,3%	28,3%
\phi_{PHHVV}	CVV	44,1%	26,5%	19,2%	5,0%	16,7%	3,3%	28,3%
LVV	\phi_{CHHVV}	20,8%	48,8%	47,9%	20,3%	11,5%	17,4%	29,4%
\phi_{CHHVV}	LVV	20,8%	48,8%	47,9%	20,3%	11,5%	17,4%	29,4%
CHH	CHH	36,7%	49,3%	25,9%	12,4%	19,4%	1,7%	31,2%
LHH	\phi_{CHHVV}	36,0%	33,3%	40,9%	15,8%	11,1%	19,0%	31,6%
\phi_{CHHVV}	LHH	36,0%	33,3%	40,9%	15,8%	11,1%	19,0%	31,6%
CHH/CVV	\phi_{CHHVV}	31,9%	50,9%	42,5%	14,8%	10,8%	16,7%	33,3%
\phi_{CHHVV}	CHH/CVV	31,9%	50,9%	42,5%	14,8%	10,8%	16,7%	33,3%
CVV	\phi_{CHHVV}	53,6%	11,6%	60,5%	3,5%	8,1%	1,5%	34,1%
\phi_{CHHVV}	CVV	53,6%	11,6%	60,5%	3,5%	8,1%	1,5%	34,1%
LVV	\phi_{PHHVV}	50,0%	50,4%	20,8%	7,0%	39,6%	21,1%	38,6%
\phi_{PHHVV}	LVV	50,0%	50,4%	20,8%	7,0%	39,6%	21,1%	38,6%
LHH	\phi_{PHHVV}	52,8%	30,9%	20,2%	4,5%	20,9%	54,8%	38,7%
\phi_{PHHVV}	LHH	52,8%	30,9%	20,2%	4,5%	20,9%	54,8%	38,7%
CHH/CVV	\phi_{PHHVV}	49,9%	40,5%	13,3%	9,3%	33,9%	61,0%	40,0%
\phi_{PHHVV}	CHH/CVV	49,9%	40,5%	13,3%	9,3%	33,9%	61,0%	40,0%
LHV	\phi_{CHHVV}	31,0%	67,3%	70,0%	32,1%	11,5%	13,4%	41,2%
\phi_{CHHVV}	LHV	31,0%	67,3%	70,0%	32,1%	11,5%	13,4%	41,2%
LHH/LVV	\phi_{LHHVV}	50,9%	38,2%	27,8%	3,2%	34,2%	60,6%	41,2%
\phi_{LHHVV}	LHH/LVV	50,9%	38,2%	27,8%	3,2%	34,2%	60,6%	41,2%
LHH/LVV	CHH/CVV	68,0%	23,2%	39,9%	4,6%	27,0%	15,5%	42,2%
CHH/CVV	LHH/LVV	68,0%	23,2%	39,9%	4,6%	27,0%	15,5%	42,2%
CHH/CVV	\phi_{LHHVV}	47,5%	55,6%	19,2%	2,6%	29,2%	64,3%	42,4%
\phi_{LHHVV}	CHH/CVV	47,5%	55,6%	19,2%	2,6%	29,2%	64,3%	42,4%
LHH	CHH/CVV	60,2%	26,5%	30,8%	7,6%	17,7%	61,1%	43,3%
CHH/CVV	LHH	60,2%	26,5%	30,8%	7,6%	17,7%	61,1%	43,3%
LHH	\phi_{LHHVV}	66,6%	36,6%	11,9%	1,3%	23,3%	53,7%	44,4%
\phi_{LHHVV}	LHH	66,6%	36,6%	11,9%	1,3%	23,3%	53,7%	44,4%
CVV	CVV	71,9%	26,2%	51,0%	8,6%	14,5%	3,3%	44,7%
\phi_{LHHVV}	\phi_{PHHVV}	54,6%	42,9%	24,4%	9,3%	45,7%	66,2%	44,8%
\phi_{PHHVV}	\phi_{LHHVV}	54,6%	42,9%	24,4%	9,3%	45,7%	66,2%	44,8%
LHH/LVV	\phi_{PHHVV}	53,7%	52,2%	38,0%	5,4%	45,0%	48,2%	45,7%
\phi_{PHHVV}	LHH/LVV	53,7%	52,2%	38,0%	5,4%	45,0%	48,2%	45,7%
\phi_{CHHVV}	LHH/LVV	41,7%	64,0%	94,9%	5,4%	16,7%	13,4%	45,8%
LHH/LVV	\phi_{CHHVV}	41,7%	64,0%	94,9%	5,4%	16,7%	13,4%	45,8%
\phi_{LHHVV}	LVV	64,7%	58,0%	14,9%	1,4%	39,6%	26,2%	45,8%
LVV	\phi_{LHHVV}	64,7%	58,0%	14,9%	1,4%	39,6%	26,2%	45,8%

		Ice1	Ice2	Ice3	Ice4	Ice5	Ice6	Overall
Param1	**Param2**	**1-2 day**	**12 days**	**>15 days**	**MY ice**	**2-3 days**	**<1 day**	**Error**
\phi_{CHHVV}	\phi_{LHHVV}	60,9%	53,7%	39,5%	7,7%	14,3%	22,8%	46,1%
\phi_{LHHVV}	\phi_{CHHVV}	60,9%	53,7%	39,5%	7,7%	14,3%	22,8%	46,1%
CHH/CVV	LVV	63,1%	41,8%	37,3%	12,6%	28,3%	31,7%	46,1%
LVV	CHH/CVV	63,1%	41,8%	37,3%	12,6%	28,3%	31,7%	46,1%
CHH/CVV	LHV	51,4%	58,1%	33,9%	16,6%	20,9%	53,6%	46,5%
LHV	CHH/CVV	51,4%	58,1%	33,9%	16,6%	20,9%	53,6%	46,5%
\phi_{PHHVV}	LHV	56,6%	59,9%	33,6%	10,2%	20,1%	49,5%	48,0%
LHV	\phi_{PHHVV}	56,6%	59,9%	33,6%	10,2%	20,1%	49,5%	48,0%
\phi_{CHHVV}	\phi_{PHHVV}	56,5%	74,2%	35,7%	10,6%	21,6%	20,8%	48,2%
\phi_{PHHVV}	\phi_{CHHVV}	56,5%	74,2%	35,7%	10,6%	21,6%	20,8%	48,2%
LVV	LHV	59,1%	61,3%	44,0%	18,5%	34,2%	34,0%	50,2%
LHV	LVV	59,1%	61,3%	44,0%	18,5%	34,2%	34,0%	50,2%
LHH	LHV	66,8%	44,0%	36,6%	23,6%	16,5%	51,0%	51,0%
LHV	LHH	66,8%	44,0%	36,6%	23,6%	16,5%	51,0%	51,0%
\phi_{LHHVV}	LHV	68,0%	68,6%	29,3%	1,3%	19,7%	44,7%	52,8%
LHV	\phi_{LHHVV}	68,0%	68,6%	29,3%	1,3%	19,7%	44,7%	52,8%
LHV	LHH/LVV	64,2%	51,9%	73,3%	5,1%	32,4%	34,6%	52,9%
LHH/LVV	LHV	64,2%	51,9%	73,3%	5,1%	32,4%	34,6%	52,9%
LHH	LVV	82,8%	36,6%	48,3%	2,8%	33,9%	29,2%	53,8%
LHH	LHH/LVV	82,8%	36,6%	48,3%	2,8%	33,9%	29,2%	53,8%
LVV	LHH	82,8%	36,6%	48,3%	2,8%	33,9%	29,2%	53,8%
LVV	LHH/LVV	82,8%	36,6%	48,3%	2,8%	33,9%	29,2%	53,8%
LHH/LVV	LHH	82,8%	36,6%	48,3%	2,8%	33,9%	29,2%	53,8%
LHH/LVV	LVV	82,8%	36,6%	48,3%	2,8%	33,9%	29,2%	53,8%
\phi_{PHHVV}	\phi_{PHHVV}	60,2%	71,1%	25,8%	11,3%	100,0%	75,3%	55,6%
CHH/CVV	CHH/CVV	57,4%	76,2%	39,8%	17,3%	44,2%	76,9%	56,7%
\phi_{LHHVV}	\phi_{LHHVV}	63,4%	62,3%	47,2%	8,7%	71,5%	84,4%	58,0%
LHH	LHH	84,3%	36,1%	43,7%	34,4%	21,6%	67,7%	60,9%
LVV	LVV	85,5%	73,9%	58,4%	41,7%	54,5%	37,8%	69,3%
LHV	LHV	74,5%	82,2%	79,6%	47,7%	19,2%	51,7%	70,3%
LHH/LVV	LHH/LVV	85,7%	83,2%	99,3%	7,9%	39,8%	47,9%	73,9%
\phi_{CHHVV}	\phi_{CHHVV}	100,0%	87,1%	83,3%	18,4%	15,7%	19,7%	76,3%